UCLouvain

École polytechnique de Louvain

Numerical Modelling of Mudflows: Investigation of Rheological Models

Author: **Noam Lemy Storme**
Supervisors: **Sandra Soares-Frazão, Hadrien Rattez**
Readers: **Nathan Delpierre, Miltiadis Papalexandris**
Academic year 2025–2026
Master [120] in Mechanical Engineering

Abstract

Mudflows are deadly gravity-driven hazards on Earth: unpredictable dense torrents of water, soil, and rock that travel at tens of metres per second and bury everything in their path. Predicting where they go, how fast, and where they stop is a central and hard challenge for risk mitigation. Their complex behaviour, which combines the physics of water flows and granular media, makes them difficult to model and simulate. This master's thesis tackles a simple question: can Watlab, a finite-volume shallow-water solver built at UCLouvain for river and flood flows, be turned into a reliable predictive tool for viscoplastic mudflows, and which rheology best captures the behaviour of real muds?

The starting point is a single-phase, two-dimensional, depth-averaged description of the flow. A quick order-of-magnitude analysis exposes the core difficulty: in water, inertia dominates friction, but in mud the two are comparable. Therefore, the solver's original operator-splitting strategy breaks down in the friction-driven run-out phase. Three targeted fixes restore it: a temporary state variable, a vector-valued stopping criterion, and a semi-implicit treatment of friction. On top of this, four viscoplastic laws, Bingham, Herschel-Bulkley, Casson and quadratic, are implemented. The basal shear stress is recovered both by inverting the velocity law and through a faster, explicit slope-based formulation. The model is first stress-tested on a Carbopol dam-break benchmark, then turned loose on a real natural-mud experiment from an experimental campaign performed at Politecnico di Milano.

The final verdict shows that the approach based on Watlab is well suited for such applications. The slope-based closure matches the experimental data accurately, mainly for the steady flow phase, and is substantially less expensive than the velocity-based closure. On real mud, the model captures the overall shape and downstream extent of the deposit, but misses some behaviours of the experiment and the calibration remains delicate.

The outcome is a version of Watlab able to simulate viscoplastic free-surface flows, but not yet a ready-to-use predictive tool for natural mudflows. The perspectives for future work are numerous and promising for the development of a reliable tool for risk mitigation.

Acknowledgments

I would first like to thank my supervisors, Professor *Sandra Soares-Frazão* and Professor *Hadrien Rattez*, as well as the entire team, who welcomed me with remarkable warmth from day one, provided me with invaluable guidance and support throughout the thesis, and made a real difference in both the quality of my work and my experience of it.

My deepest thanks go to Nathan Delpierre, who accompanied me throughout the thesis. He guided me, helped me and supported me in all aspects of the work, at every step of the way. Without his help, this thesis would not have been the same.

I would also like to thank Simon Liesse, whose work I had the opportunity to continue, for his help and availability whenever I had questions.

A special thanks goes to Théo, Pablo, François, and Josephine for their patience with my long technical monologues and for their company during the many late working evenings.

I owe a profound debt of gratitude to my parents, Maud and Frank and my brother Tim. It is largely thanks to them that I have made it this far. They have supported me throughout my entire education and consistently made sure I had access to the best opportunities available. They have listened patiently as I shared the progress and setbacks of this work, offered their sharp and always welcome perspective. None of this would have been possible without them.

Finally, I would like to acknowledge the university and the public system that allowed me to pursue these studies under the best possible conditions. Access to higher education should never be a privilege reserved for the few. It is my sincere hope that we collectively continue to defend academic freedom, broaden access to all, and confront the structural inequalities that continue to limit this access.

Table of Contents

1 Introduction **1**

2 State of the art **5**

2.1 Definition of a mudflow 5

2.1.1 Physical description 5

2.1.2 The viscoplastic behaviour: yield stress and plug zones 7

2.1.3 Life cycle: initiation, runout, deposition 10

2.2 Classification of sediment-laden gravity flows 12

2.2.1 Mudflows in the spectrum of sediment-laden flows 12

2.2.2 Characterising the dominant regime: the Bagnold number 14

2.3 Modelling strategies 15

2.3.1 Phase representation 16

2.3.2 Spatial dimensionality 17

2.3.3 Numerical discretisation schemes 17

2.3.4 Summary of the main modelling choices 18

3 Shallow Water Solver and adaptation for mudflows **21**

3.1 Shallow Water Equations 21

3.1.1 Derivation framework 21

3.1.2 Governing equations 21

3.1.3 Closure relation 22

3.2 Numerical solver 23

3.2.1 Finite volume discretisation 23

3.2.2 Current implementation 23

3.3 Limitations for mudflow applications 24

3.4 Proposed adaptations of the solver 25

3.4.1 Temporary state variable and stopping criterion 25

3.4.2 Semi-implicit friction treatment 26

4 Rheological models and their depth-averaged implementation **29**

4.1 Rheological models 29

4.1.1 Bingham model 30

4.1.2 Herschel-Bulkley model 31

4.1.3 Casson model 32

4.1.4 Quadratic model 32

4.1.5 Comparison of the different rheological models . . . 33
4.2 Watlab implementation . . . 36
4.2.1 Computation of the shear stress at the bottom of the flow . . . 36
4.2.2 Regularisation of the constitutive laws . . . 39

5 Validation and sensitivity analysis 45
5.1 Experimental setup . . . 45
5.2 Numerical setup . . . 47
5.3 Results and discussion . . . 47
5.3.1 Front position and front velocity . . . 47
5.3.2 Depth at the gate . . . 51
5.3.3 Depth profile . . . 52
5.3.4 Temporal computation cost . . . 54
5.4 Limitations and comparison with the literature . . . 55
5.4.1 Rheological model . . . 55
5.4.2 Model correction . . . 56
5.4.3 Comparison with the literature . . . 58

6 Improved closure: a slope-based formulation 59
6.1 Motivation and rheology derivation . . . 59
6.2 Rheology regimes . . . 61
6.3 Numerical implementation . . . 62
6.3.1 Construction of the driving slope . . . 62
6.3.2 Treatment of the singular regime . . . 64
6.4 Benchmark Result and discussion . . . 65
6.4.1 Regime A . . . 66
6.4.2 Regime B . . . 70
6.4.3 Comparison between three implementations . . . 74
6.4.4 Time computation . . . 77
6.5 Global limitations of the benchmark . . . 78
6.5.1 Limitations related to mudflow application . . . 78
6.5.2 Deposit geometry and material . . . 79

7 Validation on a real-material mudflow 81
7.1 Experimental setup . . . 82
7.1.1 Reference experiment . . . 83
7.2 Rheological characterisation . . . 84
7.2.1 Fitting procedure . . . 84
7.3 Results . . . 87
7.3.1 Channel dynamics . . . 87
7.3.2 Deposit geometry . . . 90
7.4 Discussion and conclusions . . . 94

8 Conclusion and perspectives 95

8.1 Conclusion . . . 95
8.1.1 Summary of contributions . . . 95
8.1.2 Limitations . . . 96
8.2 Perspectives . . . 96
8.2.1 Completing the slope-based formulation of Muchiri *et al.* (2025) . . . 97
8.2.2 A systematic, model-specific calibration of the rheological parameters . . . 97
8.2.3 From a single-phase to a multilayer vertical structure . . . 97
8.2.4 A solver with an intrinsic treatment of the friction source term . . . 98

Appendices **99**

A Order-of-magnitude estimate of the inertial flux term **99**
A.1 Water flow case . . . 99
A.1.1 Characteristic scales . . . 99
A.1.2 Order of magnitude of the different components . . . 99
A.1.3 Comparison of the flux divergence and the friction source term . . . 100
A.1.4 Numerical estimation for typical water flows . . . 100
A.2 Mudflow case . . . 100
A.2.1 Characteristic scales and friction term . . . 100
A.2.2 Order of magnitude of the flux divergence . . . 101
A.2.3 Comparison of the flux divergence and the friction source term . . . 101
A.2.4 Numerical estimation for typical mudflows . . . 101

B Casson model derivation **103**

C Use of Generative AI Tools **107**

Bibliography **109**

List of Figures

1.1 Aerial view showing the destruction of Blatten, Switzerland, on May 29, 2025, one day after the landslide. Credit: Jean-Christophe Bott / Keystone / AP. . . . 2
1.2 Aerial view of the Brumadinho tailings dam failure in Brazil, February 1, 2019. From Lumbroso *et al.* (2021). 2

2.1 Grain size classification, from Coussot (1997) (Picture modified using AI tools). 6
2.2 Schematic interaction energy between two colloidal particles as a function of their separation distance (from Coussot (1997)). 8
2.3 Plug model of a mudflow with a non-Newtonian rheology. (a) Profile view of a flow travelling down a slope of angle θ with h_p the depth of the rigid plug and h the total depth of the flow. (b) Cross-sectional view of the flow, perpendicular to the flow direction. (c) Schematic diagram of the velocity profile, where zero indicates the substrate or surface on which the flow is travelling. From Whorton *et al.* (2025) 9
2.4 Three stages of a debris flow or mudflow life cycle: initiation (a), runout (b) and deposition (c). From Zhang, Li, *et al.* (2021) and Liesse (2026). 10
2.5 Front segregation in a debris flow, with the coarser grains (boulders) migrating towards the front of the flow. From Liesse (2026) and Schaer (2018). 11
2.6 Classification of mass movements on steep slopes as a function of solid fraction and material type. From Coussot and Meunier (1996) (modified using AI tools). 13
2.7 Visual illustration of the four main mass movement types discussed in this section, ordered from solid-like behaviour (top-left) to fluid-like behaviour (bottom-right). 14
2.8 Possible modelling choices for mudflow simulation. Each branch corresponds to one of the modelling axes reviewed in this section. The green boxes mark the choices made in this work: a single-phase, two-dimensional shallow-water formulation with a viscoplastic constitutive law, discretised by a finite-volume method. Graph inspired by Trujillo-Vela *et al.* (2022). 19

4.1 Comparison of the idealised rheological behaviour of a Bingham fluid, of a Herschel-Bulkley fluid with $n = 0.5$ (shear-thinning) and $n = 1.5$ (shear-thickening), of a Casson fluid, and of a Newtonian fluid. 30
4.2 Comparison of the apparent viscosity as a function of the shear rate for the considered rheological models. 34
4.3 Shear stress distribution and velocity profile for a “threshold fluid” in steady uniform flow over an inclined plane (Pastor *et al.* (2004), Liesse (2026)). 36

4.4 Stress as a function of rate of strain at several values of m for regularised local law, from Papanastasiou (1987). 40
4.5 Softplus function $\mathcal{S}(x; M)$ for several values of the sharpness parameter M, compared to its limiting case $\max(0, x)$. As M increases, $\mathcal{S}$ converges pointwise to the ramp function while remaining C^∞ everywhere. 42
4.6 Effect of the regularisation on the Bingham model. Left: local constitutive law $\tau(\dot\gamma)$ with the Papanastasiou substitution (4.12) for several values of the local sharpness parameter m. Right: depth-averaged law $\bar u(\tau_b)$ with the softplus substitution for several values of the dimensionless sharpness parameter M, used in the Watlab implementation. 42
4.7 Effect of the regularisation on the Herschel–Bulkley model in the shear-thinning regime ($n = 0.5$, typical of natural mudflows). Left: local constitutive law with Papanastasiou substitution. Right: depth-averaged law with softplus substitution. 43
4.8 Effect of the regularisation on the Herschel–Bulkley model in the shear-thickening regime ($n = 1.5$). Left: local constitutive law with Papanastasiou substitution. Right: depth-averaged law with softplus substitution. 43
4.9 Effect of the regularisation on the Casson model. Left: local constitutive law with Papanastasiou substitution. Right: depth-averaged law with softplus substitution applied through $\xi_{\text{reg}} = 1 - \mathcal{S}(1 - \xi; M)$. 43

5.1 Schematic of the experimental setup for the viscoplastic dam-break experiments, from Ancey *et al.* (2012). 46
5.2 Front position $x_f(t)$ as a function of time for three mesh sizes ($M = 50$, $\mathrm{CFL} = 0.4$) with regularised rheology, compared with the experimental data of Ancey *et al.* (2012). 48
5.3 Front velocity $u_f(t)$ as a function of time for three mesh sizes ($M = 50$, $\mathrm{CFL} = 0.4$) with regularised rheology, compared with experiments. 49
5.4 Front position $x_f(t)$ for four values of the regularisation parameter M ($l_c = 0.01$ m, $\mathrm{CFL} = 0.4$) with regularised rheology, compared with experiments. . . 50
5.5 Front velocity $u_f(t)$ for four values of M ($l_c = 0.01$ m, $\mathrm{CFL} = 0.4$) with regularised rheology, compared with experiments. 50
5.6 Flow depth $h(x{=}0, t)$ at the gate location for three mesh sizes ($M = 50$, $\mathrm{CFL} = 0.4$) with regularised rheology. The dashed line indicates the theoretical plug-flow arrest height $h_p = 0.0102$ m. 51
5.7 Flow depth $h(x{=}0, t)$ for four values of M ($l_c = 0.01$ m, $\mathrm{CFL} = 0.4$) with regularised rheology. The dashed line indicates $h_p = 0.0102$ m. 52
5.8 Free-surface profiles along the flume axis at $t \in \{0.5,\ 1.0,\ 2.0,\ 5.0,\ 10.0\}$ s for three mesh sizes ($M = 50$, $\mathrm{CFL} = 0.4$) with regularised rheology. 53
5.9 Free-surface profiles along the flume axis at $t \in \{0.5,\ 1.0,\ 2.0,\ 5.0,\ 10.0\}$ s for four values of M ($l_c = 0.01$ m, $\mathrm{CFL} = 0.4$) with regularised rheology. 54

5.10 Comparison of the front position $x_f(t)$ obtained in this study with the regularised rheology and the results from Fernández-Nieto *et al.* (2023) and Muchiri *et al.* (2025), alongside the experimental data. 58

6.1 Schematic of the mean-slope reference frame with non-flat topography, from Muchiri *et al.* (2025). 62
6.2 Front position $x_f(t)$ as a function of time for three mesh sizes ($M = 50$, $\mathrm{CFL} = 0.4$) with regime A rheology, compared with the experimental data of Ancey *et al.* (2012). 66
6.3 Front velocity $u_f(t)$ as a function of time for three mesh sizes ($M = 50$, $\mathrm{CFL} = 0.4$) with regime A rheology, compared with experiments. 67
6.4 Flow depth $h(x{=}0, t)$ at the gate location for three mesh sizes ($M = 50$, $\mathrm{CFL} = 0.4$) with regime A rheology. The dashed line indicates the theoretical plug-flow arrest height $h_p = 0.0102$ m. 68
6.5 Free-surface profiles along the flume axis at $t \in \{0.5,\ 1.0,\ 2.0,\ 5.0,\ 10.0\}$ s for three mesh sizes ($M = 50$, $\mathrm{CFL} = 0.4$) with regime A rheology. 69
6.6 Comparison of the front position $x_f(t)$ obtained in this study with the regime A rheology and the results from Fernández-Nieto *et al.* (2023) and Muchiri *et al.* (2025), alongside the experimental data. 70
6.7 Front position $x_f(t)$ as a function of time for three mesh sizes ($M = 50$, $\mathrm{CFL} = 0.4$) with regime B rheology, compared with the experimental data of Ancey *et al.* (2012). 71
6.8 Front velocity $u_f(t)$ as a function of time for three mesh sizes ($M = 50$, $\mathrm{CFL} = 0.4$) with regime B rheology, compared with experiments. 71
6.9 Flow depth $h(x{=}0, t)$ at the gate location for three mesh sizes ($M = 50$, $\mathrm{CFL} = 0.4$) with regime B rheology. The dashed line indicates the theoretical plug-flow arrest height $h_p = 0.0102$ m. 72
6.10 Free-surface profiles along the flume axis at $t \in \{0.5,\ 1.0,\ 2.0,\ 5.0,\ 10.0\}$ s for three mesh sizes ($M = 50$, $\mathrm{CFL} = 0.4$) with regime B rheology. 73
6.11 Comparison of the front position $x_f(t)$ obtained in this study with the regime B rheology and the results from Fernández-Nieto *et al.* (2023) and Muchiri *et al.* (2025), alongside the experimental data. 74
6.12 Comparison of the front position $x_f(t)$ obtained with the three implementations of the rheology (regularised, Regime A and Regime B) with the experimental data from Ancey *et al.* (2012). 75
6.13 Comparison of the front velocity $u_f(t)$ obtained with the three implementations of the rheology (regularised, Regime A and Regime B) with the experimental data from Ancey *et al.* (2012). 76
6.14 Comparison of the flow depth at the gate $h(x{=}0, t)$ obtained with the three implementations of the rheology (regularised, Regime A and Regime B) with the experimental data from Ancey *et al.* (2012). 77

7.1 Experimental setup of the Polimi benchmark, from Liesse (2026). 82
7.2 Time evolution of the simulated front velocity in the channel and deposit zone for the five rheological parameter sets. 88
7.3 Time evolution of the simulated front velocity, time-shifted so that $t = 0$ corresponds to the passage of the front at the channel outlet. 89
7.4 Longitudinal free-surface profiles along the channel axis at six successive times for the five rheological parameter sets of Table 7.2. Dashed lines mark the channel outlet and the two control points at 40 cm (middle) and 80 cm (upper) from the outlet. 90
7.5 Top view of the final deposit on the horizontal plane. Top left: laser scan of the experimental deposit. Other panels: simulated deposit at $t = 12$ s for each rheological parameter set of Table 7.2. 91
7.6 Top: longitudinal cut of the final deposit along $y = 0.4$ m. Bottom: transverse cut at $x = 0.4$ m. The simulations spread the material more uniformly than the experiment, which exhibits a pronounced peak near the channel outlet. 92
7.7 Maps of the difference $h_{\mathrm{sim}} - h_{\mathrm{exp}}$ at $t = 12$ s for the five rheological parameter sets. RMSE and bias are reported in each panel. 93

List of Tables

4.1 Conceptual classification of sediment-laden flows and associated rheological models, inspired by Gibson *et al.* (2021). 35

5.1 Herschel–Bulkley rheological parameters of the Carbopol ultrez 10 gel used in the experiments of Ancey *et al.* (2012). 46

5.2 Computation time for the benchmark simulations for different mesh sizes and regularisation parameters (CFL = 0.4, 15 seconds of simulated time, AMD Ryzen 7 7735HS, 16 threads). 55

6.1 Computation time for the benchmark simulations for different mesh sizes and closure formulations (CFL = 0.4, 15 seconds of simulated time, AMD Ryzen 7 7735HS, 16 threads). 77

7.1 Initial conditions and measurements for experiment T08, from Liesse (2026). . 83

7.2 Rheological parameters fitted for experiment T08. 87

7.3 Channel metrics for experiment T08: experiment vs. simulations. 87

7.4 Scalar metrics for experiment T08: experiment vs. simulations. 93

CHAPTER 1

Introduction

Mudflows and debris flows are among the most destructive gravity-driven natural hazards. These flows consist of dense mixtures of water, soil, rock and organic matter capable of travelling at high velocity while transporting large quantities of sediments and debris over long distances. Their destructive potential arises from the combination of high density, strong momentum, and the ability to transport large volumes of material far beyond the initiation zone. Front velocities of 5 to 15 m/s are measured for moderately energetic events and peaks of 20 to 30 m/s for the most violent ones. The total released volumes can reach 10^6 to 10^9 m^3 (Iverson (1997) and Coussot and Meunier (1996)). They result, in particular in mountainous regions where they are more likely to occur, in severe damage to infrastructure and, in some cases, in substantial casualties for local populations. Therefore, predicting their propagation, velocity, and deposition area constitutes a major challenge for hazard assessment and risk mitigation.

In the coming decades, the need for reliable mudflow simulation tools will become increasingly important in the context of climate change and growing human exposure to natural hazards. Indeed, many of the factors that control their initiation and propagation are influenced by ongoing environmental changes (Hirschberg *et al.* (2021)). The intensification of extreme rainfall events, the retreat of glaciers, the degradation of permafrost and the increasing prevalence of wildfires all modify, to various extents, hydrological and sedimentological conditions governing slope failures and sediment mobilisation. The precise evolution of mudflow activity remains strongly region-dependent and cannot be reduced to a simple globally uniform trend (Hirschberg *et al.* (2021) and Imaizumi *et al.* (2021)). What can nevertheless be stated with confidence is that the future evolution of mudflow hazards can no longer be assumed to follow the same trends and recurrence patterns as in the past.

Recent events have further highlighted the societal importance of hazards. The 2025 collapse of a glacier-supported rock mass above the village of Blatten, in the Swiss Alps, which mobilised into a debris flow that buried most of the village (Büntgen *et al.* (2025)), is a recent illustration of the threat posed by large-scale natural material mobilisation in a changing environment. A picture of this event is shown in Figure 1.1.



Fig 1.1. *Aerial view showing the destruction of Blatten, Switzerland, on May 29, 2025, one day after the landslide. Credit: Jean-Christophe Bott / Keystone / AP.*

Another striking example is the 2019 Brumadinho tailings-dam failure in Brazil that demonstrated the destructive potential of human-induced mudflows generated by industrial infrastructure failures, causing catastrophic loss of life and widespread environmental damage (Lumbroso *et al.* (2021)). Although their triggering mechanisms differ fundamentally, both events highlight the critical importance of predictive numerical tools capable of simulating flow propagation and sediment deposition on complex topographies. An illustration of the Brumadinho event is shown in Figure 1.2.



Fig 1.2. *Aerial view of the Brumadinho tailings dam failure in Brazil, February 1, 2019. From Lumbroso* et al. *(2021).*

The present thesis, built on the previous master's thesis of Liesse (2026), pursues two main objectives: to deepen the understanding of the challenges associated with mudflow simulation and to improve a numerical tool dedicated to such flows within the existing Watlab framework. Watlab[1] is a finite-volume shallow-water solver developed at UCLouvain currently used for various applications, including the simulation of Newtonian free-surface flows in the field of river hydraulics and flood inundation studies. More broadly, this work seeks to contribute to the development of numerical tools for mudflow simulation and to provide a solid basis for future research and improvements.

This thesis is structured as follows. Chapter 2 presents the relevant state of the art: it first describes the physical nature of mudflows and the properties that distinguish them from other types of sediment-laden flows. Then, it presents the main modelling strategies described in the literature in order to motivate the choice of the numerical approach adopted in this work. Chapter 3 presents the shallow-water solver into which the selected mudflow rheology have been implemented, recalls the mathematical framework of the shallow-water equations, and details the modifications introduced to the original solver in order to handle the friction-dominated regime characteristic of mudflows. Chapter 4 provides a review of rheological models considered for mudflows and describes their implementation in Watlab. Chapter 5 shows how the resulting implementation was validated based on experimental data from the literature and includes a sensitivity analysis of the model parameters. The results are then compared with other numerical models using the same datasets in order to cross-validate the model. Chapter 6 then documents the corrections and improvements to the model which was made based on the results of the previous chapter. Then, the new model implementation is validated on the same experimental data. Chapter 7 provides an independent validation using an experimental campaign, which was a part of the thesis of Liesse (2026). Finally, the main conclusions and perspectives of this work are summarised in Chapter 8.

[1] `https://sites.uclouvain.be/hydraulics-group/watlab/index.html`

CHAPTER 2

State of the art

This chapter presents the state of the art in mudflow modelling. Some figures and sources are directly inherited from the state of the art established in the master's thesis of Liesse (2026).

2.1 Definition of a mudflow

2.1.1 Physical description

A mudflow is, in essence, a suspension of solid particles in water in which the solid fraction is so high that the mixture no longer behaves as a dilute sediment-laden flow but as a continuous, dense fluid (Iverson (1997), Coussot and Meunier (1996), and Coussot (1997)). The solid content typically occupies between 40 and 80 % of the bulk volume, with a bulk density ρ_m usually between 1500 and 2500 kg/m^3. That is, between 1.5 and 2.5 times that of water (Iverson (1997)).

Mudflows are part of the broader family of *debris flows*, which are defined as fast-moving, gravity-driven flows of mixed water and sediment (Iverson (1997) and Coussot and Meunier (1996)). What distinguishes mudflows from other debris flows is the nature of the solid load: clays and silts dominate the mass, while coarser grains (sand, gravel) are present in much smaller proportions. The fine-particle fraction is typically high enough for inter-particle cohesive interactions to control the macroscopic behaviour. As a consequence, mudflows behave like a thick viscous fluid rather than a moving collection of grains.

From a more detailed physical perspective, the solid phase can be separated into two main groups which approximately correspond to two distinct size classes (Coussot (1997)):

- **Fine particles**, usually clay particles, which are smaller than $2\,\mu\mathrm{m}$. Fine particles are colloidal[1] in nature, with a large area-to-volume ratio. Their behaviour is dominated by surface electrochemical forces.
- **Large grains**, which are larger than $2\,\mu\mathrm{m}$. Large grains (silt, sand, gravel, pebbles, boulders) are mostly inert fragments of rock.

[1] A colloid is a system in which particles of one phase, with sizes typically ranging from $1\,\mathrm{nm}$ to $1\,\mu\mathrm{m}$, are finely dispersed in a continuous medium. At this scale, the surface-to-volume ratio is so large that interfacial forces (electrostatic double-layer repulsion and van der Waals attraction) dominate over gravitational effects.

The boundary between the two classes is not strictly fixed: under some flow conditions, particles as large as $100\ \mu\mathrm{m}$ may still exhibit colloidal behaviour.

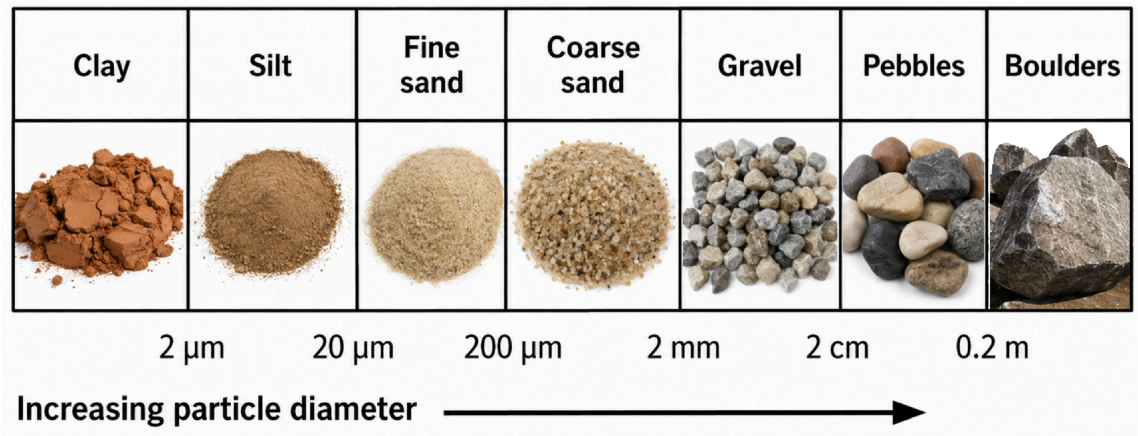


Fig 2.1. *Grain size classification, from Coussot (1997) (Picture modified using AI tools).*

The water itself is not a simple inert fluid and two categories of water can be distinguished in a mudflow (Coussot (1997)):

- **Adsorbed water**, which is the water bound to the surface of the fine particles by electro-chemical forces. It forms a thin, strongly held layer that does not behave as free water. It does not evaporate below $300^{\circ}\mathrm{C}$ and exhibits a high viscosity.
- **Free water**, which is the water that is not trapped in the pore space and can flow freely through the mixture. Free water evaporates completely around $105^{\circ}\mathrm{C}$ and has a viscosity close to $10^{-3}\ \mathrm{Pa.s}$ at $20^{\circ}\mathrm{C}$ away from the particles.

In engineering practice, adsorbed water is often considered as part of the solid phase and the free water as the true interstitial fluid.

At the scale of engineering modelling, this microstructure is not explicitly represented. The flow is represented as a single, homogeneous, continuous medium of density ρ_m, with mechanical properties chosen to encapsulate the average effect of the complex solid-fluid interactions at the particle scale. This so-called *single-phase assumption* is the first major simplification on which this work, and most existing numerical models of mudflows, are based. This is specifically justified for mudflows by the high fine-particle content, which makes the mixture sufficiently homogeneous and cohesive at the scale of interest. The alternatives, which become necessary for flows with a higher coarse-particle content, are discussed in Section 2.3.1.

2.1.2 The viscoplastic behaviour: yield stress and plug zones

The property that most distinguishes mudflows from water, and which controls almost every modelling choice in this master's thesis, is that a mudflow can sustain a finite shear stress without flowing. In a gravity-driven flow, the driving stress comes from the component of the mixture's weight acting along the slope. Whether the material flows or remains static is then governed by the balance between this driving stress and the material's internal resistance. For a homogeneous Newtonian fluid such as water, internal resistance vanishes as the shear rate goes to zero, so any non-zero driving stress produces deformation. Water on an inclined surface always flows downhill (neglecting surface tension). In contrast, a mudflow behaves as a *viscoplastic* material. A critical shear stress exists, called the *yield stress* τ_y, below which the material behaves as a rigid solid and does not flow, and above which it behaves as a viscous fluid (Coussot and Meunier (1996) and Iverson (1997)).

The physical origin of the yield stress in mudflows lies in the cohesive interactions between the clay and silt particles that make up most of the fine fraction of the mixture (Coussot and Meunier (1996)). At rest, these particles form an interconnected network maintained by electrostatic and colloidal forces. As long as the applied shear stress is below the yield stress, it is too weak to break this network and the material resists to the load without flowing. Once the applied stress exceeds τ_y, the network structure breaks, the particles rearrange and the material starts to flow.

From a colloidal physics perspective, the cohesive network results from the balance between attractive van der Waals forces[2] and repulsive forces due to the overlapping of electrical double layers[3]. At short range, the van der Waals attraction dominates and particles tend to stick together, while at longer range, the electrostatic repulsion dominates and prevents particles from coming too close (see Figure 2.2). The combination of these forces creates an equilibrium position at a certain distance between the particles. The particles become "trapped" in this position and form a stable, cohesive network without directly touching each other. The yield stress is the stress required to pull the particles out of this equilibrium position and break the network so that the mud can start to flow (Coussot (1997)).

[2] Short-range attractive forces between neutral particles, arising from potential electrical fluctuations in their electronic fields

[3] Charged particles in water attract a diffuse cloud of counter-ions, when two such clouds overlap, they produce an electrostatic repulsion.

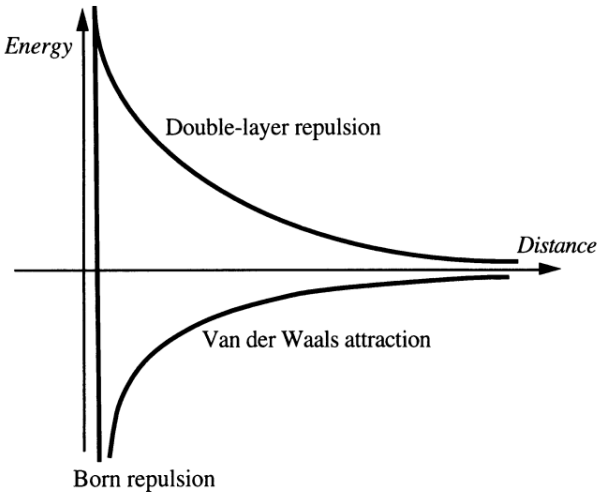


Fig 2.2. *Schematic interaction energy between two colloidal particles as a function of their separation distance (from Coussot (1997)).*

This behaviour is taken into account in the modelling by using an appropriate *rheological law*. It is a relation between the shear stress τ that the material supports and the shear rate $\dot{\gamma}$ at which it deforms. For a Newtonian fluid such as water, this relation reduces to a simple linear relationship $\tau = \mu\dot{\gamma}$, where μ is the dynamic viscosity and passes through the origin. For a viscoplastic material, the relation does not pass through the origin. It intersects the τ-axis at $\tau = \tau_y$, meaning that no shear rate occurs below this threshold. The specific shape of the curve above τ_y characterises the post-yield behaviour which is described by diverse constitutive laws that will be detailed and compared in Chapter 4.

This single property has two implications that are central to mudflow modelling and thus to the rest of this master's thesis.

The first implication concerns the internal structure of the flow. Consider the case of a steady uniform flow of thickness h over an inclined plane at an angle θ. A momentum balance on a column of mixture shows that the shear stress grows linearly with depth, from zero at the free surface to a maximum $\tau_b = \rho_m g h \sin\theta$ at the bed. Below the depth at which this driving stress equals τ_y, the material is sheared and behaves as a viscous fluid. Above it, the driving stress is insufficient to overcome the yield stress and the material moves as a rigid solid. This upper region is the *plug zone*, of thickness h_p given by:

$$h_p = \frac{\tau_y}{\rho_m g \sin\theta}$$

The velocity profile of a mudflow is therefore not the simple parabolic Poiseuille profile of a Newtonian fluid, but a combination of a sheared lower zone of thickness $h - h_p$ and a constant-velocity plug region of thickness h_p (see Figure 2.3).

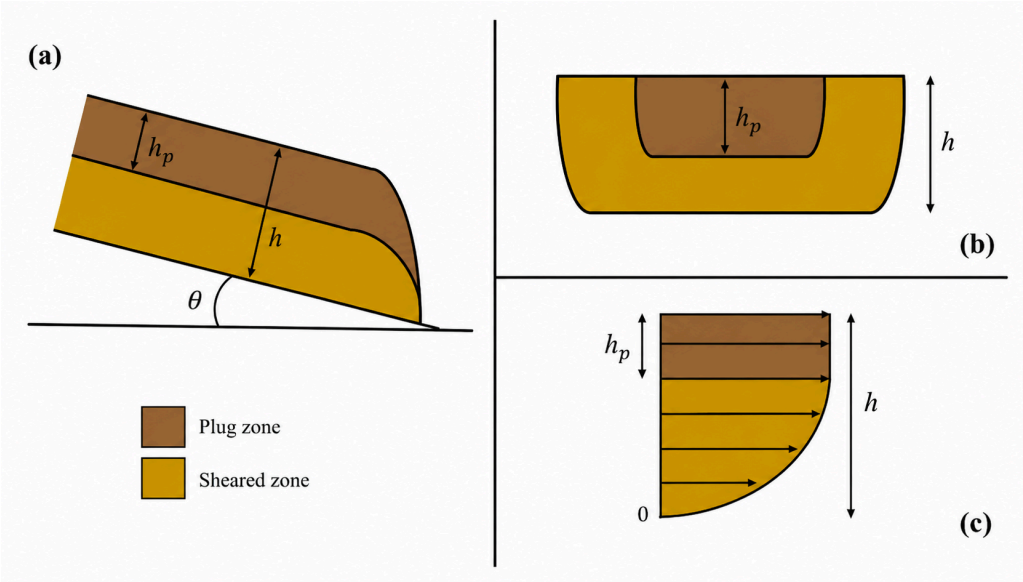


Fig 2.3. *Plug model of a mudflow with a non-Newtonian rheology. (a) Profile view of a flow travelling down a slope of angle* θ *with* h_p *the depth of the rigid plug and* h *the total depth of the flow. (b) Cross-sectional view of the flow, perpendicular to the flow direction. (c) Schematic diagram of the velocity profile, where zero indicates the substrate or surface on which the flow is travelling. From Whorton* et al. *(2025)*

The second implication concerns the cessation of the flow. As mentioned above, a water flow on an inclined surface will continue to flow as long as the driving stress is non-zero. In contrast, a mudflow can come to a complete stop, even on a slope. If the thickness becomes small enough that the basal shear stress τ_b falls below the yield stress τ_y, the flow will stop and remain static until further material is added to increase the thickness and driving stress again.

2.1.3 Life cycle: initiation, runout, deposition

The life cycle of a mudflow can be divided into three main stages: initiation, runout, and deposition (Iverson (1997), Iverson *et al.* (1997), and Zhang, Li, *et al.* (2021)). An illustration of these stages is given in Figure 2.4.

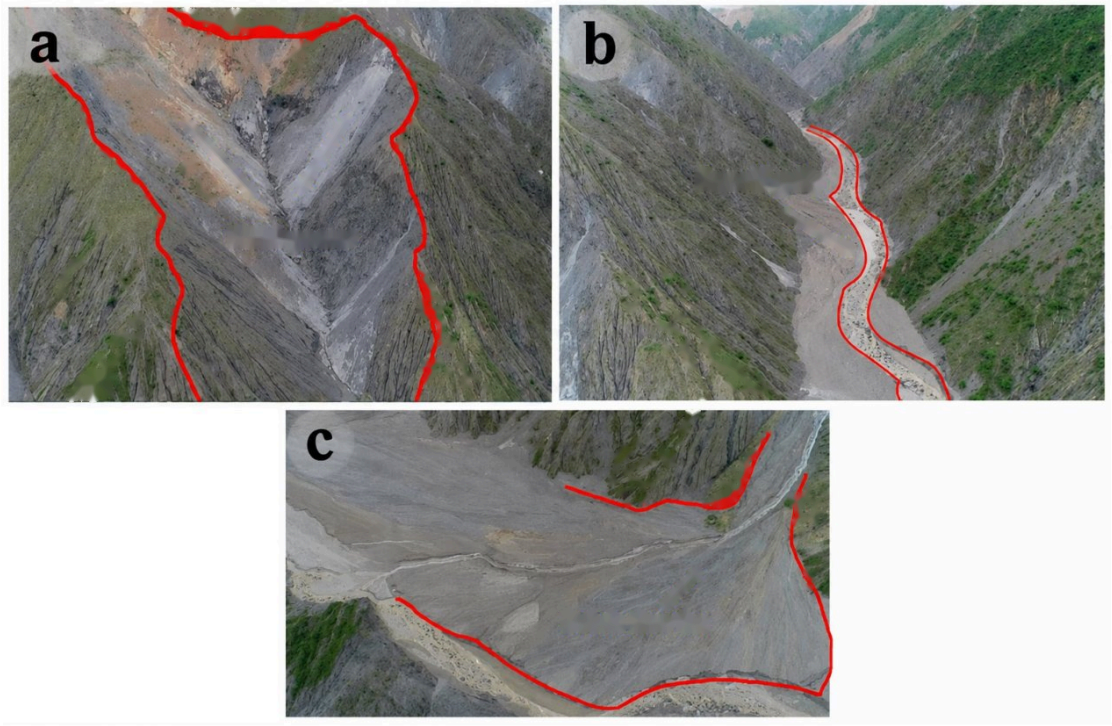


Fig 2.4. *Three stages of a debris flow or mudflow life cycle: initiation (a), runout (b) and deposition (c). From Zhang, Li,* et al. *(2021) and Liesse (2026).*

Initiation

The flow begins with the failure of a saturated mass of material on a hillslope, which can be triggered by various phenomena such as prolonged or intense rainfall, snow or ice melt, seismic activity, remobilisation of a previous deposit, *etc*. Nonetheless, it is worth noting that the mass does not necessarily have to be saturated at the moment of failure. In some cases, the initial failure can occur in a dry state, and the material can then entrain water as it moves downslope, leading to the development of a mudflow. The underlying mechanisms of the initiation phase are complex and involve a combination of slope stability, pore-pressure dynamics and granular effects. In this work, we focus on the runout and deposition phases, and we do not attempt to model the initiation process. The reader interested in this phase can refer to Iverson *et al.* (1997) for a detailed review of the physical processes involved.

Runout

Once the flow is initiated, it starts to move downslope under the influence of gravity. This is the phase during which the mudflow does most of its damage: it can travel several kilometres, reach high velocities, erode the bed and the banks, and entrain additional material along the way. In debris flows specifically, the runout phase is also accompanied by front segregation, in which the coarser grains tend to migrate towards the front of the flow while the finer particles remain in the body (see Figure 2.5). The presence of the biggest grains at the front can lead to the formation of a coarse-grained, boulder-rich frontal surge that is particularly destructive (Iverson *et al.* (1997) and Schaer (2018)).



Fig 2.5. *Front segregation in a debris flow, with the coarser grains (boulders) migrating towards the front of the flow. From Liesse (2026) and Schaer (2018).*

Deposition

The flow eventually loses mobility and comes to rest through the mechanism described in Section 2.1.2, when $h \leq h_p$ everywhere. This transition is gradual: the front decelerates first and acts as a natural dam for the upstream material, which piles up behind it before stopping (Iverson (1997) and Major (1997)). Once at rest, the deposit does not become inert immediately. The interstitial fluid drains progressively, the solid skeleton consolidates, and the residual shear strength of the material increases substantially. As a result, remobilisation of a stopped deposit generally requires more energy than the initial failure, which is why old deposits can remain stable on relatively steep slopes for long periods.

2.2 Classification of sediment-laden gravity flows

2.2.1 Mudflows in the spectrum of sediment-laden flows

Mudflows constitute merely one category among the various types of sediment-laden gravity flows. The classification of these flows is a complex topic as they span a wide continuous spectrum of behaviours and the boundaries between different types of flows are not always clear-cut. At one end of this spectrum, landslides behave as solid bodies, sliding downslope without significant internal deformation. At the other end, stream flows are dilute fluid-dominated transports of sediment, in which the solid load is carried by suspension[4] and bedload[5]. Their solid fraction is typically below 5 %. Between these two extremes there is a wide variety of flows, in order of decreasing fluid dominance, hyperconcentrated flows (5–40 % solid fraction) and debris flows (40–80 % solid fraction). It is important to note that there is no universally accepted classification scheme for these flows. The interval values of solid fraction given here are an approximation based on several papers (Iverson (1997), Coussot and Meunier (1996), and Pierson and Costa (1987)) and should not be taken as strict thresholds but rather as a general guideline.

Among debris flows, one can further distinguish mudflows, which are dominated by the fine fraction, from granular flows, which are dominated by the coarse fraction. In Figure 2.6, these three terms appear as adjacent regions of the rapid-motion regime. Here and in the rest of this work, “mudflow” is used in the more common sense of a cohesive-end member of the broader debris-flow family.

[4] Transport mode in which the particles are held in suspension.
[5] Transport mode in which the particles move along the bed.

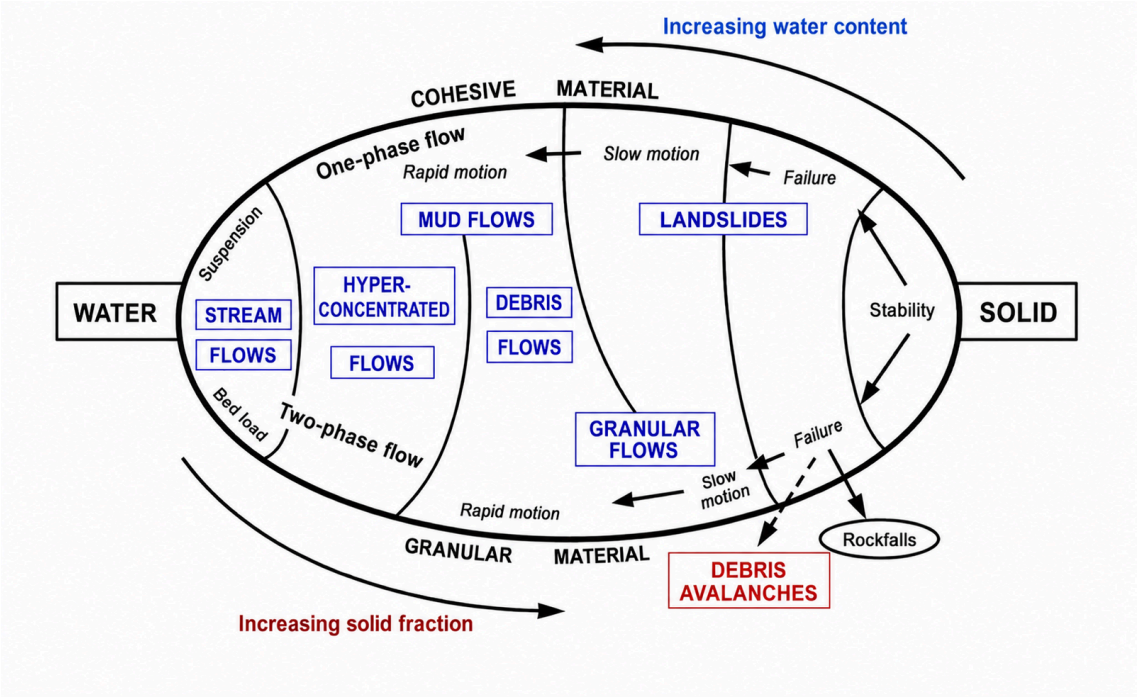


Fig 2.6. *Classification of mass movements on steep slopes as a function of solid fraction and material type. From Coussot and Meunier (1996) (modified using AI tools).*

Coussot and Meunier (1996) proposed one of the most widely used classification schemes for these flows, based on two factors: the solid volume fraction and the nature of the solid phase (i.e. its mineralogy). The first factor controls how dominant the solid phase is in the bulk behaviour of the flow. The second factor, which ranges from cohesive clays to non-cohesive cobbles determines the type of inter-particle interactions. The combination of these two factors gives rise to a wide variety of behaviours that is summarised in Figure 2.6. Some of the mass movements identified in this figure are illustrated in Figure 2.7. The transition from a stream or hyperconcentrated flow to a debris flow occurs when the solid concentration becomes large enough for inter-particle interactions to dominate over fluid dynamics. The transition from a debris flow to a landslide-like motion occurs when the solid concentration is so large that the fluid behaviour becomes negligible. Within the debris-flow regime, the nature of the solid phase further separates mudflows, in which clay-driven cohesive interactions dominate, from granular flows, in which frictional and collisional contacts between coarse grains dominate. Mudflows, the object of this thesis, therefore correspond to the cohesive, single-phase, rapid-motion sector of Figure 2.6.



(a) *Landslide near Cusco, Peru (2018). Source: photo by Galeria del Ministerio de Defensa del Perú, CC BY 2.0.*



(b) *Granular debris flow near Bondo, Switzerland. Source: RTBF.*



(c) *Mudflow in the Brumadinho tailings dam failure, Brazil, February 1, 2019. Source: Lumbroso* et al. *(2021).*



(d) *Hyperconcentrated flow in Valais, Switzerland, after the 2024 flood. Source: Keystone/Jean-Christophe Bott.*

Fig 2.7. *Visual illustration of the four main mass movement types discussed in this section, ordered from solid-like behaviour (top-left) to fluid-like behaviour (bottom-right).*

2.2.2 Characterising the dominant regime: the Bagnold number

Another, more quantitative way to characterise the dominant regime of a sediment-laden flow is the *Bagnold number*, introduced by Bagnold (1954) and later revisited by Hunt *et al.* (2002). It is a dimensionless number that compares grain inertia to viscous forces in the flow, and it distinguishes regimes dominated by viscous interactions (low Bagnold number) from regimes dominated by grain inertia (high Bagnold number). For example, in a mudflow the shear stress is mostly supported by cohesive interactions between fine particles, and therefore viscous forces dominate, and the Bagnold number is low. In a granular debris flow with a high coarse-particle content, the shear stress is supported by frictional and collisional contacts between grains. In this case, grain inertia dominates, and the Bagnold number is high.

The Bagnold number is defined as:

$$N_{\mathrm{BAG}} = \frac{\rho_s \, d_s^2 \, \lambda^{1/2} \, \dot{\gamma}}{\mu_f}, \tag{2.1}$$

where ρ_s and d_s are the density and characteristic diameter of the grains, μ_f the viscosity of the interstitial fluid, $\dot{\gamma}$ the local shear rate, and λ the linear concentration of grains, related to the volumetric concentration C_V and to the maximum packing concentration $C_{V,\max}$ by $\lambda = \left[(C_{V,\max}/C_V)^{1/3} - 1\right]^{-1}$. The variable λ measures the ratio between the grain diameter and the mean inter-grain spacing, and it diverges as $C_V \to C_{V,\max}$ reflecting the fact that grain interactions become arbitrarily strong as the packing limit is approached (Bagnold (1954), Iverson (1997), and Hunt *et al.* (2002)).

Three regimes are conventionally identified from this number (Hunt *et al.* (2002)):

- **Viscous regime**, for $N_{\mathrm{BAG}} < 40$. The flow is dominated by viscous interactions, and the shear stress is proportional to the shear rate. This regime corresponds to mudflows and hyperconcentrated flows.
- **Grain-inertia regime**, for $N_{\mathrm{BAG}} > 450$. The flow is dominated by grain inertia, and the shear stress is proportional to the square of the shear rate. This regime corresponds to granular debris flows.
- **Transition regime**, for $40 < N_{\mathrm{BAG}} < 450$. Both viscous and grain-inertia effects are significant, and the flow exhibits an intermediate more complex behaviour. This regime corresponds to flows that sit between mudflows and granular debris flows.

For natural mudflows, characterised by a high content of fine particles and a relatively small mean grain diameter d_s, the Bagnold number is typically low, placing the flow in the viscous regime, or at most in the transitional one. This confirms the physical justification introduced in Section 2.1.2 for adopting a viscoplastic constitutive law as the basis of the rheological description. It is consistent both with the observed mechanical behaviour of the mixture and with the dominance of viscous over collisional stresses predicted by the Bagnold argument. As further discussed in Chapter 4, the rheological models adopted for mudflows generally show a linear relationship between shear stress and shear rate above the yield stress, with some models including a mild non-linearity to account for the transitional regime.

2.3 Modelling strategies

The modelling of mudflows is a complex task that involves choices regarding the representation of the phase, the spatial dimensionality, the constitutive law and the numerical scheme used to discretise the resulting equations. This section summarises the main approaches discussed in Trujillo-Vela *et al.* (2022).

2.3.1 Phase representation

Three levels of phase representation are commonly distinguished: the single-phase approach, the mixture approach and the multiphase approach.

- The **single-phase approach** represents the material as a continuous medium with a single velocity field and a single set of equations governing its motion. The solid-fluid coupling is absorbed into an effective rheology that captures, at the macroscopic scale[6], the average effect of the complex interactions between the solid and fluid phases. This is the simplest and the computationally cheapest approach, and the most appropriate method related to the assumption discussed in Section 2.1.1. Phenomena that require an explicit distinction between phases, such as grain-size segregation, front segregation, *etc.* are by definition disregarded by this approach.
- The **mixture approach** represents the material as a homogeneous continuum composed of both solid and fluid phases, whose properties are expressed through weighted averages using the volumetric fraction of each phase. Unlike the single-phase approach, the density, velocity and stress fields are defined as averaged quantities over the phases, while the flow is still governed by a single momentum equation for the whole mixture. In its simplest form, the solid fraction is assumed to be constant, so that no relative motion exists between the phases and the mixture approach is practically equivalent to the single-phase approach. More advanced mixture models additionally introduce a transport equation for the solid volumetric fraction, allowing the local concentration to evolve in space and time while preserving a unique velocity field. This enables the modelling of erosion or deposition processes more naturally, at the price of an additional equation.
- The **multiphase approach** represents the material as a collection of distinct phases. Each phase is given its own velocity field, volume fraction and a set of mass and momentum equations. Relative motion between the phases is explicitly modelled, and the coupling between phases is captured through interphase exchange terms in the equations. This approach is the most detailed and computationally expensive.

For mudflows, the single-phase approach is widely used and considered adequate at engineering accuracy because the dominant dissipation mechanism is the viscoplastic behaviour of the fine-particle suspension rather than the multiphase interactions. The present work adopts this approach.

[6] The scale at which the flow is considered as a continuum and the microstructure is not explicitly resolved

2.3.2 Spatial dimensionality

The spatial dimensionality of the model is another important choice in the modelling strategy. A fully three-dimensional (3D) resolution of the Navier-Stokes equations with a viscoplastic constitutive law would be the most accurate representation of the flow and is in principle possible with modern computational resources (see for example Zhang, Chen, *et al.* (2021)). At geohazard scales, however, where domains of several kilometres and flow depths of several metres are common, the computational cost of a 3D model becomes prohibitive.

A common alternative is to exploit the geometric characteristics of actual flows: the horizontal extent of a mudflow, typically several hundred metres to several kilometres, is much larger than its depth, which rarely exceeds a few metres. This scale separation justifies a depth-averaging of the Navier-Stokes equations, in which the vertical structure of the flow is integrated out, and the flow is represented by two-dimensional (2D) equations for the depth-averaged velocity and flow thickness. This is the so-called Shallow Water Equations (SWE) approach, originally introduced by Barré de Saint-Venant (1871) for the case of Newtonian water flows. In the case of mudflows and other threshold fluids, they retain the mass and the depth-averaged momentum balance, while the vertical structure of the flow, in particular the precise velocity profile between the plug and the sheared zones, is absorbed into closures for the depth-averaged momentum flux and for the basal shear stress. This is the approach adopted in this work.

A natural refinement of the standard monolayer SWE is the multilayer SWE approach, in which the flow depth is discretised into several layers, each with its own velocity and thickness (Fernández-Nieto *et al.* (2023)). This allows to capture the vertical structure of the flow more accurately, and allows modelling phenomena such as vertical segregation or the evolution of the plug zone. However, it also increases the computational cost and the complexity of the model. It can be seen as an intermediate step between the monolayer SWE and the full 3D approach.

2.3.3 Numerical discretisation schemes

The third modelling choice concerns the numerical scheme used to discretise the equations. Two main categories of numerical methods exist (Trujillo-Vela *et al.* (2022)):

- ***Mesh-based methods*** where the computational domain is discretised into a fixed mesh of cells, and the equations are solved cell by cell.
  - **Finite Difference Methods (FDM)** place the variables at discrete points in space and approximate the derivatives in the equations by finite differences between these points. They are simple to implement but can struggle with complex geometries and unstructured meshes. Moreover, they are not well-suited for handling shocks and discontinuities, which are common in debris flows.

  - **Finite Element Methods (FEM)** represent the solution as a linear combination of basis functions defined on the mesh elements. They are flexible and can handle complex geometries and unstructured meshes, but they can be computationally expensive and may require special treatment to capture shocks and discontinuities.
  - **Finite Volume Methods (FVM)** integrate the equations over control volumes defined by the mesh cells and apply conservation principles to compute fluxes across cell boundaries. They are particularly well-suited for handling shocks and discontinuities, and they can be implemented on structured or unstructured meshes. This is the reason finite-volume methods dominate the literature on shallow-water models (Trujillo-Vela *et al.* (2022)), and it is the category to which the Watlab solver used in this work belongs.

- ***Mesh-free methods*** where the computational domain is represented by a set of discrete particles or points, and the equations are solved by tracking the interactions between these particles.

  - **Smoothed Particle Hydrodynamics (SPH)** represents the flow as a collection of interpolation particles, each carrying properties such as mass, velocity, and density. The equations are solved by computing the interactions between these particles using kernel functions. SPH is particularly well-suited for handling free surfaces and large deformations. Its cost, however, scales steeply with the number of particles needed for a representative simulation.
  - **Discrete Element Methods (DEM)** go one step further and represent the flow as a collection of individual grains interacting through contact, friction, and optionally cohesion. DEM is the most direct representation of granular debris flows but is prohibitively expensive at the geohazard scales and is intrinsically designed for purely granular systems without an interstitial fluid phase, which makes it ill-suited to mudflow modelling.

2.3.4 Summary of the main modelling choices

A graphical representation of the main modelling possibilities is given in Figure 2.8. The choices made in this work are highlighted in green and correspond to a single-phase, two-dimensional shallow-water formulation with a viscoplastic constitutive law, discretised by a finite-volume method. This combination is consistent with the physical characteristics of mudflows established in Section 2.1:

- The single-phase representation is justified by the homogeneous, fine-particle dominated nature of mudflows.
- The shallow-water approach is justified by the large difference in scale between the horizontal extent and the depth of the flow, and allows capturing the main dynamics while keeping the computational cost manageable.

- The viscoplastic constitutive law is justified by the presence of a yield stress and the dominance of viscous interactions in mudflows, as discussed in Section 2.1.2.
- The finite-volume method is justified by its suitability for handling shocks and discontinuities while being computationally efficient.

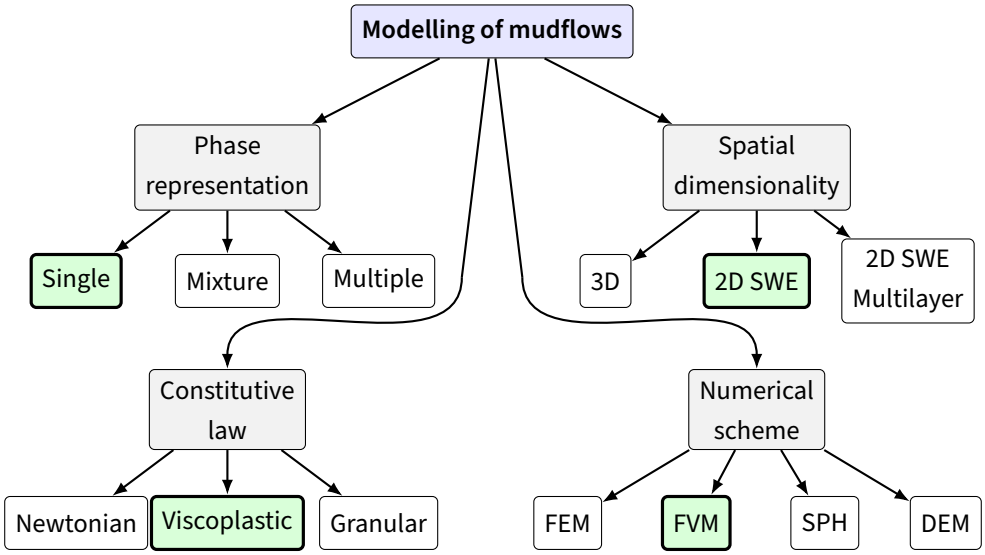


Fig 2.8. *Possible modelling choices for mudflow simulation. Each branch corresponds to one of the modelling axes reviewed in this section. The green boxes mark the choices made in this work: a single-phase, two-dimensional shallow-water formulation with a viscoplastic constitutive law, discretised by a finite-volume method. Graph inspired by Trujillo-Vela* et al. *(2022).*

CHAPTER 3

Shallow Water Solver and adaptation for mudflows

Building on the modelling choices presented at the end of Chapter 2, this chapter focuses on the numerical solver in which the mudflow rheology will be implemented.

3.1 Shallow Water Equations

3.1.1 Derivation framework

The Shallow Water Equations (SWE), also known as the Saint-Venant equations, are derived from a vertical integration of the incompressible Navier-Stokes equations, which govern the motion of a fluid and are given by:

$$\begin{cases} \nabla \cdot \mathbf{u} = 0 \\ \frac{\partial \mathbf{u}}{\partial t} + (\mathbf{u} \cdot \nabla)\mathbf{u} = -\frac{1}{\rho}\nabla p + \nu \nabla^2 \mathbf{u} + \mathbf{g} \end{cases} \tag{3.1}$$

where $\mathbf{u}$ is the velocity field, p is the pressure, ρ is the density, ν is the kinematic viscosity, and $\mathbf{g}$ is the gravitational acceleration.

Their main assumptions are that the horizontal length scales are much larger than the vertical length scale, and that the vertical velocity is negligible compared to the horizontal velocities. The SWE consist of a set of hyperbolic partial differential equations that describe the conservation of mass and momentum in a fluid flow.

3.1.2 Governing equations

The system is formulated in the horizontal plane (x, y). The unknowns are the flow depth $h(x, y, t)$ [m] and the depth-averaged velocity components $u(x, y, t)$ [m/s] and $v(x, y, t)$ [m/s] in the x and y directions, respectively.

By defining the specific discharge as $q_x = hu$ [m^2/s] and $q_y = hv$ [m^2/s], the SWE can be expressed in a conservative form.

Continuity equation

The depth-averaged continuity equation, which represents the conservation of mass, is given by:

$$\frac{\partial h}{\partial t} + \frac{\partial (q_x)}{\partial x} + \frac{\partial (q_y)}{\partial y} = 0 \tag{3.2}$$

The source term on the right-hand side is zero here, as no mass sources or sinks such as rainfall or infiltration are considered.

This equation states that, over a control volume, the variation of the flow depth h over time is balanced by the net flux of water entering or leaving the control volume through its boundaries.

Momentum equations

The depth-averaged momentum equations, which represent the conservation of momentum in the x and y directions, are given by:

$$\begin{cases} \frac{\partial q_x}{\partial t} + \frac{\partial}{\partial x}\left(\frac{q_x^2}{h} + \frac{1}{2}gh^2\right) + \frac{\partial}{\partial y}\left(\frac{q_x q_y}{h}\right) = gh(S_{0x} - S_{fx}) \\ \frac{\partial q_y}{\partial t} + \frac{\partial}{\partial x}\left(\frac{q_x q_y}{h}\right) + \frac{\partial}{\partial y}\left(\frac{q_y^2}{h} + \frac{1}{2}gh^2\right) = gh(S_{0y} - S_{fy}) \end{cases} \tag{3.3}$$

The advective momentum fluxes $q_x^2/h = u\,q_x$ and $q_y^2/h = v\,q_y$ describe the transport of momentum in the respective coordinate directions. The cross terms $q_x\,q_y/h = v\,q_x = u\,q_y$ represent transverse momentum transport. The hydrostatic pressure contribution $\frac{1}{2}gh^2$ arises from the vertical integration of the linear pressure distribution over the depth.

The source terms on the right-hand side are:

- **Bed slope:** S_0 which represents the gravitational driving force of the flow, and is defined as $S_{0x} = -\frac{\partial z_b}{\partial x}$ and $S_{0y} = -\frac{\partial z_b}{\partial y}$, where z_b is the bed elevation.
- **Friction slope:** S_f which accounts for the resistance to flow due to bed friction.

3.1.3 Closure relation

To close the system of equations, we need to specify a closure relation for the friction slope S_f. For Newtonian fluids like water, this is commonly done using the Manning's equation:

$$S_f = \frac{n^2(q_x^2 + q_y^2)}{h^{10/3}} \tag{3.4}$$

where n is the Manning's roughness coefficient, which depends on the characteristics of the bed and of the flow.

For non-Newtonian fluids, such as mudflows, the closure relation is more complex and can be based on a rheological model. This aspect is discussed extensively in Chapter 4.

3.2 Numerical solver

In Watlab, the SWE are solved using a finite volume method on a mesh owing to its ability to handle discontinuities and unstructured meshes. The computational domain is discretised in a set of triangular control volumes, and the governing equations are integrated over each control volume to yield a system of ordinary differential equations in time.

Using a vectorial formulation, the system can be written in the following compact form:

$$\frac{\partial U}{\partial t} + \frac{\partial F(U)}{\partial x} + \frac{\partial G(U)}{\partial y} = S(U) \tag{3.5}$$

With

$$U = \begin{pmatrix} h \\ q_x \\ q_y \end{pmatrix}, \quad F(U) = \begin{pmatrix} q_x \\ \frac{q_x^2}{h} + \frac{1}{2}gh^2 \\ \frac{q_x\, q_y}{h} \end{pmatrix}, \quad G(U) = \begin{pmatrix} q_y \\ \frac{q_x\, q_y}{h} \\ \frac{q_y^2}{h} + \frac{1}{2}gh^2 \end{pmatrix}, \quad S(U) = \begin{pmatrix} 0 \\ gh(S_{0x} - S_{fx}) \\ gh(S_{0y} - S_{fy}) \end{pmatrix}$$

3.2.1 Finite volume discretisation

Applying the finite volume method, the previous continuous system is discretised in space, leading to the following update formula over cell i of area Ω_i:

$$U_i^{n+1} = U_i^n - \frac{\Delta t}{\Omega_i} \sum_{j=1}^{3} \mathbf{T}_j^{-1} \mathbf{F}_j\big(\bar{U}_j\big)\, L_j + \Delta t\, S_i \tag{3.6}$$

where $\mathbf{F}_j$ is the numerical flux through face j of length L_j, obtained by solving a Riemann problem at each interface using an LHLLC[1] solver, and $\mathbf{T}_j$ is the rotation matrix aligning the local face normal with the x-axis.

3.2.2 Current implementation

The solver currently implemented in Watlab uses a first-order operator splitting method where the fluxes are computed first without any source term, and then the source term is applied as a correction.

The *update Equation* 3.6 is thus carried out in two successive steps:

- **Flux update:** $U_i^* = U_i^n - \frac{\Delta t}{\Omega_i} \sum_{j=1}^{3} \mathbf{T}_j^{-1} \mathbf{F}_j\big(\bar{U}_j\big)\, L_j$
- **Explicit source term update:** $U_i^{n+1} = U_i^* + \Delta t\, S(U_i^n)$

[1] The (L)HLLC solver is an approximate Riemann solver that estimates the interface flux from the wave structure of the local Riemann problem, adapted here to the shallow-water equations with wet/dry fronts.

This approach allows for a straightforward implementation of the source term and a decoupling of the flux and source term computations.

However, as a consequence of this decoupling, mass transfer (i.e. variation of h) is driven exclusively by the fluxes, while the source term only acts on the momentum equations in the subsequent step. To prevent the source term from inducing negative specific discharges, a clipping is applied to them: if their values become negative after the source term update, they are reset to zero.

3.3 Limitations for mudflow applications

The splitting scheme described in Section 3.2.2 performs well for water flows with Manning friction, since the friction slope S_f is small compared to the inertial flux terms (see Appendix A.1):

$$\left|\frac{\partial F}{\partial x} + \frac{\partial G}{\partial y}\right| \gg \left|gh\, S_f\right|.$$

The clipping introduced in Section 3.2.2 is therefore rarely triggered, and only for nearly dry cells where the mass transfer is negligible.

However, for the case of viscoplastic non-Newtonian flows, like mudflows, the friction slope S_f is significantly larger, as these flows are more viscous and more strongly dominated by friction than by inertia. In this regime (see Appendix A.2):

$$\left|\frac{\partial F}{\partial x} + \frac{\partial G}{\partial y}\right| \sim \left|gh\, S_f\right| \text{ or even } \left|\frac{\partial F}{\partial x} + \frac{\partial G}{\partial y}\right| \ll \left|gh\, S_f\right|$$

In this case, the source term can have a significant impact on the mass transfer, and the current splitting method and sequence of operation can lead to non-physical results such as *Artificial Mass Diffusion* because the clipping is nearly systematically triggered.

The *Artificial Mass Diffusion*, from cell A to cell B over a time step from t^n to t^{n+1} can be described as follows:

- **Step 1 — Flux computation:** the LHLLC solver at the A-B interface uses the values U_A^n and U_B^n to compute the fluxes F_j, without accounting for source term effects. After the flux update step, the intermediate values U_A^* and U_B^* are obtained, which may include a mass flux Δh^* from cell A to cell B.
- **Step 2 — Mass transfer:** the mass flux Δh^* is applied to the cells:

$$h_A^{n+1} = h_A^n - \frac{\Delta t}{\Omega_A}\,\Delta h^* \cdot L, \qquad h_B^{n+1} = h_B^n + \frac{\Delta t}{\Omega_B}\,\Delta h^* \cdot L$$

- **Step 3 — Friction application and clipping** are applied to the intermediate specific discharges q_x^* and q_y^*. Since friction is dominant in most cases, the specific discharges are reduced to negative values and subsequently clipped. However, the mass flux Δh already transferred mass from A to B is not returned to cell A.

The outcome is a transfer of mass from A to B with no remaining velocity to physically justify the transport:

$$\underbrace{\Delta h \neq 0}_{\text{mass transferred from A to B}} \qquad \text{yet} \qquad \underbrace{q_x^{n+1} = 0}_{\text{specific discharge zeroed by clipping}}$$

3.4 Proposed adaptations of the solver

To address the artificial mass diffusion issue identified in the previous section, the following modifications to the solver are proposed in this thesis. They are designed to better handle flows in which the source term dominates over the flux terms, as is typical in mudflow simulations.

It is important to note that the goal of these modifications is to adapt the solver to the specific case of mudflows. However, the current solver is not designed for such a case and the best approach would be to implement a new solver that directly takes into account the source term in the flux computation, rather than applying it as a correction after the flux update. Nevertheless, such a new implementation goes beyond the scope of this master's thesis, and the proposed modifications are a workaround to mitigate the issue within the current framework.

3.4.1 Temporary state variable and stopping criterion

To prevent mass transfer having no physical justification (i.e. without any specific discharge), a temporary state variable approach is introduced. Rather than applying all updates directly to the conservative variable U_i^n, all computations of a time step are first performed on a temporary copy U_i^{temp}, leaving U_i^n unchanged. A stopping criterion is then evaluated on U_i^{temp} before any update is implemented.

The stopping criterion compares the magnitude of the friction force to the magnitude of the available momentum. The clipping is triggered if:

$$\underbrace{\sqrt{\left(q_{x,friction}^{temp}\right)^2 + \left(q_{y,friction}^{temp}\right)^2}}_{\text{friction impulse}} \geq \underbrace{\sqrt{(q_x^{temp})^2 + (q_y^{temp})^2}}_{\text{available momentum}} \tag{3.7}$$

Where $q_{x,friction}^{temp}$ and $q_{y,friction}^{temp}$ are the specific discharges that would be subtracted from q_x^{temp} and q_y^{temp} if the friction were applied, and q_x^{temp} and q_y^{temp} are the specific discharges before applying friction.

This condition detects whether the friction force exceeds the total available momentum in the cell, regardless of direction. Two cases arise depending on whether the stopping criterion is triggered:

- **Criterion not triggered,** the flow is active. The real conservative variable is updated:

$$U_i^{n+1} = U_i^{\text{temp}}$$

  and the friction source term is applied normally.

- **Criterion triggered,** the flow should stop. The outgoing fluxes of the cell are zeroed in the flux buffers, as well as the incoming fluxes from this cell to its neighbours for mass conservation. The source term due to friction is computed again based on the adapted fluxes (i.e. with zero outgoing fluxes) and applied to the real conservative variable.

This approach ensures that mass is only transferred from a cell A to its neighbour B if there is sufficient momentum in cell A to justify the transfer, thus preventing any artificial mass diffusion.

3.4.2 Semi-implicit friction treatment

The proposed approach consists of treating the friction term semi-implicitly to avoid negative specific discharges. Indeed, as the clipping is now based on a vectorial criterion, it is possible that one of the specific discharges is negative while the other is still positive, which would lead to a non-physical state.

Currently, in the second step of the update, the source term is applied as a correction on the specific discharges, and it is computed based on the q^n values. With this method, the clipping mentioned above is necessary to avoid negative specific discharges:

$$q_x^{n+1} = q_x^* + \Delta t\ ghS_{0x} - \Delta t\ ghS_{fx}\,(U^n)$$

To avoid this issue, the friction source term is treated semi-implicitly. The friction slope S_f is linearised about the intermediate state U^* obtained after the flux update:

$$gh\ S_{fx}(U^{n+1}) \approx C_f(U^*)\ q_x^{n+1}$$

where C_f is a linearisation coefficient depending on the rheology and evaluated at U^*.

Starting from the definitions:

$$S_f = \frac{\tau_b}{\rho gh} \qquad \text{and} \qquad S_{fx} = S_f \frac{u}{|\mathbf{u}|} = S_f \frac{q_x}{h|\mathbf{u}|}$$

the friction contribution to the momentum equation reads:

$$\left.\frac{\partial q_x}{\partial t}\right|_{\text{friction}} = -gh\, S_{fx} = -gh\, S_f \frac{q_x}{h|\mathbf{u}|} = -\frac{\tau_b}{\rho h|\mathbf{u}|}\, q_x = -C_f\, q_x$$

The linearisation coefficient can thus be formulated as:

$$C_f = \frac{\tau_b}{\rho h|\mathbf{u}|}$$

The update of the specific discharge in the x direction can then be written as:

$$\begin{aligned} q_x^{n+1} &= q_x^* + \Delta t\; ghS_{0x} - \Delta t\; ghS_{fx}\left(U^{n+1}\right) \\ q_x^{n+1} &= q_x^* + \Delta t\; ghS_{0x} - \Delta t\; C_f(U^*)\; q_x^{n+1} \\ q_x^{n+1}\left(1 + \Delta t\; C_f(U^*)\right) &= q_x^* + \Delta t\; ghS_{0x} \end{aligned}$$

which finally yields the following update formula for the specific discharge in the x direction:

$$q_x^{n+1} = \frac{q_x^* + \Delta t\; ghS_{0x}}{1 + \Delta t\; C_f(U^*)} \tag{3.8}$$

and an analogous expression for the specific discharge in the y direction.

Since the denominator is strictly positive, the sign of q_x^{n+1} is entirely determined by the sign of $q_x^* + \Delta t\; ghS_{0x}$, which is the value of the specific discharge we would have without friction. Consequently, friction can only attenuate the magnitude of the specific discharge, but cannot reverse its direction or produce negative values, thereby eliminating the need for clipping. Indeed, the following cases can be distinguished:

- If the numerator is negative due to an adverse bed slope (S_{0x} strongly negative), then $q_x^{n+1} < 0$. This is physically correct, as the topography decelerates and reverses the flow.
- A sign reversal due to friction alone is structurally impossible, since the friction contribution is confined to the denominator.

The main limitation of this method is the linearisation of the friction slope, which is only an approximation of the real friction slope. This can lead to some errors in the computation of the specific discharges, especially for highly non-linear rheologies.

CHAPTER 4

Rheological models and their depth-averaged implementation

As explained in Section 3.1, the key difference between the modelling of water with the Shallow Water Equations (SWE) and of mudflows with the same set of equations lies in the constitutive law used to close the system, i.e. the rheological relationship linking shear stress to shear rate. Whereas water is typically modelled using empirical friction laws such as the Manning's law, mudflows require a rheological constitutive law.

4.1 Rheological models

"Rheology describes the deformation and flow behaviour of a system" (Whorton *et al.* (2025)). It is used to characterise the relationship between the shear stress τ (Pa) and the shear rate $\dot{\gamma}$ (s^{-1}) of a fluid. The three first rheological models described here under have the following characteristics[1]:

- Under a certain shear-stress threshold τ_y (yield stress), the fluid behaves like a solid and has a constant velocity along depth. This part is often referred to as the "plug zone".
- Above this threshold, the fluid flows and the relationship between τ and $\dot{\gamma}$ is model-dependent.
- If the stress at the bottom of the flow is below the yield stress, the flow does not move.
- The depth where the shear stress equals the yield stress defines the limit between the plug zone and the sheared zone. This depth is called the yield depth h_s.

[1] These concepts have been more widely discussed in Chapter 2 but they are recalled here for clarity.

4.1.1 Bingham model

The Bingham model is formulated as follows (Pastor *et al.* (2004)):

$$\tau = \tau_y + \mu\,\dot{\gamma} \qquad \text{if} \quad \tau > \tau_y, \tag{4.1}$$

and

$$\dot{\gamma} = 0 \qquad \text{if} \quad \tau \leq \tau_y,$$

where μ is the plastic viscosity (Pa.s).

The Bingham model assumes a linear relationship between the shear stress and shear rate, like the Newtonian model, but with a yield stress leading to a larger shear stress at the bottom of the flow compared to the Newtonian model (Gibson *et al.* (2021)). This difference can be seen in Figure 4.1 where the idealised rheological behaviour of a Bingham fluid is compared to a Newtonian fluid and to the other models presented in this section.

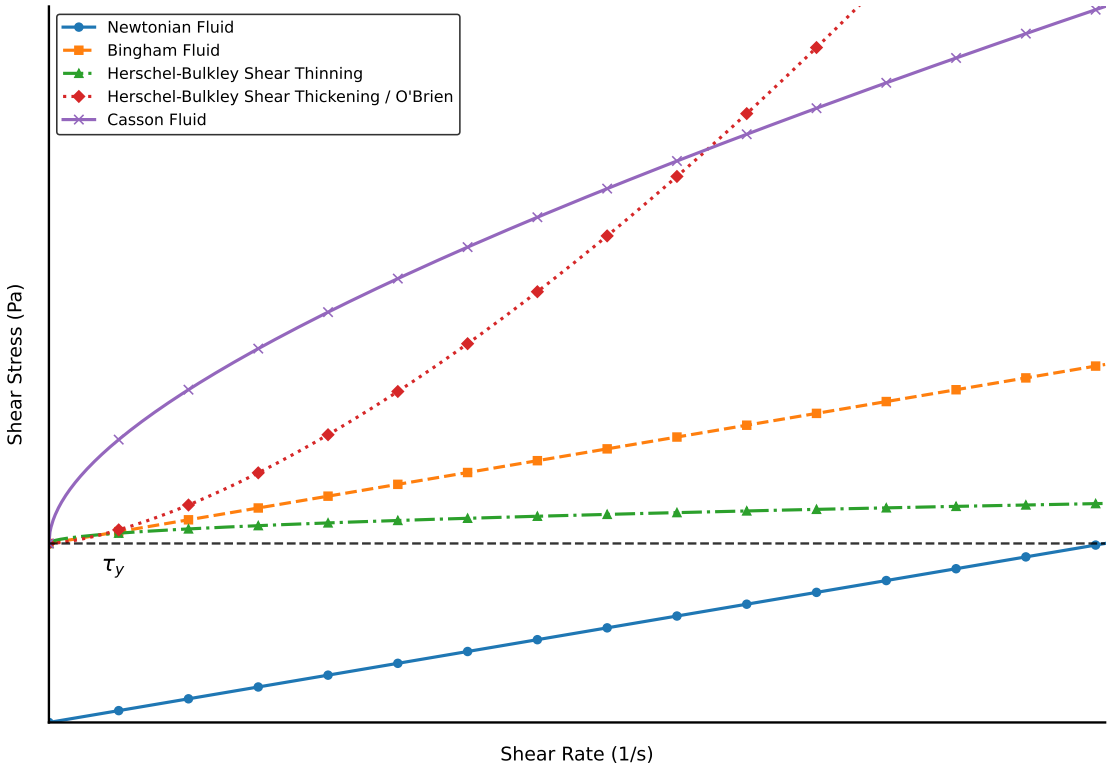


Fig 4.1. *Comparison of the idealised rheological behaviour of a Bingham fluid, of a Herschel-Bulkley fluid with $n = 0.5$ (shear-thinning) and $n = 1.5$ (shear-thickening), of a Casson fluid, and of a Newtonian fluid.*

This model is the most widely used (with the Herschel-Bulkley model) to describe the behaviour of mudflows, notably because of its simplicity and the fact that it captures the main characteristics of these flows (yield stress and viscous behaviour) at low strain rates. However, it does not account for the shear-thinning or shear-thickening behaviour of the fluid and non-linear effects on the shear stress. Therefore, it is only suitable for low concentration, low velocity

and homogeneous mudflows, where the viscous behaviour is dominant and the inter-particle interactions are negligible (Gibson *et al.* (2021), Huang and García (1998)).

4.1.2 Herschel-Bulkley model

The Herschel-Bulkley model (HB model) is a generalisation of the Bingham model and is formulated as follows (Whorton *et al.* (2025), Engineers (2023)):

$$\tau = \tau_y + K\,\dot{\gamma}^n \qquad \text{if} \quad \tau > \tau_y, \tag{4.2}$$

and

$$\dot{\gamma} = 0 \qquad \text{if} \quad \tau \leq \tau_y,$$

where K is the consistency (Pa.s^n) and n the flow behaviour index (dimensionless). The flow index n characterises the shear-thinning or shear-thickening behaviour of the fluid as illustrated in Figure 4.1 and defined as follows:

- If $n < 1$, the fluid is shear-thinning (pseudoplastic): the viscosity decreases with increasing shear rate.
- If $n = 1$, the fluid behaves like a Bingham fluid.
- If $n > 1$, the fluid is shear-thickening (dilatant): the viscosity increases with increasing shear rate.

"The Herschel-Bulkley approach is more empirical. By diverging from a linear model, the coefficient (K) in the non-linear term no longer has units of viscosity and cannot be directly measured" (Gibson *et al.* (2021)). Indeed, the parameters of the HB model are usually obtained by calibration based on experimental data.

As a generalisation of the Bingham model, the HB model is mostly used to describe the behaviour of more complex mudflows. Depending on the value of the flow index n, it can capture very different behaviours:

- For $n < 1$, it is the most common model for natural mudflows where the structure of the fluid is progressively broken which leads to a decreasing apparent viscosity with increasing shear rate. Values of n found in the literature are typically between 0.3 and 0.7 (Huang and García (1998)).
- For $n > 1$, it can be used to describe very dense mudflows where the inter-particle interactions are important and lead to an increasing apparent viscosity with increasing shear rate. However, this behaviour is not commonly observed in natural mudflows and is more relevant for debris flows. It can be seen as a first approximation of the quadratic model presented in the next section (Gibson *et al.* (2021), Huang and García (1998)).

The Herschel–Bulkley model is therefore positioned intermediate between viscosity dominated flows, such as the Bingham or Casson models, and more inertia-dominated approaches. While the model remains well suited to viscous and transitional mudflows, its limitations at high solid concentrations and high shear rates motivate the introduction of quadratic stress contributions, as considered in the O'Brien model presented in Section 4.1.4.

4.1.3 Casson model

The Casson model is formulated as follows (Whorton *et al.* (2025)):

$$\sqrt{\tau} = \sqrt{\tau_y} + \sqrt{\mu\,\dot{\gamma}} \qquad \text{if} \quad \tau > \tau_y, \tag{4.3}$$

and

$$\dot{\gamma} = 0 \qquad \text{if} \quad \tau \leq \tau_y,$$

where μ is the plastic viscosity of Casson (Pa.s).

Figure 4.1 shows that the Casson model provides a smooth transition between the solid/plug behaviour and the fluid/sheared behaviour, which is not the case for the Bingham and Herschel-Bulkley models. Then, at high shear rates, the Casson model converges towards a Bingham behaviour. This model is usually used to describe the behaviour of blood, polymers, and some food products, but it can also be interesting to describe the behaviour of mudflows where the transition between the solid and fluid behaviour is progressive and not abrupt like in the case of oil-based or water-based mudflows, where the viscous behaviour is dominant (Houwen and Geehan (1986)).

4.1.4 Quadratic model

The semi-empirical quadratic model, also called O'Brien model is widely used, notably in the HEC-RAS software (Engineers (2023)). The model, described in Dimas *et al.* (2023), Engineers (2023) and O'Brien and Julien (1988), is formulated as follows:

$$\tau_b = \tau_y + \mu_m\dot{\gamma} + \rho_m l_m^2\dot{\gamma}^2 + 0.01\rho_s\left(\left(\frac{0.615}{C_V}\right)^{\frac{1}{3}} - 1\right)^{-2} d_s^2\dot{\gamma}^2 \tag{4.4}$$

where μ_m is the plastic viscosity (Pa.s), ρ_m is the density of the mud (kg/m^3), l_m is the characteristic length of the mud (m) (i.e "Prandtl mixing length"), ρ_s is the density of the solid particles (kg/m^3), C_V is the volumetric concentration of solids in the mud and d_s is the diameter of the solid particles (m). The factor 0.01 is an empirical coefficient obtained by calibration (O'Brien and Julien (1988)). It is also important to note that the value of the maximum volumetric concentration of solids C_V is set to 0.615 in the original model, but it can be adapted to fit the characteristics of the flow considered.

This model adds two quadratic terms to the Bingham model to take into account inter-particle interactions and turbulence effects (Gibson *et al.* (2021)). By including these terms, this model assumes that the flows are dilatant.

As explained in O'Brien, Julien, and Fullerton (1993), this model takes into account inertial and turbulent effects which was not the case for previous models. Moreover, as it does not allow for the existence of a plug zone, it is more suitable for debris flows or mudflows at very high concentration and/or velocity where the inertial and turbulent effects are more important than the viscous effects. It provides also an implicit transition towards a granular flow behaviour when the concentration of solids increases, which is not the case with previous models.

4.1.5 Comparison of the different rheological models

Figure 4.1 compares the idealised rheological behaviours captured by the different models presented in this chapter.

Figure 4.2 shows the evolution of the apparent viscosity as a function of the shear rate for the different models. The apparent viscosity is defined as $\eta = \tau/\dot{\gamma}$, and it characterises the resistance of the fluid to flow. The difference between the Newtonian model where the apparent viscosity is constant (which is the definition of a Newtonian fluid) and the other models where the apparent viscosity varies with the shear rate is clearly visible. Models with a yield stress show an infinite apparent viscosity at zero shear rate, which is a consequence of the fact that the fluid behaves like a solid and does not flow below the yield stress. Then, they all show a decreasing apparent viscosity with increasing shear rate and an asymptotic behaviour towards the plastic viscosity at high shear rate, except for the Herschel-Bulkley model with $n > 1$ where the apparent viscosity finally increases with increasing shear rate.

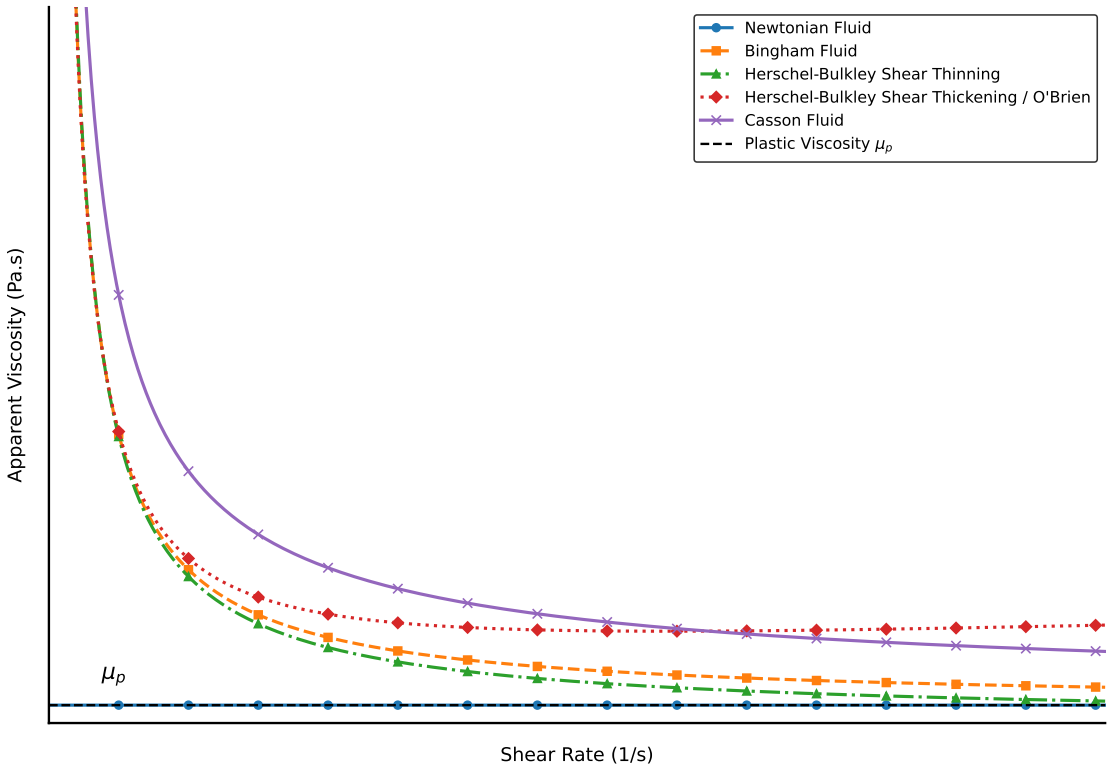


Fig 4.2. *Comparison of the apparent viscosity as a function of the shear rate for the considered rheological models.*

Table 4.1 shows which rheological models can be used to simulate different flow types and processes. The shear components which need to be added to take a specific process into account according to O'Brien, Julien, and Fullerton (1993) and Herschel-Bulkley are also indicated. This classification is inspired by Gibson *et al.* (2021) and is not exhaustive. It is important to note that the thresholds between the different types of flows are indicative and might vary according to the considered study.

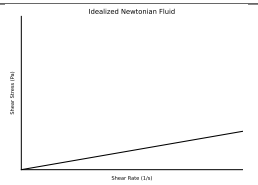
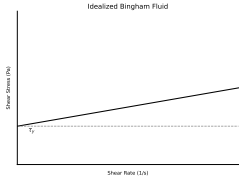
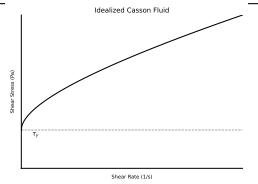
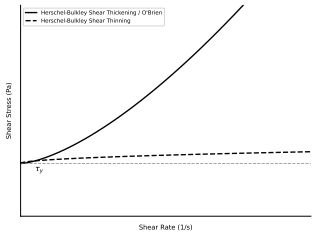
Flow classification	Process	Threshold	Associated shear component according to O'Brien, Julien, and Fullerton (1993)	Associated shear component according to Herschel-Bulkley	Rheological / Geotechnical model
Sediment transport	Bedload and suspended load	$C_v < 5\%$	None	None	
Hyper-concentrated flow	Yield stress and viscous losses	$C_v > 5\%$	Bingham	$\tau = \tau_y + K\dot{\gamma}$	
	Yield stress with smooth transition		Casson	$\tau = \left(\sqrt{\tau_y} + \sqrt{K\dot{\gamma}}\right)^2$	
Mudflow	Inter-particle turbulence	–	$\rho_m l_m^2 \dot{\gamma}^2$	$\tau = K\dot{\gamma}^{\,n} \quad (n \neq 1)$	
Debris flow	Grain collision	$N_{\text{BAG}} > 40$	$0.01\,\rho_s \left[\left(\frac{0.615}{C_v}\right)^{1/3} - 1\right]^{-2} d_s^2 \dot{\gamma}^2$		

Table 4.1. *Conceptual classification of sediment-laden flows and associated rheological models, inspired by Gibson* et al. *(2021).*

4.2 Watlab implementation

As explained in Section 3.1 about the numerical resolution of the Shallow Water Equations in Watlab, the code needs a friction slope S_f to compute the source term of the momentum equation. This friction slope is computed as follows:

$$S_f = \frac{\tau_b}{\rho g h} \tag{4.5}$$

To be implemented in the Watlab code, the different models need to be re-formulated to express the shear stress at the bottom of the flow (τ_b) as a function of conservative variable on Shallow Water Equations: the flow depth-averaged velocity ($\bar{u}$) and the flow depth (h).

4.2.1 Computation of the shear stress at the bottom of the flow

The re-formulation is done like described in Pastor *et al.* (2004) and in the Master's thesis Liesse (2026), and is illustrated in Figure 4.3:

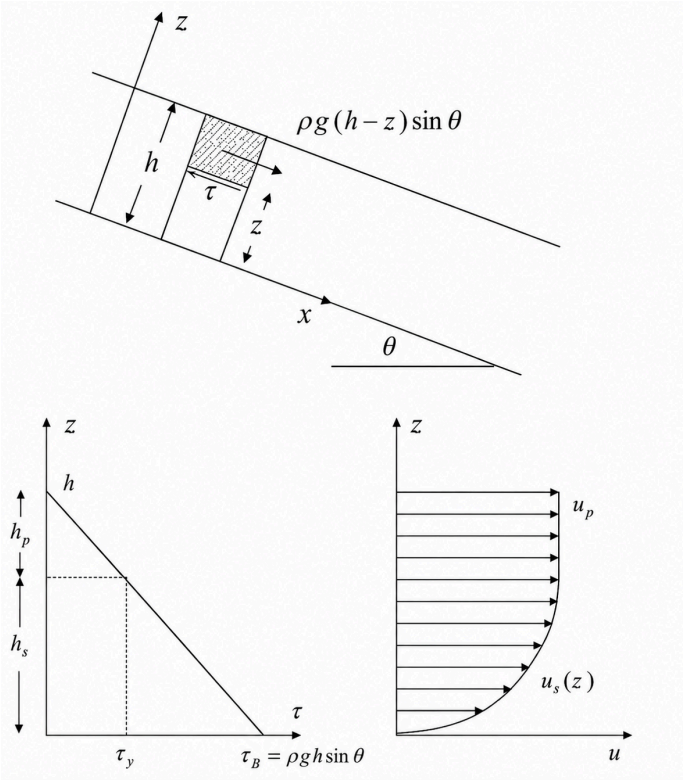


Fig 4.3. *Shear stress distribution and velocity profile for a "threshold fluid" in steady uniform flow over an inclined plane (Pastor* et al. *(2004), Liesse (2026)).*

In the Shallow Water Equations, the shear stress can be assumed to be linear along depth which gives the following relationship:

$$\tau(z) = \tau_b \left(1 - \frac{z}{h}\right) \tag{4.6}$$

The procedure to derive $\bar{u}(\tau_b)$ for the three viscoplastic models follows the same steps:

1. **Inversion of the constitutive law.** The local relation $\tau = \tau(\dot{\gamma})$ given by the rheological model is inverted to express the shear rate as a function of the local shear stress, $\dot{\gamma} = f(\tau)$. For the three viscoplastic models, f is identically zero whenever $\tau \leq \tau_y$, since the fluid does not flow under the yield stress.

2. **Identification of the plug zone.** The linear stress profile (4.6) crosses the yield value $\tau = \tau_y$ at the depth $z = h_s = h(1 - \xi)$, with $\xi = \tau_y/\tau_b$. For $z \in [0,\ h_s]$, the fluid is sheared and $\dot{\gamma} > 0$. For $z \in [h_s,\ h]$, the fluid is in plug regime, with constant velocity along the depth.

3. **Integration of the shear rate.** The velocity profile $u(z) = \int_0^z \dot{\gamma}(\tau(z'))\,\mathrm{d}z'$ is obtained by integrating $f(\tau(z'))$ over the sheared zone, and remains constant equal to $u(h_s)$ throughout the plug zone.

4. **Depth-averaging.** The depth-averaged velocity $\bar{u} = (1/h)\int_0^h u(z)\,\mathrm{d}z$ is obtained by integrating the velocity profile, splitting the integral between sheared and plug zones.

5. **Reformulation in terms of ξ.** A change of variable using the dimensionless yield stress $\xi = \tau_y/\tau_b$ produces a compact algebraic form of $\bar{u}(\tau_b)$ specific to each model.

The complete computation is done in Appendix B for the Casson model and is carried out following the same pattern in Pastor *et al.* (2004) and Liesse (2026) for the Bingham and Herschel-Bulkley models.

It is important to note that the procedure described above relies on several assumptions that are not always verified in natural flows, which may introduce important errors in the computation of τ_b and therefore in the simulation of the flow:

- The shear stress is assumed to be linear along depth, which is correct for a steady uniform flow over an inclined plane but only approximate elsewhere.
- The velocity profile is assumed to be the one of a fully developed flow at every point of the simulation, which implicitly assumes a steady-state local equilibrium between the driving force and the friction.
- The same integrated relation is then used to define τ_b at every point of an unsteady, non-uniform flow.

The resulting expressions for the three viscoplastic models are summarised in the following subsections. The quadratic model, however, uses a different approach detailed at the end of this section.

Bingham

The expression of the shear stress at the bottom of the flow as a function of depth-averaged velocity and flow depth is given by (Pastor *et al.* (2004), Liesse (2026)):

$$\bar{u} = \frac{\tau_b h}{6\mu} \left(1 - \xi\right)^2 \left(2 + \xi\right), \tag{4.7}$$

where $\xi = \frac{\tau_y}{\tau_b}$ is the dimensionless yield stress.

For this model, Pastor *et al.* (2004) propose an analytic approximation by interpolating the Equation 4.7 with a Tchebychev polynomial of degree 2 to reduce computational cost.

Herschel-Bulkley

The expression of the shear stress at the bottom of the flow as a function of depth-averaged velocity and flow depth is given by Liesse (2026):

$$\bar{u} = \frac{h}{n+1} \left(\frac{\tau_y}{K}\right)^{\frac{1}{n}} \frac{\left(1 - \xi\right)^{\frac{n+1}{n}}}{\xi^{\frac{1}{n}}} \left(1 - \frac{n}{2n+1} + \frac{n\xi}{2n+1}\right) \tag{4.8}$$

Casson

The expression of the shear stress at the bottom of the flow as a function of depth-averaged velocity and flow depth is derived in Appendix B and is given by:

$$\bar{u} = \frac{\tau_b h}{\mu} \left(\frac{1}{3} + \frac{\xi}{2} - \frac{4\sqrt{\xi}}{5} - \frac{\xi^3}{30}\right) \tag{4.9}$$

Quadratic model

Here, to express the shear stress at the bottom (τ_b) as a function of depth-averaged velocity ($\bar{u}$) and flow depth (h), a different approach is used compared to the previous models. Instead of assuming a linear distribution of shearstress along depth, an *a priori* velocity profile is assumed. Usually, a parabolic velocity profile is assumed, which is coherent with the profile seen in Figure 4.3 for a “threshold fluid”. However, this approach does not allow for the existence of a plug zone.

Applying the parabolic velocity profile allows expressing the shear rate as a function of the depth-averaged velocity and flow depth, which gives the following expression of the shear stress at the bottom of the flow as a function of $\bar{u}$ and h (Dimas *et al.* (2023)):

$$\tau_b = \tau_y + \mu_m \frac{3\bar{u}}{h} + \left[\rho_m l_m^2 + 0.01\rho_s \left(\left(\frac{0.615}{C_V}\right)^{\frac{1}{3}} - 1\right)^{-2} d_s^2\right] \left(\frac{3\bar{u}}{h}\right)^2 \tag{4.10}$$

By this method, the numerical resolution of the equation is straightforward, which is an advantage of this model. However, the assumption of a parabolic velocity profile and the absence of a plug zone may introduce important errors which makes the calibration of the model parameters particularly important.

4.2.2 Regularisation of the constitutive laws

All the closures presented above share the same problem at implementation time: the yield stress τ_y creates a discontinuity between the rest state and the flowing state. For the three viscoplastic models (4.7), (4.8) and (4.9), this difficulty is structural: the formulae are derived for $\tau_b > \tau_y$, while the rest state is described by the separate condition $\bar{u} = 0$. The depth-averaged constitutive law is therefore defined piecewise:

$$\bar{u}(\tau_b) \;=\; \begin{cases} \text{model formula} & \text{if } \tau_b > \tau_y, \\ 0 & \text{if } \tau_b \leq \tau_y, \end{cases} \tag{4.11}$$

with a discontinuous derivative at $\tau_b = \tau_y$.

In order to avoid numerical instabilities and convergence issues, the constitutive laws are regularised by smoothing the transition between the rest state and the flowing state, as proposed in Papanastasiou (1987).

Physical justification

The discontinuity at the transition between the rest state and the flowing state is not exactly physical. It is an idealisation of the behaviour of such fluids. As explained and illustrated in Barnes and Walters (1985), precise low-shear rate measurements of rheological properties of polymers following a Bingham behaviour reveal a transition between the rest state and the flowing state that is not abrupt but smooth. Barnes and Walters (1985) even questioned the existence of a true yield stress in such fluids, arguing that on sufficiently long timescales, the fluid will eventually flow and that the yield stress is more an artefact from the limitations of the measurement techniques than a real physical property.

However, in the case of mudflows, this idealisation of the behaviour of the fluid does not invalidate the use of such rheological models. Indeed, the timescales of the flow are usually much shorter than the timescales required for the fluid to flow under the yield stress, which makes the idealisation of a discontinuous transition between rest and flow states relevant. Moreover, the engineering quantities of interest, runout distance, flow velocity and depth, deposit geometry, *etc.* are well captured by an idealised rheological model with a yield stress. In this instance, the constitutive regularised laws are intended to facilitate not only a numerical resolution but also to provide a more realistic transition between the rest and flowing states.

Numerical justification

For the three implicit viscoplastic models, the computation of τ_b from the simulation state at each time step and each cell requires the inversion of $\bar{u}(\tau_b)$. A Newton-Raphson method is used for this numerical inversion, which uses the local derivative of the function to converge towards the root. This method requires the function to be at least continuously differentiable over the entire search interval, a condition that the piecewise law (4.11) fails to satisfy at $\tau_b = \tau_y$, where the derivative jumps from a finite positive value to zero. Without regularisation, a Newton–Raphson iteration crossing the yield point would either diverge, oscillate, or converge to a spurious value depending on the side from which the iterate approaches.

Papanastasiou's original substitution

This idea was originally introduced by Papanastasiou (1987) for the Bingham model. The regularisation proposed is based on the local constitutive law described in Section 4.1.1. Papanastasiou (1987) replaces the constant yield-stress contribution τ_y by a sigmoid regularised version that vanishes with the shear rate:

$$\tau \;=\; \left(1 - e^{-m|\dot{\gamma}|}\right)\tau_y \;+\; \mu\,\dot{\gamma}, \tag{4.12}$$

where m is a sharpness parameter. The bracketed factor tends to 1 for $|\dot{\gamma}| \gg 1/m$, recovering the original Bingham law, and to 0 for $|\dot{\gamma}| \ll 1/m$, removing the discontinuity at $\dot{\gamma} = 0$. The substitution defines a single smooth law $\tau(\dot{\gamma})$ valid for all $\dot{\gamma}$, and applies identically to yielded and unyielded regions of the flow.

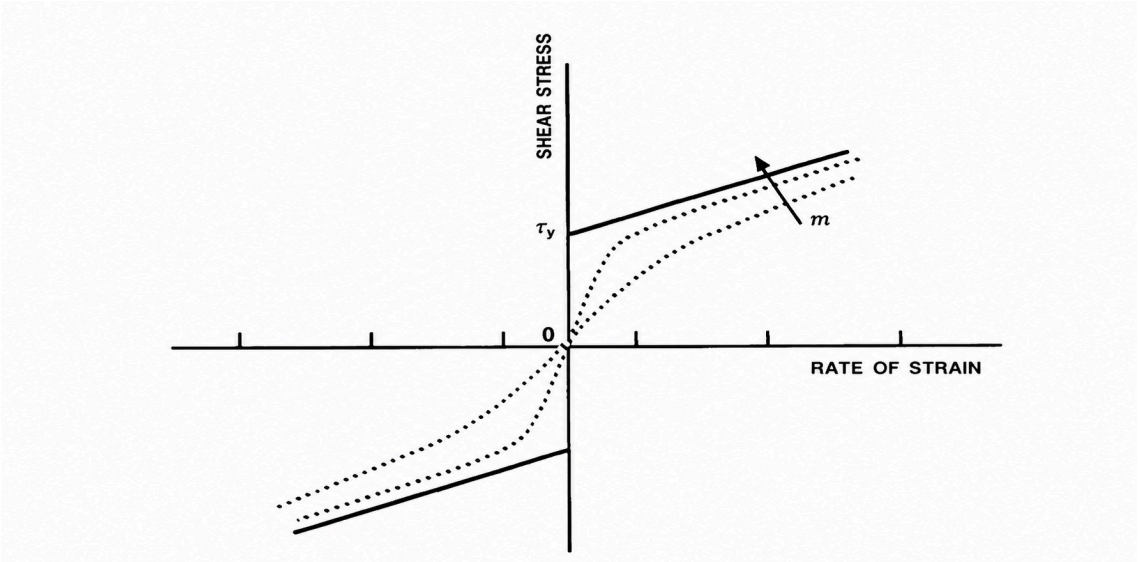


Fig 4.4. *Stress as a function of rate of strain at several values of m for regularised local law, from Papanastasiou (1987).*

The approach in this work is inspired by the idea of Papanastasiou (1987) for the four constituent laws presented above, with one key adaptation. Papanastasiou's substitution operates at the local scale: the smooth ramp $1-e^{-m|\dot{\gamma}|}$ is applied directly to the constitutive relation $\tau(\dot{\gamma})$, where m has units of time and controls the smoothing in shear-rate space. Integrating this regularised local law in depth would, in principle, produce a regularised depth-averaged relation $\bar{u}(\tau_b)$, but the integration is not analytically tractable for the three viscoplastic models, and would require a numerical integration at each time step and each cell of the simulation, which would be computationally expensive.

Instead, the regularisation is applied directly to the depth-averaged constitutive law $\bar{u}(\tau_b)$, The smoothing parameter is denoted M throughout this work to avoid confusion with Papanastasiou's m. It is thus evident that the two regularisation approaches are not equivalent, yet they are both driven by the objective of achieving a smooth transition between the rest state and the flowing state. Furthermore, both approaches introduce a smoothing parameter that necessitates calibration. Both will be illustrated side by side in Figures 4.6 to 4.9 for each of the three implicit models, the local form being shown for reference and the depth-averaged form being the one actually used in the simulations.

For the quadratic model, the situation is slightly different and somewhat closer to the original Papanastasiou approach: the closure (4.10) is already explicit at the depth-averaged level, so the regularisation is applied directly to the additive yield term in $\bar{u}$ space, with the same sigmoid form as Papanastasiou but with $\bar{u}$ in place of $\dot{\gamma}$. This case is detailed at the end of the section.

Softplus regularisation of the depth-averaged laws

The piecewise definition (4.11) can be rewritten in an equivalent and more compact form as follows for the three viscoplastic models:

$$\bar{u}(\tau_b) = \left(\max(0,\, 1-\xi)\right)^k \cdot (\dots),$$

where $(\dots)$ represent the rest of the equation and $k > 0$ is an exponent depending on the original model. The discontinuity of the piecewise law is fully captured by the $\max()$ function. Regularising the constitutive law thus reduces to approximating this $\max()$ by a smooth function. The natural choice is the *softplus* function:

$$\mathcal{S}(x, M) = \frac{1}{M}\,\ln\left(1+e^{Mx}\right), \qquad \mathcal{S}(x, M) \xrightarrow[M\to\infty]{} \max(0,\, x), \tag{4.13}$$

with $M > 0$ a sharpness parameter controlling the width $\mathcal{O}(1/M)$ of the transition zone. The softplus is strictly positive, infinitely differentiable on $\mathbb{R}$, and tends pointwise to the ramp function as $M \to \infty$. Its derivative is the sigmoid function $\sigma(x; M) = 1/(1+e^{-Mx})$, which provides an analytical expression for $\partial\bar{u}_{reg}/\partial\tau_b$ usable by the Newton–Raphson solver.

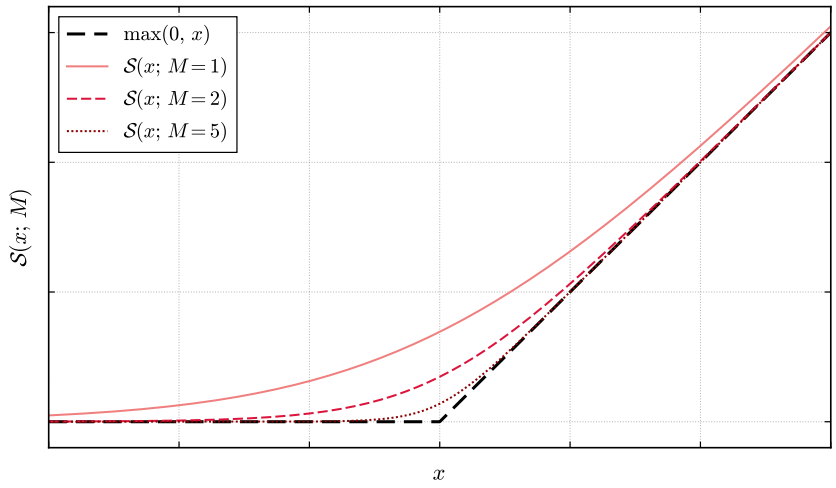


Fig 4.5. *Softplus function $\mathcal{S}(x;M)$ for several values of the sharpness parameter M, compared to its limiting case $\max(0,x)$. As M increases, $\mathcal{S}$ converges pointwise to the ramp function while remaining C^∞ everywhere.*

The regularised closures are obtained by substituting $\mathcal{S}(1-\xi;M)$ for $\max(0,\,1-\xi)$ in the formulae. For the Bingham and Herschel–Bulkley models, the substitution acts directly on the $(1-\xi)^k$ factor. For the Casson model, where ξ also appears alone elsewhere in the formula, a regularised dimensionless yield stress $\xi_{\text{reg}} = 1-\mathcal{S}(1-\xi;M)$ is defined and substituted globally for ξ throughout the closure, ensuring consistent behaviour across the full range of τ_b.

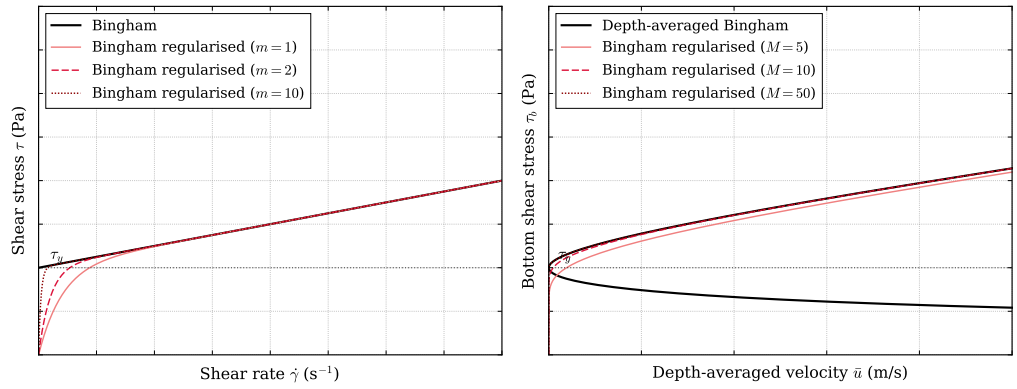


Fig 4.6. *Effect of the regularisation on the Bingham model. Left: local constitutive law $\tau(\dot\gamma)$ with the Papanastasiou substitution* (4.12) *for several values of the local sharpness parameter m. Right: depth-averaged law $\bar u(\tau_b)$ with the softplus substitution for several values of the dimensionless sharpness parameter M, used in the Watlab implementation.*

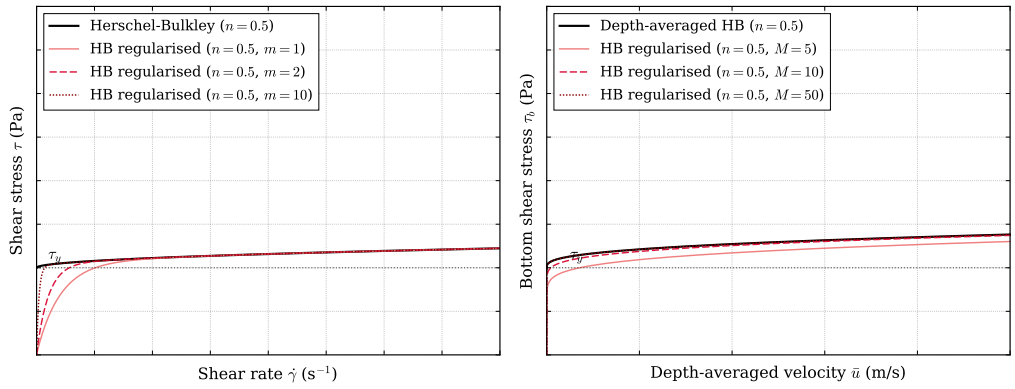


Fig 4.7. *Effect of the regularisation on the Herschel–Bulkley model in the shear-thinning regime ($n = 0.5$, typical of natural mudflows). Left: local constitutive law with Papanastasiou substitution. Right: depth-averaged law with softplus substitution.*

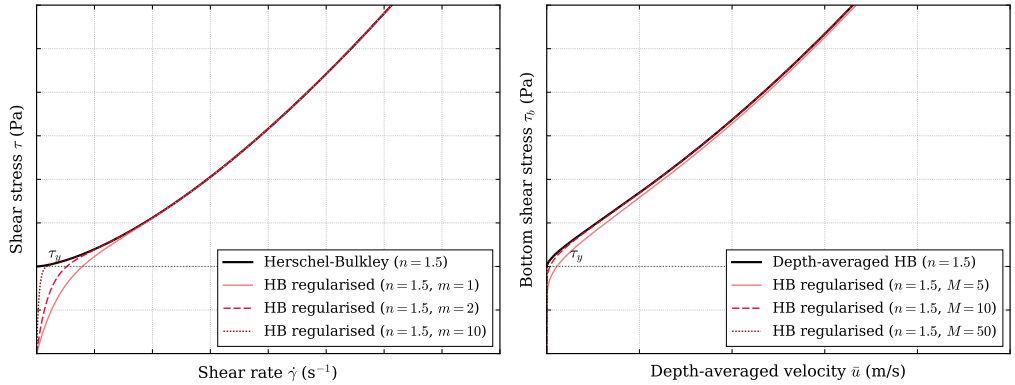


Fig 4.8. *Effect of the regularisation on the Herschel–Bulkley model in the shear-thickening regime ($n = 1.5$). Left: local constitutive law with Papanastasiou substitution. Right: depth-averaged law with softplus substitution.*

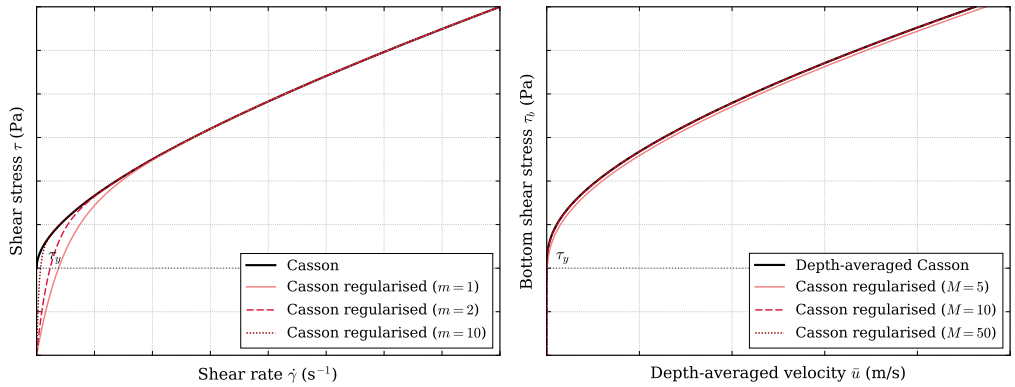


Fig 4.9. *Effect of the regularisation on the Casson model. Left: local constitutive law with Papanastasiou substitution. Right: depth-averaged law with softplus substitution applied through $\xi_{reg} = 1 - \mathcal{S}(1 - \xi; M)$.*

Direct regularisation of the quadratic model

For the quadratic model, since the closure is already explicit in $\bar{u}$, the regularisation is applied directly to the yield-stress term in (4.10), in the spirit of the original Papanastasiou substitution (4.12): the constant term τ_y is replaced by the smooth ramp $\tau_y\,(1-e^{-M\bar{u}})$, with M playing the role of the sharpness parameter at the depth-averaged level:

$$\tau_b^{\text{reg}}(\bar{u},h) \;=\; \tau_y\left(1-e^{-M\bar{u}}\right)+\mu_m\,\frac{3\bar{u}}{h}+\left[\rho_m l_m^2+0.01\,\rho_s\left(\dots\right)\right]\left(\frac{3\bar{u}}{h}\right)^2. \tag{4.14}$$

This substitution removes the finite jump at $\bar{u}=0$ in a way consistent with the softplus treatment of the implicit models.

Numerical inversion and choice of M

Once regularised, the three implicit closures are smooth, monotonically increasing functions of τ_b that admit a unique solution to $\bar{u}_{reg}(\tau_b)$ at each cell and each time step. This inversion is performed numerically with a hybrid Newton–Raphson / bisection scheme that combines the fast convergence of Newton–Raphson in the smooth regions with the robustness of bisection near the yield point. The value of τ_b is then converted into the friction slope $S_f=\tau_b/(\rho g h)$. The quadratic model, being explicit, requires no inversion.

The sharpness parameter M controls a trade-off between fidelity to the idealised constitutive law and numerical robustness. Large M produces a sharp yield-stress representation but a steep transition that can slow down the Newton–Raphson iteration, small M smooths the transition over a wide range and artificially lowers the apparent yield stress, which leads to excess spreading and an underestimation of the deposit thickness. The benchmark of Chapter 5 illustrates the differences and convergence of solutions depending on M.

CHAPTER 5

Validation and sensitivity analysis

In order to validate the implementation of the modified solver and regularised rheology, the implementation was assessed against experimental data to ascertain the model's capacity to reproduce the observed flow behaviour and its limitations. The benchmark case was selected on the basis of three requirements: an independently characterised rheology, a flow regime that involves both the inertial and the yield-stress-dominated dynamics, and the availability of comparable numerical studies for cross-validation.

5.1 Experimental setup

The viscoplastic dam-break experiments of Ancey *et al.* (2012) satisfy all three criteria and are therefore retained as the reference test case for this section. The inclined dam-break configuration is particularly challenging for depth-averaged viscoplastic solvers: the sudden gate release produces a strongly transient flow that transitions from an inertia-dominated phase to a yield-stress-controlled arrest, thereby probing the full Herschel–Bulkley regime within a single experiment. Alternative canonical tests such as steady uniform flow on an inclined plane or horizontal axisymmetric spreading isolate only one of these regimes and are consequently less representative. Moreover, the dataset of Ancey *et al.* (2012) has been adopted as a reference in several recent depth-averaged studies, notably Fernández-Nieto *et al.* (2023) and Muchiri *et al.* (2025), which enables a direct comparison of the present implementation with state-of-the-art numerical models.

In these experiments, a constant volume of Carbopol ultrez 10, a synthetic polymeric gel that exhibits characteristics of a Herschel–Bulkley fluid, was released onto an inclined flume and permitted to flow freely downslope. The geometry, displayed in Figure 5.1, consists of a rectangular channel of width $w = 0.10$ m, an initial volume of 6 L is contained behind a removable gate located at $x = 0.5$ m and instantaneously released at $t = 0$. The channel is inclined at an angle $\theta = 15^\circ$ to the horizontal, and the flow is driven by gravity.

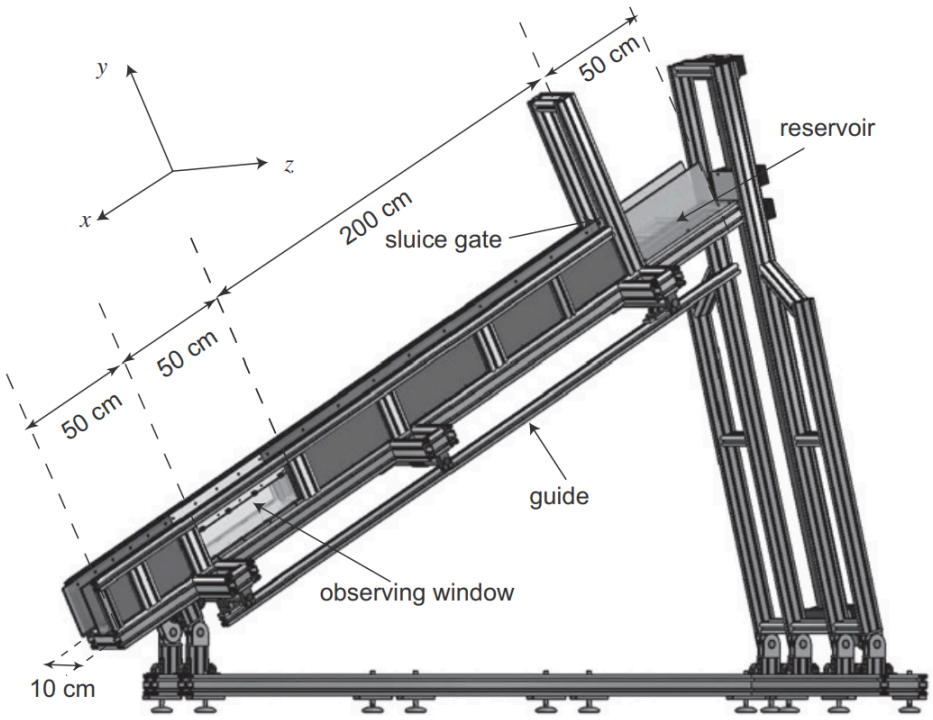


Fig 5.1. *Schematic of the experimental setup for the viscoplastic dam-break experiments, from Ancey* et al. *(2012).*

The rheological parameters of the Carbopol gel were independently characterised "using a parallel plate geometry (with serrated plates, diameter 60 mm and gap 2 mm) mounted on a Bohlin CVOR rheometer" (Ancey *et al.* (2012)), and are summarised in Table 5.1.

Table 5.1. *Herschel–Bulkley rheological parameters of the Carbopol ultrez 10 gel used in the experiments of Ancey* et al. *(2012).*

Parameter	Symbol	Value	Maximum deviation
Yield stress	τ_y	33 Pa	± 2 Pa
Consistency index	K	26 Pa s^n	± 4 Pa s^n
Power-law index	n	0.33	± 0.02
Mass density	ρ	1000 kg m^{-3}	

It is important to note that Carbopol is not a naturally occurring mud. It is a transparent, water-swollen gel chosen specifically because it is optically accessible for PIV and because its Herschel–Bulkley rheology is exceptionally well characterised and reproducible. While numerous natural mudflows comply with a Herschel–Bulkley constitutive law, at least to a first approximation, the mapping from laboratory gel parameters to field-scale mud parameters introduces additional uncertainties that are not addressed in this section. The present benchmark thus validates the numerical scheme and the constitutive formulation, as opposed to the specific rheological parameters of any field material.

5.2 Numerical setup

The two-dimensional shallow-water equations with a Herschel–Bulkley source term are solved on an unstructured triangular mesh covering the domain $[0,\ L_{\mathrm{dom}}] \times [0,\ w]$ with no-flux (wall) boundary conditions on all sides except the downstream end, which is transmissive.

The initial condition and the characteristics tracked to assess the model's performance are widely inspired by the use of the exact same experimental data in Fernández-Nieto *et al.* (2023). The CFL number is set to $\mathrm{CFL} = 0.4$[1] throughout all simulations. Two series of mesh-refinement and parameter-sensitivity studies are conducted:

- **Mesh convergence** (fixed $M = 50$): three characteristic cell sizes $l_c \in \{0.03,\ 0.01,\ 0.005\}$ m are compared.
- **Regularisation sensitivity** (fixed $l_c = 0.01$ m): four sharpness values $M \in \{1,\ 5,\ 20,\ 50\}$ are compared.

5.3 Results and discussion

The results are organised around four quantities of interest: the front position $x_f(t)$, the front velocity $u_f(t)$, the flow depth at the gate $h(x{=}0,\, t)$, and the depth profile along the flume axis $h(x,\, t)$ at selected time steps. For each quantity, the sensitivity to the mesh characteristic size l_c and to the regularisation parameter M are examined separately. In the case of dam-break experiments, the flow evolution can be qualitatively divided into two distinct phases (Fernández-Nieto *et al.* (2023)): an initial "*inertial phase*" following the gate release, during which inertia governs the dynamics and the front accelerates to a peak velocity before decelerating, and a subsequent "*spreading phase*" during which inertia has been dissipated and the flow creeps slowly towards its final deposit under the balance between gravity and yield stress. In this particular experiment, the inertial phase lasts approximately 1 second, while the spreading phase extends from 1 second to the end of the experiment.

5.3.1 Front position and front velocity

Sensitivity to the mesh characteristic size l_c

Figures 5.2 and 5.3 show the front position $x_f(t)$ and front velocity $u_f(t)$ for the three mesh sizes, alongside the experimental data of Ancey *et al.* (2012). Assuming the most refined mesh ($l_c = 0.005$ m) as the reference solution, a convergence trend is clearly observed as the mesh is refined.

[1] Although the scheme remains stable up to $\mathrm{CFL} \approx 0.9$, the smaller value of 0.4 was retained throughout: it was first adopted as a safe choice to avoid any stability concerns, and subsequently kept unchanged to ensure consistency across all reported simulations.

The model systematically overestimates the front position, predicting that the mass spreads faster than observed experimentally. Initially, approximately 0.7 seconds into the flow, the front position and velocity are accurately captured. Subsequently, as the experimental flow decelerates and attains a quasi-constant velocity, the model is driven by its own inertia and significantly overestimates the front velocity and position. Finally, during the spreading phase, the model is capable of capturing the front velocity. However, the front position is still overestimated due to the overestimation during the inertial phase.

This tendency is well documented in the literature: Ancey *et al.* (2012) themselves report the same overestimation when applying the Saint-Venant equations to this test case, and note that even the kinematic-wave model achieves better agreement despite being formally less sophisticated. The exact same overestimation is also observed for the same type of model in Fernández-Nieto *et al.* (2023) (i.e. Figure 5.10). However, the results in this study are closer to the experimental data than those obtained there, which may be attributed to differences in the numerical implementation and the assumptions made to compute the basal shear stress τ_b (see Section 5.4.1).

Even if this overestimation is a common feature of depth-averaged models for this test case, it is important to note that the model does capture the two distinct phases of the flow, and that the front velocity during the spreading phase is well captured. Furthermore, a very efficient correction leading to a much better agreement with the experimental data is proposed in Muchiri *et al.* (2025), i.e. Figure 5.10 for comparison, and is explained in Section 5.4.2.

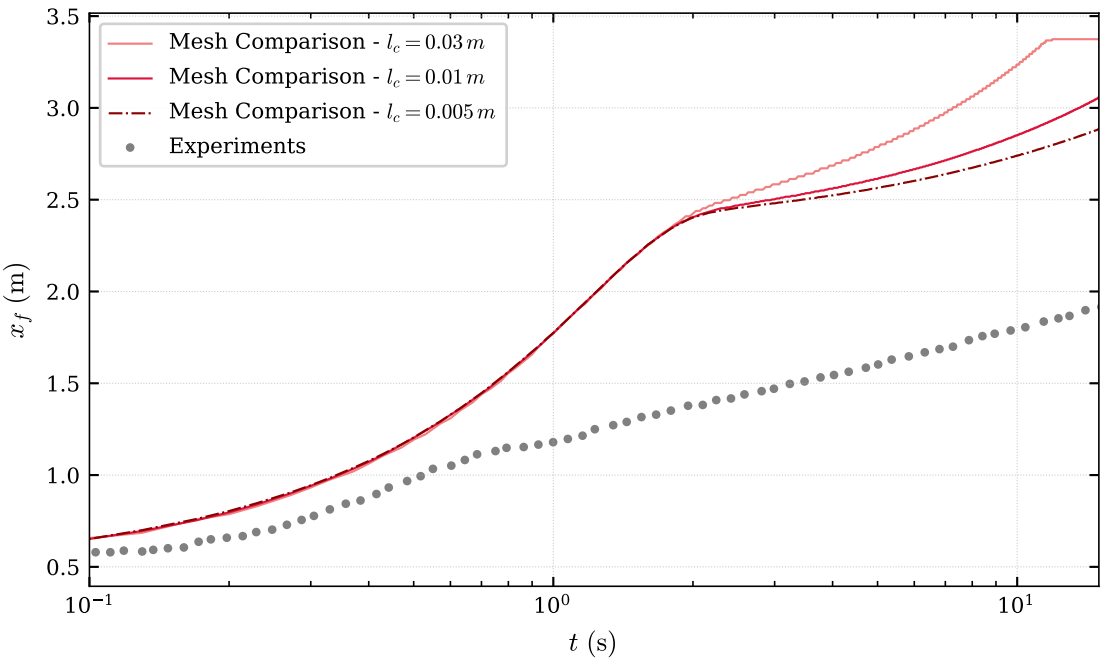


Fig 5.2. *Front position $x_f(t)$ as a function of time for three mesh sizes ($M = 50$, $\mathrm{CFL} = 0.4$) with regularised rheology, compared with the experimental data of Ancey* et al. *(2012).*

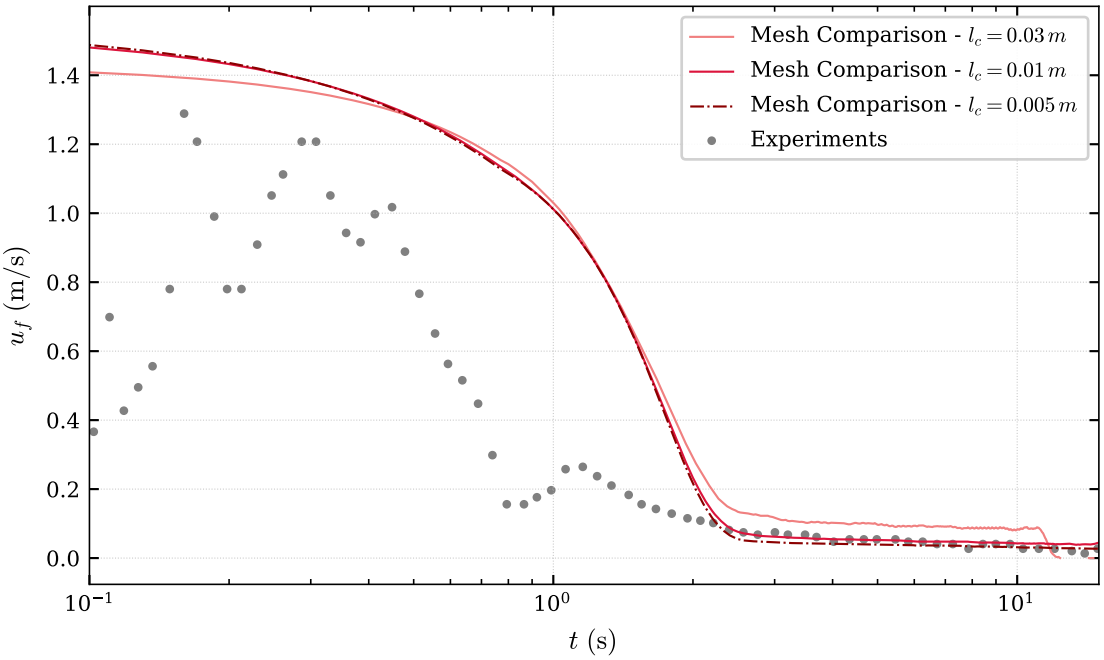


Fig 5.3. *Front velocity $u_f(t)$ as a function of time for three mesh sizes ($M = 50$, $\mathrm{CFL} = 0.4$) with regularised rheology, compared with experiments.*

Sensitivity to the regularisation parameter M

Figures 5.4 and 5.5 show the effect of the regularisation sharpness M on the front position and velocity. For $M = 1$, the regularisation is very smooth, effectively reducing the apparent yield stress over a wide range of strain rates and resulting in a significantly faster front. For $M \geq 20$, the solutions are virtually indistinguishable, demonstrating convergence of the regularised model towards a well-defined limit.

The value $M = 50$ is therefore retained as the default in all subsequent simulations, as it combines sharp yield-stress representation with robust numerical behaviour.

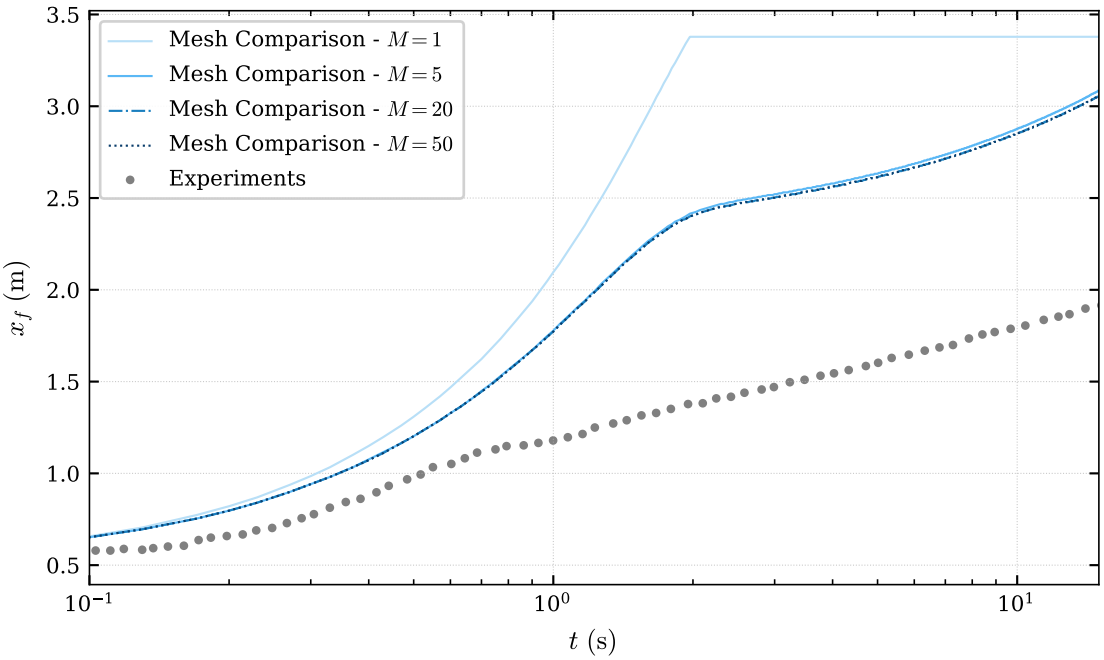


Fig 5.4. *Front position $x_f(t)$ for four values of the regularisation parameter M ($l_c = 0.01$ m, CFL $= 0.4$) with regularised rheology, compared with experiments.*

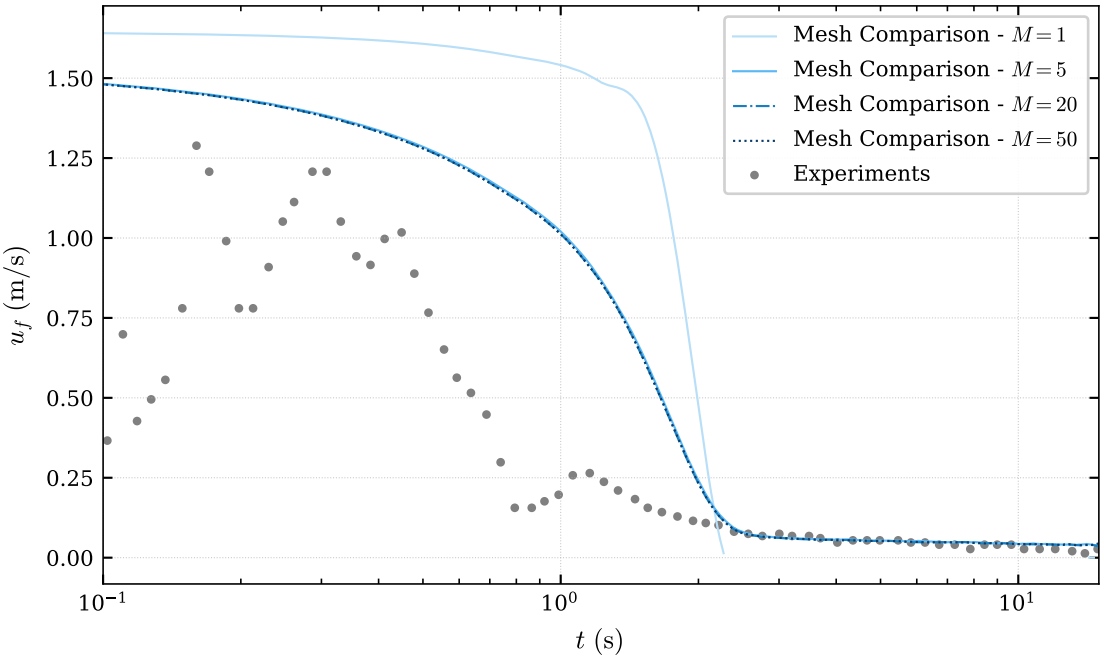


Fig 5.5. *Front velocity $u_f(t)$ for four values of M ($l_c = 0.01$ m, CFL $= 0.4$) with regularised rheology, compared with experiments.*

5.3.2 Depth at the gate

Sensitivity to the mesh characteristic size l_c

Figure 5.6 shows the temporal evolution of the flow depth $h(x{=}0,\,t)$ at the gate location for the three mesh resolutions. All resolutions exhibit the same qualitative behaviour: a rapid decrease from the initial depth following gate release, followed by a gradual approach to a finite resting height. The final deposit height converges below the theoretical plug-flow arrest height $h_p = \tau_y/(\rho g \sin\theta) \approx 0.0102$ m. This under-prediction is consistent with the results of Fernández-Nieto *et al.* (2023) and the apparent convergence of the final height with mesh refinement suggests that it is not a numerical artefact but rather an inherent limitation, probably of the vectorial stopping criterion implemented in the solver.

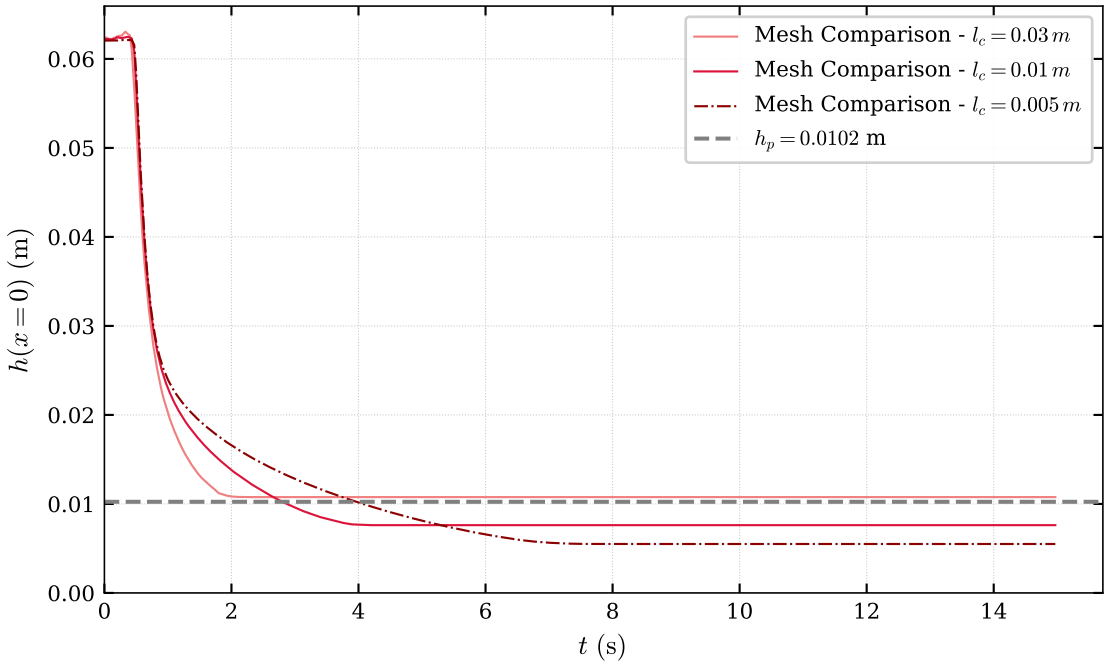


Fig 5.6. *Flow depth $h(x{=}0,\,t)$ at the gate location for three mesh sizes ($M = 50$, $\mathrm{CFL} = 0.4$) with regularised rheology. The dashed line indicates the theoretical plug-flow arrest height $h_p = 0.0102$ m.*

Sensitivity to the regularisation parameter M

Figure 5.7 shows the same quantity for varying M. The effect of M on the final deposit depth is moderate: all values $M \geq 5$ produce a final height within a narrow band just below h_p, while $M = 1$ leads to a slightly lower arrest height, reflecting the more diffuse yield-stress transition and the associated excess spreading. The convergence of the curves for $M \geq 5$ confirms that the regularisation does not artificially alter the arrest dynamics when the sharpness parameter is sufficiently large.

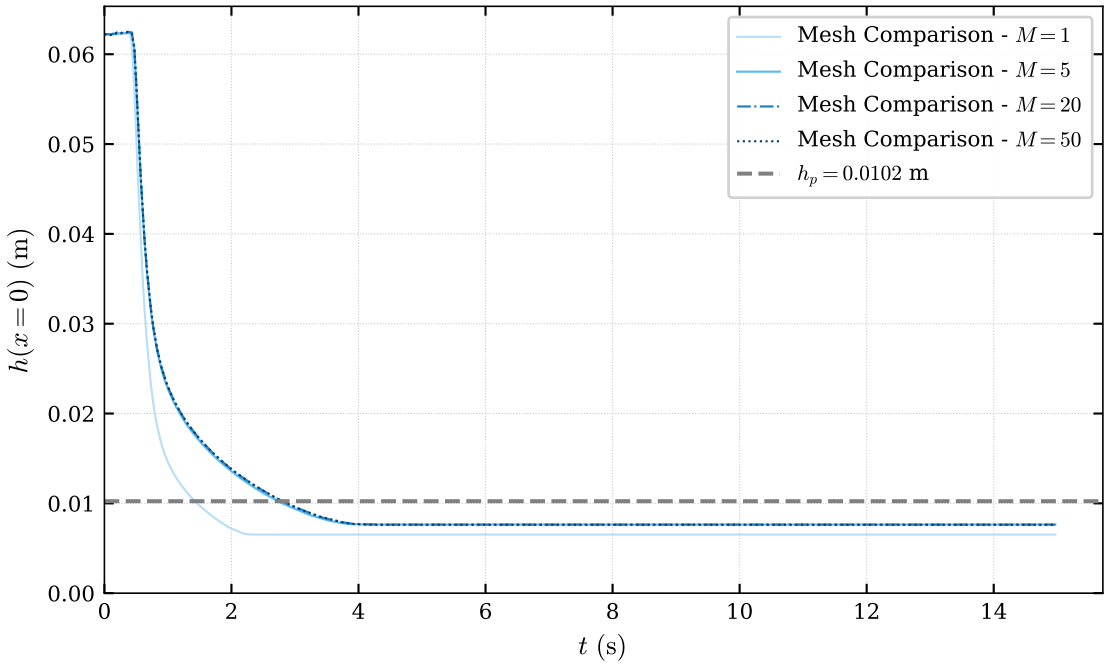


Fig 5.7. *Flow depth $h(x{=}0, t)$ for four values of M ($l_c = 0.01$ m, $\mathrm{CFL} = 0.4$) with regularised rheology. The dashed line indicates $h_p = 0.0102$ m.*

5.3.3 Depth profile

Sensitivity to the mesh characteristic size l_c

Figure 5.8 shows the free-surface profiles along the flume axis at $t \in \{0.5,\ 1.0,\ 2.0,\ 5.0,\ 10.0\}$ s for the three mesh resolutions. The overall shape of the spreading mass is well reproduced: a relatively flat body region behind a steeper head that progressively loses height as the front advances. The profiles for $l_c = 0.01$ m and $l_c = 0.005$ m are essentially indistinguishable, confirming mesh convergence. The convergence to a constant final deposit profile has also been observed, thus confirming the convergence of the final gate height. This figure demonstrates the principal effect of mesh refinement, which is to reduce the velocity of the front more rapidly. Consequently, this results in the primary differences in front position being observed at late times. As illustrated in Figures 5.2 and 5.3, the three curves are observed to be in proximity at the inertial phase of the flow, subsequently diverging at the spreading phase at later times.

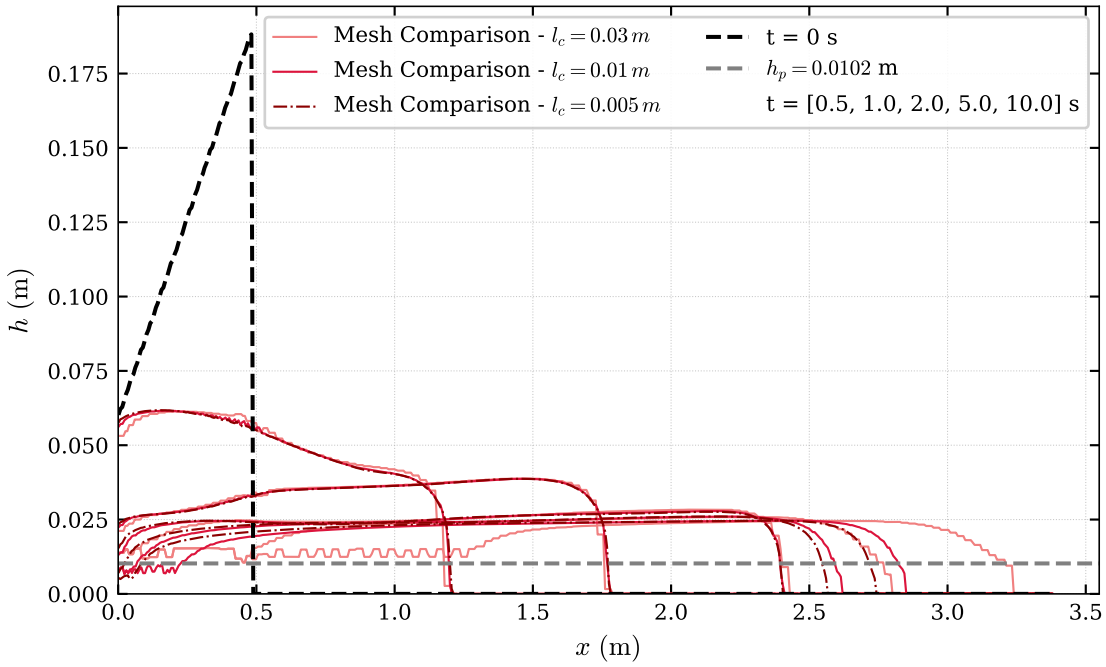


Fig 5.8. *Free-surface profiles along the flume axis at $t \in \{0.5,\ 1.0,\ 2.0,\ 5.0,\ 10.0\}$ s for three mesh sizes ($M = 50$, $\mathrm{CFL} = 0.4$) with regularised rheology.*

Sensitivity to the regularisation parameter M

Figure 5.9 shows the depth profiles for varying M. The profiles for $M \geq 20$ are nearly superimposed at all times, while $M = 1$ produces a noticeably thinner and more extended mass, consistent with the excess spreading already observed in the front position curves. For $M = 5$, the profile lies between these two regimes even if a net tendency towards the $M \geq 20$ profiles is observed. This figure also confirms that the regularisation does not significantly change the behaviour of the flow in the inertial phase, while it has a more pronounced effect during the spreading phase at later times, where the flow is more sensitive to the precise representation of the yield-stress transition.

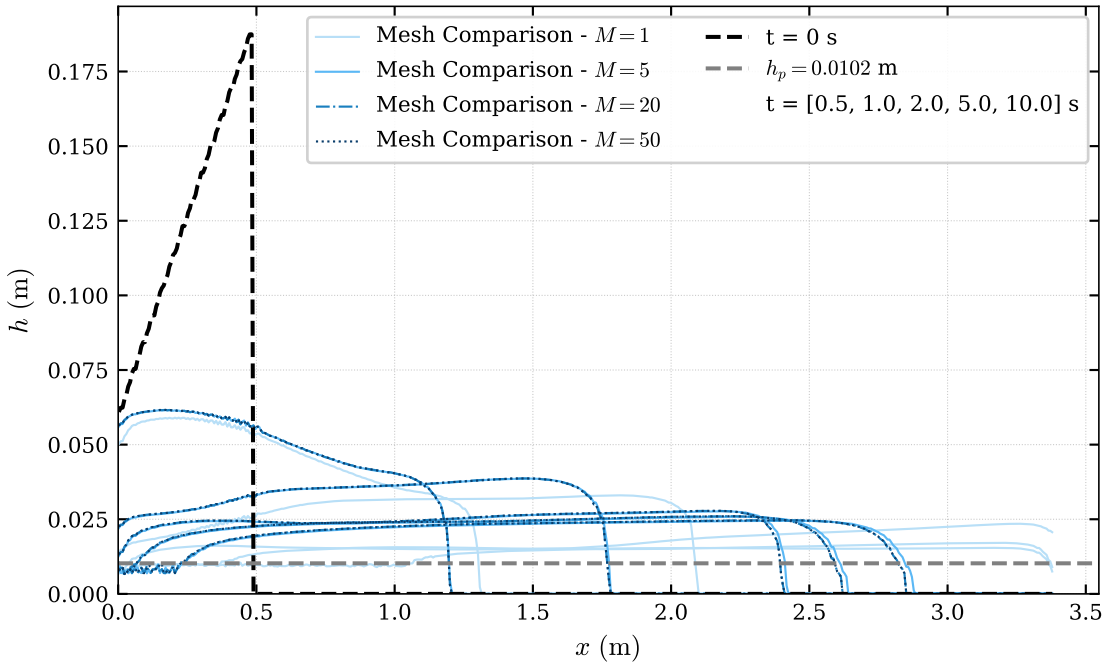


Fig 5.9. *Free-surface profiles along the flume axis at $t \in \{0.5,\ 1.0,\ 2.0,\ 5.0,\ 10.0\}$ s for four values of M ($l_c = 0.01$ m, $\mathrm{CFL} = 0.4$) with regularised rheology.*

5.3.4 Temporal computation cost

Table 5.2 reports the wall-clock computation time for 15 seconds of simulated flow time at CFL = 0.4. All simulations were run in parallel using OpenMP on a Lenovo Yoga laptop equipped with an AMD Ryzen 7 7735HS processor (8 cores, 16 threads).

Effect of mesh size

The computation time increases sharply with mesh refinement, rising from 16 s for $l_c = 0.03$ m to 2051 s for $l_c = 0.005$ m. This behaviour is expected for explicit finite-volume schemes. The exponential increase in computation time with mesh refinement highlights the importance of achieving mesh convergence at the coarsest possible resolution, and motivates the use of adaptive mesh refinement in future work to concentrate computational resources near the front and other regions of interest.

Effect of regularisation parameter M.

The computation time is largely insensitive to M for $M \geq 5$, with values clustered between 233 s and 241 s. The only notable exception is $M = 1$, which completes in 88 s, approximately three times faster than the converged cases. This speed-up is explained by the smoother constitutive law at low M: the Newton–Raphson inversion of the Herschel–Bulkley relation converges in fewer iterations when the function $\bar{u}(\tau_b)$ is more gently curved near the yield point. However, as demonstrated in Section 5.3.1, this faster convergence comes at the cost of a physically inaccurate

yield-stress representation. For $M \geq 20$, both the solution and the computation time are fully converged, confirming that the sharpness of the regularisation does not introduce additional computational overhead once the Newton–Raphson solver operates in the well-conditioned regime.

Table 5.2. *Computation time for the benchmark simulations for different mesh sizes and regularisation parameters (CFL = 0.4, 15 seconds of simulated time, AMD Ryzen 7 7735HS, 16 threads).*

Mesh size l_c (m)	Regularisation parameter M	Computation time (s)
0.03	50	16
0.01	50	233
0.005	50	2051
0.01	1	88
0.01	5	241
0.01	20	241
0.01	50	233

5.4 Limitations and comparison with the literature

The results presented above demonstrate that the implementation correctly reproduces the qualitative behaviour of a viscoplastic dam-break flow and is consistent with comparable depth-averaged models reported in the literature Ancey *et al.* (2012) and Fernández-Nieto *et al.* (2023). Several limitations nonetheless deserve to be noted.

5.4.1 Rheological model

As previously stated, the results obtained are in accordance with the existing literature, given the utilisation of equivalent assumptions and solvers. However, the results obtained with the same type of model in Fernández-Nieto *et al.* (2023) and Muchiri *et al.* (2025) are closer to the experimental data than those obtained here. An explanation for this discrepancy may be found in the assumptions made to compute the basal shear stress τ_b in the depth-averaged model.

In the present implementation, τ_b is computed by numerically inverting the depth-averaged relation $\bar{u}(\tau_b)$ using a hybrid Newton-Raphson/bisection method. The main assumption behind the derivation of the relation $\bar{u}(\tau_b)$ is that the flow is fully developed in a vertical Poiseuille/HB profile as explained in Section 4.2. Indeed, in the development from the local constitutive law $\tau = \tau(\dot{\gamma})$ to the depth-averaged relation $\bar{u} = \bar{u}(\tau_b)$, the flow is assumed to be steady and fully developed, which allows deriving an analytical expression for $\bar{u}(\tau_b)$ in the case of a Herschel–Bulkley rheology. However, this assumption may not hold in most of the flow domain. In the future case of natural mudflow simulation, this assumption is even more likely to be violated, as the flow is expected to be highly unsteady and non-uniform. This could lead to an underestimation of the basal shear stress τ_b and consequently an overestimation of the front

velocity and position, as observed in the results.

In contrast, the implementation in Fernández-Nieto *et al.* (2023) relies on a derivation of the Coussot's closure:

$$\tau_b = \tau_y + K_b \left(\frac{\bar{u}}{h}\right)^n$$

where $K_b = 1.93K$ is an empirically calibrated consistency index. This is a semi-empirical relation calibrated on the bottom condition of a fully developed flow. The influence of the term K_b has been tested in Fernández-Nieto *et al.* (2023) and the results illustrate an important difference in the front position during the spreading phase, validating the hypothesis that the choice of the closure relation for τ_b is a key factor in the overestimation of the front position and velocity during this phase.

On the other hand, the implementation in Muchiri *et al.* (2025) expresses τ_b through an explicit closed-form relation that takes both the local discharge $\vec{q}$ *and* the local driving-slope vector $\vec{S_\theta}$ as inputs:

$$\tau_b = K \left(\frac{K}{\rho g \|\vec{S_\theta}\|}\right)^{m-1} \left(\frac{\tau_y}{\rho g \|\vec{S_\theta}\|} + h_c\right) \frac{q}{D\,(h)}$$

where $m = \frac{1}{n}$, $h_c = \max\big(0,\ h - h_p\big)$, $h_p = \tau_y/(\rho g \|\vec{S_\theta}\|)$, and $D(h) = h_c^{m+1}\Big(\frac{h_p}{m+1} + \frac{h_c}{m+2}\Big) + C\,h^{m+1}$, with C the basal slip coefficient.

This closure shares the same starting point as the present implementation: it relies on the same linear shear-stress profile (4.6) and the same fully-developed Herschel-Bulkley velocity profile. The two formulations only differ in which variable is treated as primary. The present implementation takes the depth-averaged velocity $\bar{u}$ and flow depth h as input and recovers τ_b by inverting $\bar{u}(\tau_b)$, which implicitly reconstructs the local driving slope from the velocity. The closure of Muchiri *et al.* (2025) takes the geometric driving slope $\vec{S_\theta}$ directly as input and produces τ_b explicitly. In a steady uniform flow the two approaches are exactly equivalent, but in an unsteady flow such as the inertial phase of the dam-break, the velocity and the geometric slope are no longer linked by the steady relation, and the explicit slope-based closure provides a friction that is more consistent with the actual local force balance. This development is detailed in Chapter 6 and explains partially the better results obtained in Muchiri *et al.* (2025) compared to the present implementation and to Fernández-Nieto *et al.* (2023), as illustrated in Figure 5.10.

5.4.2 Model correction

Beyond the choice of closure for τ_b discussed above, Muchiri *et al.* (2025) introduces an additional structural correction to the depth-averaged momentum equation. The standard Saint-Venant momentum balance, on which the present implementation is based, reads

$$\frac{\partial}{\partial t} q_x + \frac{\partial}{\partial x}\left(\frac{q_x^2}{h} + \frac{1}{2} g h^2 \cos\theta\right) + \frac{\partial}{\partial y}\left(\frac{q_x q_y}{h}\right) \;=\; g h \left(S_{0x} - S_{fx}\right)$$

with the analogous equation for the y-component. The momentum flux q_x^2/h originates from approximating the depth-integrated convective term $\int_b^H u^2 \, \mathrm{d}z$ by $\bar{u}^2 h$, which is exact only if the velocity is uniform over the depth. It is important to note that, in contrast with the current SWE implemented, the hydrostatic pressure term includes the slope angle θ in Muchiri *et al.* (2025), which is a more accurate representation of the pressure distribution in an inclined flow (in Watlab, as in most applications, the slope angle is small and the approximation $\cos\theta \approx 1$ is commonly used).

The asymptotic derivation of Muchiri *et al.* (2025) retains the leading-order correction to this approximation by computing $\int_b^H u^2 \, \mathrm{d}z$ directly from the Herschel–Bulkley vertical profile of the steady reference flow. The result is an additive correction to the momentum flux that depends only on the rheology and the local driving slope:

$$\int_b^H u^2 \, \mathrm{d}z \;\simeq\; \frac{q_x^2}{h} \;+\; \frac{\Lambda_x^{2m}\, h^{2m+3}}{(2m+3)(m+2)^2}$$

with the equivalent expression in y and a cross term proportional to $\Lambda_x^m \Lambda_y^m \, h^{2m+3}$, where $\vec{\Lambda} = (\rho g/K)\, \vec{S_\theta}$ and $m = 1/n$. This additive term enters the conservative momentum flux of the model. The corrected momentum equation in the x-direction reads

$$\frac{\partial}{\partial t} q_x + \frac{\partial}{\partial x}\left(\frac{q_x^2}{h} + C_m \Lambda_x^{2m} h^{2m+3} + \frac{1}{2} g h^2 \cos\theta \right) + \frac{\partial}{\partial y}\left(\frac{q_x\, q_y}{h} + C_m \Lambda_x^m \Lambda_y^m h^{2m+3} \right) \;=\; \dots$$

with $C_m = 1/[(2m+3)(m+2)^2]$, and similarly in the y-direction.

Physically, this correction encodes the fact that, for a fluid in which the velocity is concentrated near the free surface (which is the case for shear-thinning Herschel–Bulkley fluids with a plug zone), the kinetic energy flux $\int u^2$ is larger than what $\bar{u}^2 h$ predicts.

This additive correction is not implemented in the present work: it would require modifying the LHLLC flux reconstruction itself and the associated CFL condition, which is outside the scope of this work. The present implementation focuses on the closure of τ_b alone, which already recovers most of the improvement reported in Muchiri *et al.* (2025) as will be shown in Chapter 6. The additive momentum correction is mentioned here for completeness and is left as a natural perspective for future work.

5.4.3 Comparison with the literature

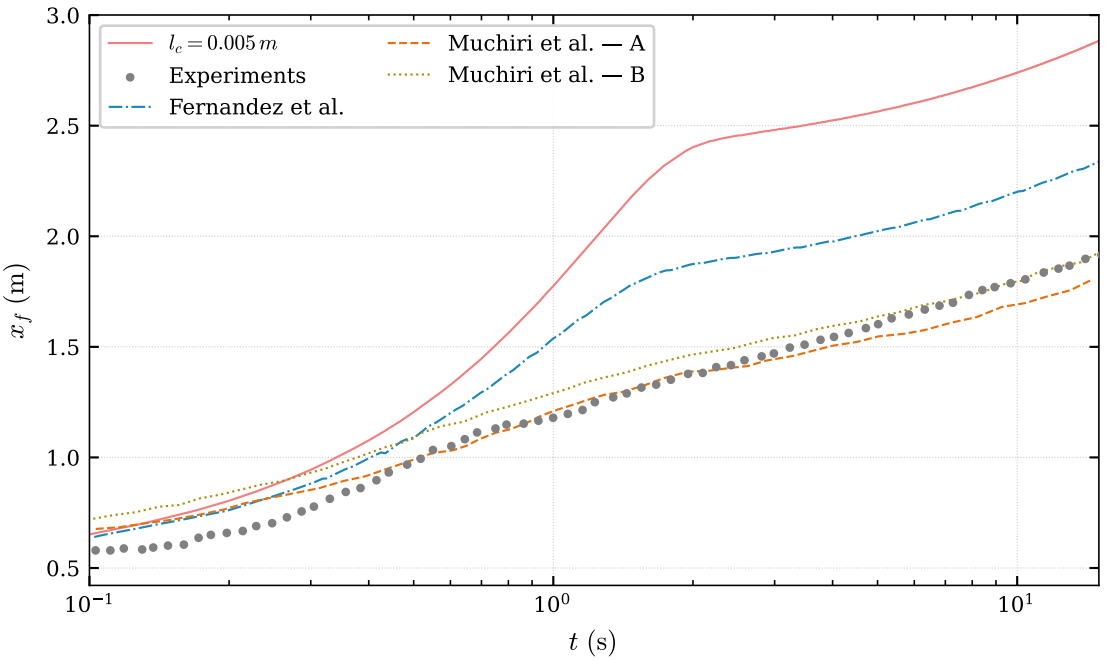


Fig 5.10. *Comparison of the front position $x_f(t)$ obtained in this study with the regularised rheology and the results from Fernández-Nieto* et al. *(2023) and Muchiri* et al. *(2025), alongside the experimental data.*

The Figure 5.10 illustrates the significant improvement in the front position prediction achieved by the modifications proposed in Muchiri *et al.* (2025), which closely align with the experimental data throughout the entire flow evolution, including both the inertial and spreading phases. The identical behaviour between the results obtained in this study and those of Fernández-Nieto *et al.* (2023) is also clearly visible, although the results obtained in Fernández-Nieto *et al.* (2023) are closer to the experimental data than those obtained here, particularly during the spreading phase.

CHAPTER 6

Improved closure: a slope-based formulation

6.1 Motivation and rheology derivation

The benchmark of Chapter 5 demonstrated that the regularised Herschel-Bulkley implementation, although consistent with comparable depth-averaged models reported in the literature, systematically overestimates the front position during the inertial phase of the dam-break. The analysis of Section 5.4 attributed this discrepancy primarily to the closure adopted for the basal shear stress: τ_b is obtained by numerically inverting the relation $\bar{u}(\tau_b)$. An approach which, by construction, links the local stress field to the steady reference flow that would produce the observed mean velocity. This is not strictly consistent with the actual local force balance during the inertial phase. During this phase, the flow is unsteady, and the velocity is no longer linked to the geometric slope through the steady relation implicitly assumed by the inversion.

The closure derived in Muchiri *et al.* (2025), based on the multi-regime asymptotic framework of Boutounet *et al.* (2016), relies on the same underlying assumptions but adopts a different parametrisation. Rather than treating the local averaged velocity as the input variable, the closure expresses τ_b directly as a function of the local flow state $(h,\ \vec{q})$ and of the local driving-slope vector $\vec{S_\theta}$. The key difference is that the slope vector $\vec{S_\theta}$ enters the closure as an explicit parameter, and is not implicitly reconstructed from the velocity by assuming a steady flow.

The full derivation is presented in Muchiri *et al.* (2025) and Boutounet *et al.* (2016), and is therefore not reproduced here. However, the precise step at which the two closures diverge is presented. Both derivations begin from the same depth-wise momentum balance at zeroth order [1] in the asymptotic expansion:

$$\frac{\partial \tau}{\partial z} \;=\; -\rho g \vec{S_\theta} \qquad \tau(z) \;=\; \rho g \vec{S_\theta}(h-z) \tag{6.1}$$

where the right-hand side is obtained by integration with the free-surface condition $\tau(z=h)=0$.

[1] The expression *zeroth order* refers to the leading-order terms of an asymptotic expansion in the parameters $\beta = \epsilon \mathrm{Re}$, $\alpha = \epsilon\gamma$ and $\delta = \epsilon/\gamma$ introduced in Boutounet *et al.* (2016), with $\epsilon = H^*/L^* << 1$ (it is the classical SWE assumption). Concretely, only the terms that survive in the thin-layer, stationary, uniform limit are retained. Inertial, unsteady and dynamic-pressure corrections are higher-order and discarded.

Evaluated at the bottom, this yields the relation:

$$\tau_b \;=\; \rho g\, h\, \vec{S_\theta} \tag{6.2}$$

It is interesting to note that the relation (4.6) can be exactly recovered by inserting Equation 6.2 in Equation 6.1.

The zeroth-order degeneracy

Equation 6.2 is, on its own, an incomplete closure for the depth-averaged momentum equation. The basal stress it predicts depends on h and $\|\vec{S_\theta}\|$ only, with no coupling to the local discharge $\vec{q}$. At fixed depth and slope, two flows with different velocities would receive the same friction, which is physically meaningless, since dissipation depends on flow velocity. Boutounet *et al.* (2016) and Muchiri *et al.* (2025) explicitly note this degeneracy of the zeroth-order expression and show that an additional substitution is required to recover a closure suitable for non-uniform flows.

The substitution adopted in Boutounet *et al.* (2016) and Muchiri *et al.* (2025) relies on the steady-state discharge relation derived from the Herschel-Bulkley rheology, which, in dimensional form, links the local discharge to the slope through:

$$q_x \;=\; \frac{\rho g\, S_{\theta_x}}{K}\left(\frac{\rho g\,\|\vec{S_\theta}\|}{K}\right)^{m-1} D(h)$$

where $D(h)$ collects the depth-dependent geometric factors of the sheared and plug zones (see Section 5.4.1) and $m = 1/n$. Isolating the slope in this expression and re-injecting it into $\tau_{bx} = \rho g h S_{\theta x}$ yields the closed-form basal stress:

$$\tau_{bx} \;=\; K\left(\frac{K}{\rho g\,\|\vec{S_\theta}\|}\right)^{m-1}\frac{h\,q_x}{D(h)} = K\left(\frac{K}{\rho g\|\vec{S_\theta}\|}\right)^{m-1}\left(\frac{\tau_y}{\rho g\|\vec{S_\theta}\|}+h_c\right)\frac{q_x}{D\,(h)} \tag{6.3}$$

where $h_c = \max\!\big(0,\; h - h_p\big)$, $h_p = \tau_y/(\rho g\|\vec{S_\theta}\|)$, and $D(h) = h_c^{m+1}\Big(\frac{h_p}{m+1}+\frac{h_c}{m+2}\Big) + C\,h^{m+1}$, with C the basal slip coefficient.

The driving slope $\|\vec{S_\theta}\|$ remains explicit in the final expression, but the formula now also depends on $\vec{q}$, which is what restores the dynamical coupling missing from the zeroth-order expression (6.2). Moreover, the slope-based closure gives a linear relation between the friction and the discharge, which makes the assumption in Section 3.4.2 of a linearised friction term for the semi-implicit treatment consistent with the actual rheology, and therefore more accurate than the regularised closure where the relation is non-linear.

The closure discussed in Chapter 4 addresses the same degeneracy by a different route. The depth integration of the constitutive law yields the relation $\bar{u} = f_{\mathrm{HB}}(\tau_b, h)$, which is then inverted to recover τ_b from $\bar{u} = \|\vec{q}\|/h$. The dynamical coupling with the discharge is therefore introduced through $\bar{u}$ as an input.

The two strategies are equivalent in steady uniform flows, where the velocity and the slope are linked by the steady relation. However, in unsteady or non-uniform flows, this correspondence breaks down: the observed couple $(\bar{u}, h)$ is no longer constrained to be consistent with the actual local slope, and $\|\vec{S_\theta}\|$ becomes an independent piece of information that the velocity-only inversion cannot recover.

6.2 Rheology regimes

The asymptotic analysis of Boutounet *et al.* (2016), taken up in Muchiri *et al.* (2025), classifies thin-layer flows by the orders of magnitude of three dimensionless groups: $\beta = \epsilon\,\mathrm{Re}$ (inertial), $\alpha = \epsilon\,\gamma$ (viscous), and $\delta = \epsilon/\gamma$ (pressure), with $\gamma = \mathrm{Fr}^2/\mathrm{Re}$ and $\epsilon = \mathcal{H}/L$. Two physically meaningful regimes for viscoplastic flows emerge from this scaling:

- **Regime A** ($\beta,\ \alpha,\ \delta \ll 1$): the pressure-gradient contribution is asymptotically negligible compared to gravity. The driving slope reduces to the gravitational component of the bed inclination. Muchiri *et al.* (2025) writes this in the mean-slope reference frame as:

$$\vec{S_\theta}^{\,A} = \sin\theta\,\hat{\mathbf{e}}_{\text{downstream}} \tag{6.4}$$

  where $\hat{\mathbf{e}}_{\text{downstream}}$ is the unit vector along the steepest descent direction and θ is the global mean inclination of the flume. This regime corresponds to thin, fast flows on steep slopes, where the free-surface gradient is small compared to the bed slope.

- **Regime B** ($\beta,\ \alpha \ll 1, \delta = O(1)$): the pressure-gradient contribution remains of leading order alongside gravity. The driving slope therefore includes a corrective term proportional to the free-surface gradient. In the mean-slope reference frame, the driving slope vector reads

$$\vec{S_\theta}^{\,B} = \sin\theta\,\hat{\mathbf{e}}_{\text{downstream}} - \cos\theta\,\nabla H \tag{6.5}$$

  where $H = z_b + h$ is the elevation of the free surface. The first term coincides with $\vec{S_\theta}^{\,A}$ and represents the gravitational driving force. The second term, $-\cos\theta\,\nabla H$, is the hydrostatic pressure-gradient correction inherited from $\delta = O(1)$. This regime captures slower flows with significant free-surface deformation, including the inertial phase of a dam-break where ∇h is locally steep.

  The corrective term just captures how the free-surface slope affects pressure: when $\partial_x h < 0$, the hydrostatic pressure decreases downstream and increases the driving force, an effect regime A ignores.

Both regimes share the same closure (6.3) and differ only in the construction of $\vec{S_\theta}$. In the limit $\nabla H \to 0$, regime B continuously degenerates into regime A.

6.3 Numerical implementation

The implementation of the slope-based closure in the Watlab code requires two key adaptations compared to the formulation described in Muchiri *et al.* (2025):

- The construction of the driving slope $\vec{S_\theta}$.
- The treatment of the null slope case.

Both adaptations are further developed in the following subsections.

6.3.1 Construction of the driving slope

The first important deviation from the formulation of Muchiri *et al.* 2025 concerns the construction of the driving slope $\vec{S_\theta}$. The original formulation is presented in a global mean-slope reference frame: a single mean slope θ is defined for the entire domain and $\hat{\mathbf{e}}_{\text{downstream}}$ is a fixed direction.

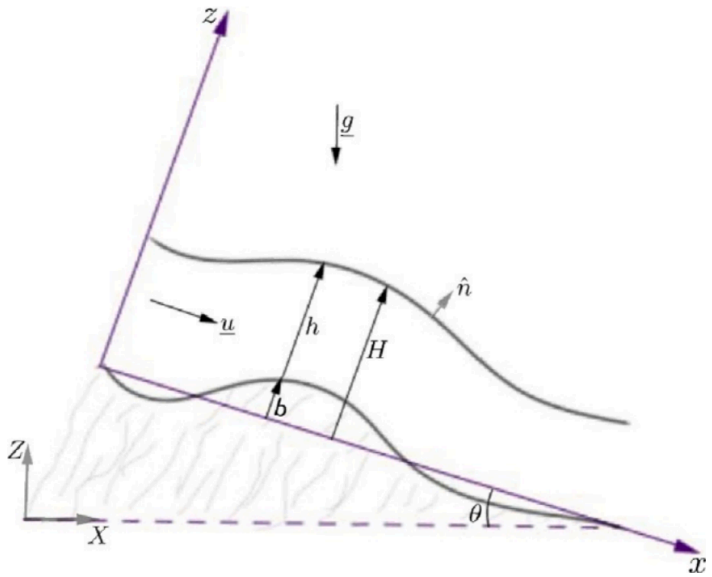


Fig 6.1. *Schematic of the mean-slope reference frame with non-flat topography, from Muchiri* et al. *(2025).*

The equations are solved on an idealised inclined plane. This is appropriate for the dam-break benchmark of Ancey *et al.* 2012, but too restrictive for mudflow simulations on natural topographies where neither the slope angle nor the downhill direction is constant.

The implementation in the Watlab code therefore relies on a local construction of the driving slope, where $\vec{S_\theta}$ is computed at each point of the domain from the local bed slope and surface gradient.

Local slope angle

Instead of a single global θ, a local inclination θ_{loc} is computed for every cell from the local bed gradient:

$$\tan\theta_{\text{loc}} = \|\nabla z_b\|, \qquad \cos\theta_{\text{loc}} = \frac{1}{\sqrt{1+\|\nabla z_b\|^2}}, \qquad \sin\theta_{\text{loc}} = \frac{\|\nabla z_b\|}{\sqrt{1+\|\nabla z_b\|^2}}.$$

The gradient ∇z_b for every cell is computed with a weighted least-squares method based on the cell and its neighbours as described in Syrakos *et al.* (2023).

Let $\vec{x_i}$ be the position of the centre of cell i and z_i^b the bed elevation at that point. For each neighbour $j \in \mathcal{N}(i)$ with $\mathcal{N}(i)$ the set of cells sharing a face with cell i, the first order Taylor expansion of the bed elevation around $\vec{x_i}$ reads:

$$z_j^b \approx z_i^b + \nabla z_b \cdot (\vec{x_j} - \vec{x_i})$$

Then, the least-squares method consists in finding the gradient ∇z_b that minimises the sum of squared residuals:

$$\nabla z_b = \arg\min_{\nabla z_b} \sum_{j\in\mathcal{N}(i)} w_{ij}^2 r_{ij}^2$$

where $r_{ij} = z_j^b - z_i^b - \nabla z \cdot (\vec{x_j} - \vec{x_i})$ is the residual for neighbour j and w_{ij} is a weight that can be chosen to improve the accuracy of the gradient estimation. In this work, the weights are set to $w_{ij} = \frac{1}{\|\vec{x_j} - \vec{x_i}\|}$, which gives more importance to closer neighbours, increases the accuracy on non-uniform meshes as explained in Syrakos *et al.* (2023).

The use of a local slope allows the closure to be applied on any topography without modification. On the dam-break benchmark, the local slope is uniform and equal to the global slope, so the implementation reduces exactly to that of the original paper.

Local slope direction

In the mean-slope frame of Muchiri *et al.* (2025), the slope direction $\hat{\mathbf{e}}_{\text{downstream}}$ is exactly aligned with the global mean slope and is therefore constant across the domain. This is appropriate for the dam-break benchmark, but not for natural topographies where the local steepest descent direction can vary significantly from point to point.

In this work, the slope direction is therefore computed locally from the bed gradient as the unit vector along the steepest descent:

$$\hat{\mathbf{e}}_{\text{downstream}} = -\frac{\nabla z_b}{\|\nabla z_b\|}$$

6.3.2 Treatment of the singular regime

A more detailed analysis of Equation 6.3 shows that the formulation becomes ill-defined when the driving slope $|\vec{S_\theta}|$ becomes small. Since this quantity appears in several denominators, the basal friction τ_b tends to infinity as $|\vec{S_\theta}| \to 0$.

Such a behaviour is consistent with the physical nature of flows over a horizontal bed, for which a steady uniform flow with non-zero velocity is both physically and mathematically impossible. Since steady uniform flows constitute the reference state used in the derivation of the closure law, it is therefore expected that the closure loses validity when this reference state itself becomes singular.

Nevertheless, this singular behaviour raises important issues for the numerical implementation, as realistic natural topographies often contain nearly flat regions or local basins where $|\vec{S_\theta}| \to 0$. The closure formulation must therefore be adapted in order to handle such situations in a stable and physically meaningful manner.

This singularity can be encountered in two distinct physical situations:

1. **Vanishing driving slope**: $\|\vec{S_\theta}\| \to 0$. The factor $\left(\frac{K}{\rho g \|\vec{S_\theta}\|}\right)^{m-1}$ in Equation 6.3 diverges (for $m > 1$, that is $n < 1$, which is the case of most viscoplastic materials including the Carbopol of the benchmark). This typically occurs on a horizontal bed in regime A, or in regime B when both ∇z_b and ∇h are small.

2. **Plug-dominated state**: the gravitational driving force $\rho g h \|\vec{S_\theta}\|$ falls below the yield stress τ_y, so that $h_p \geq h$. The sheared thickness $h_c = \max(0, h - h_p)$ then vanishes, and the denominator $D(h)$ collapses to $C\, h^{m+1}$. With the no-slip condition $C = 0$ retained throughout this work, $D = 0$ and the closure produces an infinite friction.

   This singularity is again a limitation of the closure rather than a physical property of the flow itself. Indeed, the criterion only compares the gravitational driving force to the yield stress and is therefore independent of the local velocity. It relies on the same zeroth-order expression responsible for the degeneracy discussed in Section 6.1. As a result, a fluid element carrying inertia from upstream can perfectly well transit through this state without being at rest. The divergence of τ_b only signals that the closure has stepped outside its domain of validity.

In order to handle these singular cases, both are detected at the start of the source-term evaluation through the criterion

$$\|\vec{S_\theta}\|^2 < \varepsilon_S \quad \text{or} \quad \rho g h \, \|\vec{S_\theta}\| \leq \tau_y, \tag{6.6}$$

with $\varepsilon_S = 10^{-12}$. The first inequality[2] covers case (1). The second covers case (2) and is in fact the exact physical condition $h_p \geq h$. When either condition is satisfied, the source term falls back to the regularised Newton-Raphson solver of Chapter 4 with $M = 50$. Indeed, as this closure does not rely on the driving slope, it is well-defined in both cases and produces a finite friction.

This hybrid strategy is what makes the closure usable in practice on real terrains. On the canonical Carbopol flume the bed slope is uniform and well above zero everywhere, so the fallback is rarely if ever triggered. On a natural topography, by contrast, flat pockets, basins, and the deposit itself feature regions where $\|\vec{S_\theta}\| \to 0$, and a closure that diverges there is unusable; the fallback gives the implementation a graceful, physically sensible behaviour in those regions.

6.4 Benchmark Result and discussion

In order to evaluate the performance of the two new implementations of the rheology, the dam-break benchmark of Chapter 5 is repeated under identical conditions. The numerical setup, the quantities of interest and the comparisons with the literature are kept identical to those described in Section 5.2, so that any difference observed can be attributed to the closure of τ_b alone. As detailed in Section 6.3.2, the regularised solver with $M = 50$ is retained as the fallback for the singular cells. On this benchmark, however, the bed slope is uniform at $\theta = 15^\circ$ and the fallback is only triggered marginally, near the deposit edges where $h_p \geq h$. Both regimes are tested for mesh convergence on the same three resolutions $l_c \in \{0.03,\ 0.01,\ 0.005\}$ m at fixed $\mathrm{CFL} = 0.4$.

The discussion is organised around the same four quantities of interest as in Chapter 5: front position, front velocity, depth at the gate, and depth profiles along the flume axis. For each quantity, the regime A and regime B results are first analysed separately, then compared together with the regularised closure in Section 6.4.3.

[2] The squared form is used purely for numerical efficiency, as it avoids the evaluation of a square root at every cell and remains well-conditioned as $\|\vec{S_\theta}\| \to 0$. It leaves the test unchanged, since $\|\vec{S_\theta}\|^2 < \varepsilon_S$ is equivalent to $\|\vec{S_\theta}\| < \sqrt{\varepsilon_S}$, so that the effective threshold on the driving slope is $\sqrt{\varepsilon_S} = 10^{-6}$.

6.4.1 Regime A

Front position and front velocity

The front position $x_f(t)$ and front velocity $u_f(t)$ obtained with the regime A are shown in Figures 6.2 and 6.3, respectively. A clear improvement is observed compared to the regularised closure of Chapter 5, with a markedly better agreement with the experimental data over the whole simulation. The initial front position is recovered almost exactly, and the systematic overshoot that characterised the regularised closure during the inertial phase is now strongly reduced. The same kind of overshoot is still present, but with a much smaller amplitude. During the spreading phase, the front velocity is exactly reproduced, and the front position follows the experimental data closely, although shifted because of the initial overshoot.

The initial front velocity is accurately reproduced, marking a significant improvement compared with the regularised closure, which systematically overpredicted this quantity. Due to its depth-averaged formulation, the model is unable to reproduce the oscillations observed experimentally during the inertial phase. These oscillations are likely associated with the gate-opening dynamics and with uncertainties in front-position measurements when the flow thickness becomes very small. Despite this limitation, the new closure reproduces the overall evolution of the front velocity far more accurately than the regularised closure, which consistently overestimates it throughout this phase.

A clear mesh convergence is observed: the curves shift towards the experimental data as the mesh is refined, with stable behaviour and no significant oscillation across the three resolutions.

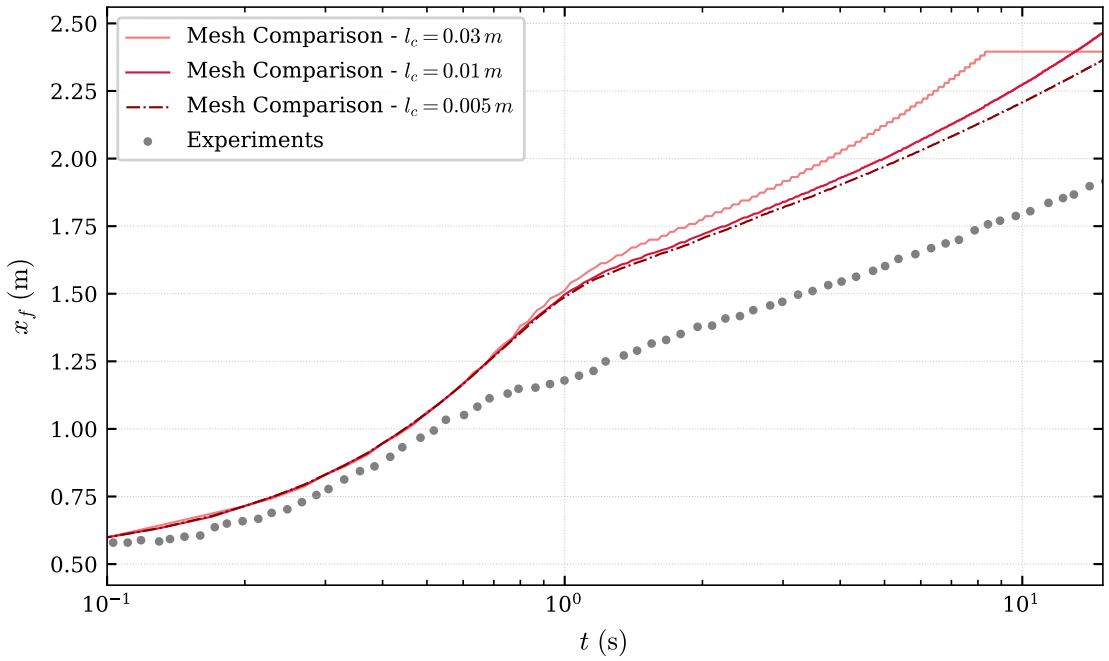


Fig 6.2. *Front position $x_f(t)$ as a function of time for three mesh sizes ($M = 50$, $\mathrm{CFL} = 0.4$) with regime A rheology, compared with the experimental data of Ancey* et al. *(2012).*

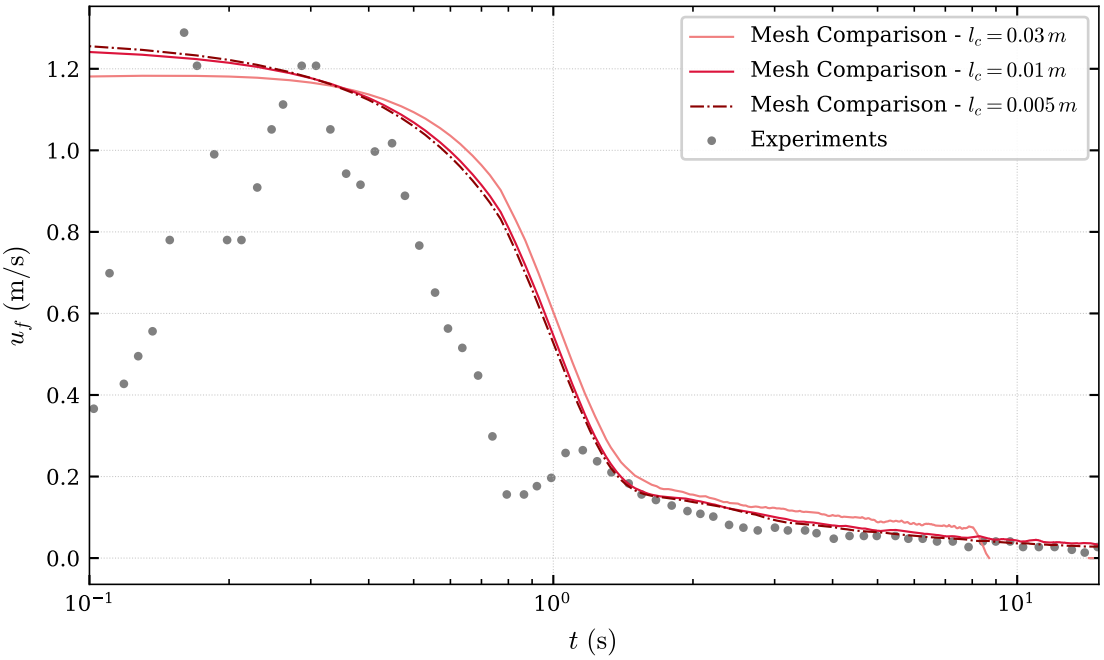


Fig 6.3. *Front velocity $u_f(t)$ as a function of time for three mesh sizes ($M = 50$, $\mathrm{CFL} = 0.4$) with regime A rheology, compared with experiments.*

Depth at the gate

The depth at the gate $h(x{=}0,\, t)$ is shown in Figure 6.4. The behaviour is qualitatively the same as with the regularised closure: a rapid decrease following the gate release, however, the slow asymptotic approach to a finite resting height is much sharper. Unlike the regularised closure, however, the converged final height settles above the theoretical plug-flow arrest height $h_p = 0.0102$ m rather than slightly below it.

This residual offset must be attributed to the stopping criterion of the numerical scheme described in Section 3.4, which allows the flow to arrest but is not finely calibrated to capture the exact theoretical equilibrium above h_p.

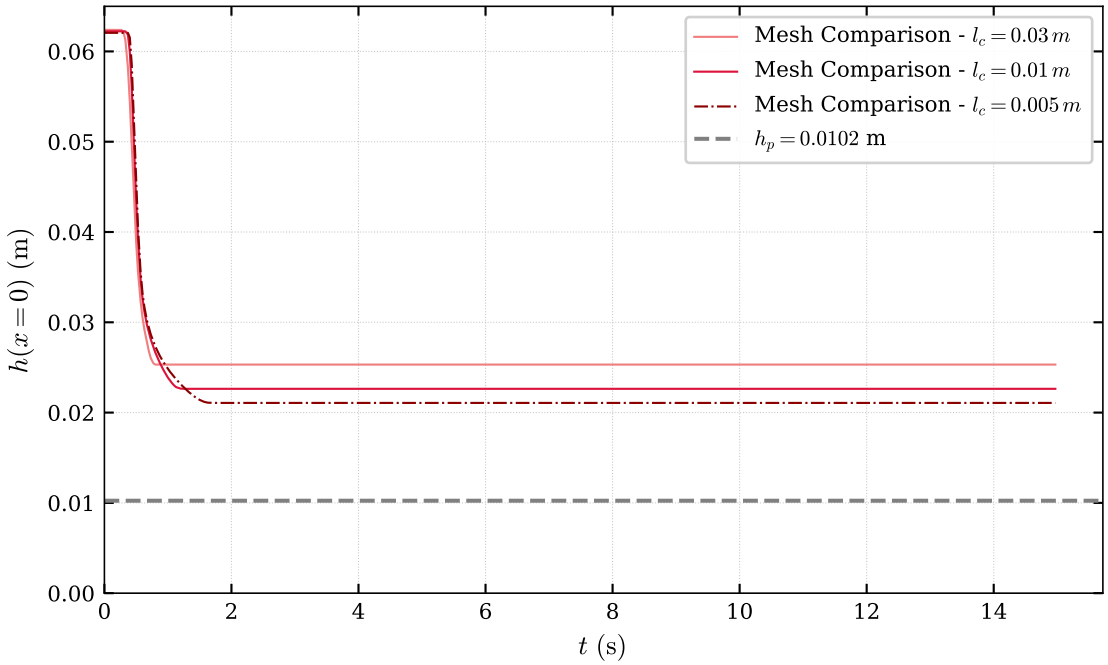


Fig 6.4. *Flow depth $h(x{=}0, t)$ at the gate location for three mesh sizes ($M = 50$, $\mathrm{CFL} = 0.4$) with regime A rheology. The dashed line indicates the theoretical plug-flow arrest height $h_p = 0.0102$ m.*

Depth profile

The free-surface profiles along the flume axis at different times are shown in Figure 6.5. The three resolutions share the same overall profile shape with a reservoir region near the gate with a converging thickness. The coarsest mesh exhibits a visible step-like structure at the front, due to the discrete advance of the wetted region one cell at a time, while the two finer meshes are essentially superimposed. The profile shapes themselves are very similar to those produced by the regularised closure on the same benchmark.

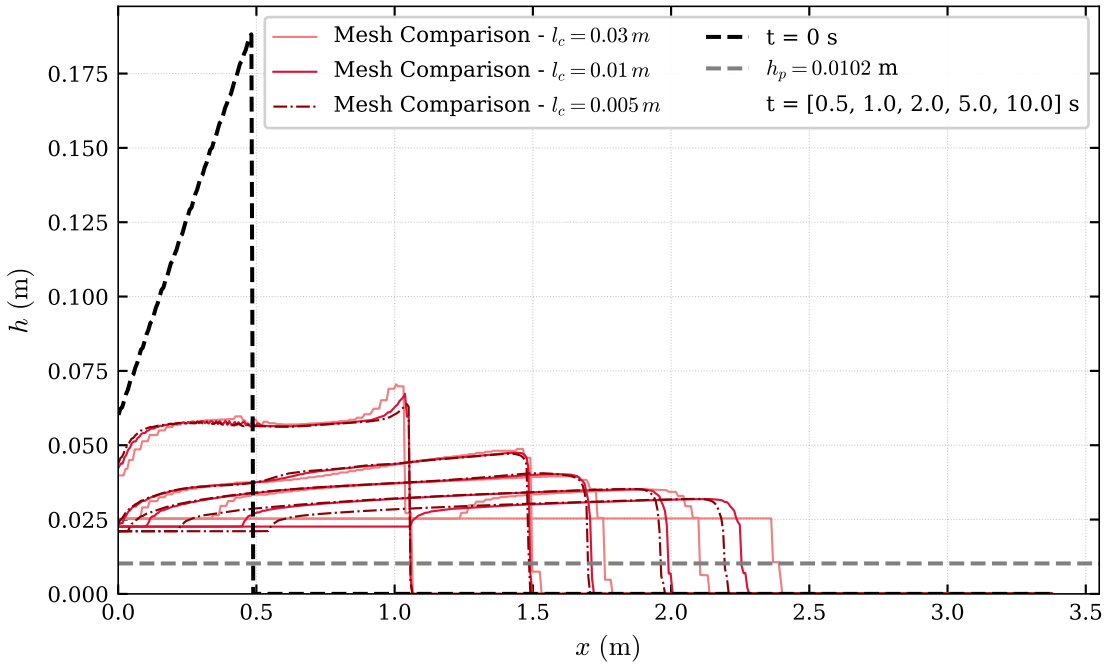


Fig 6.5. *Free-surface profiles along the flume axis at $t \in \{0.5,\ 1.0,\ 2.0,\ 5.0,\ 10.0\}$ s for three mesh sizes ($M = 50$, $\mathrm{CFL} = 0.4$) with regime A rheology.*

Comparison with the literature

Figure 6.6 positions the present implementation among the literature predictions for the same benchmark. The regime A of this work clearly outperforms the closure of Fernández-Nieto *et al.* (2023) during the inertial phase, even though both terminate at similar long-time positions. It still remains noticeably above the regime A result reported in Muchiri *et al.* (2025), which is itself in good agreement with the experimental data.

The remaining gap with respect to the original paper is consistent with the implementation choices of a slightly different numerical scheme and with the absence in this work of the additive momentum correction discussed in Section 5.4.2.

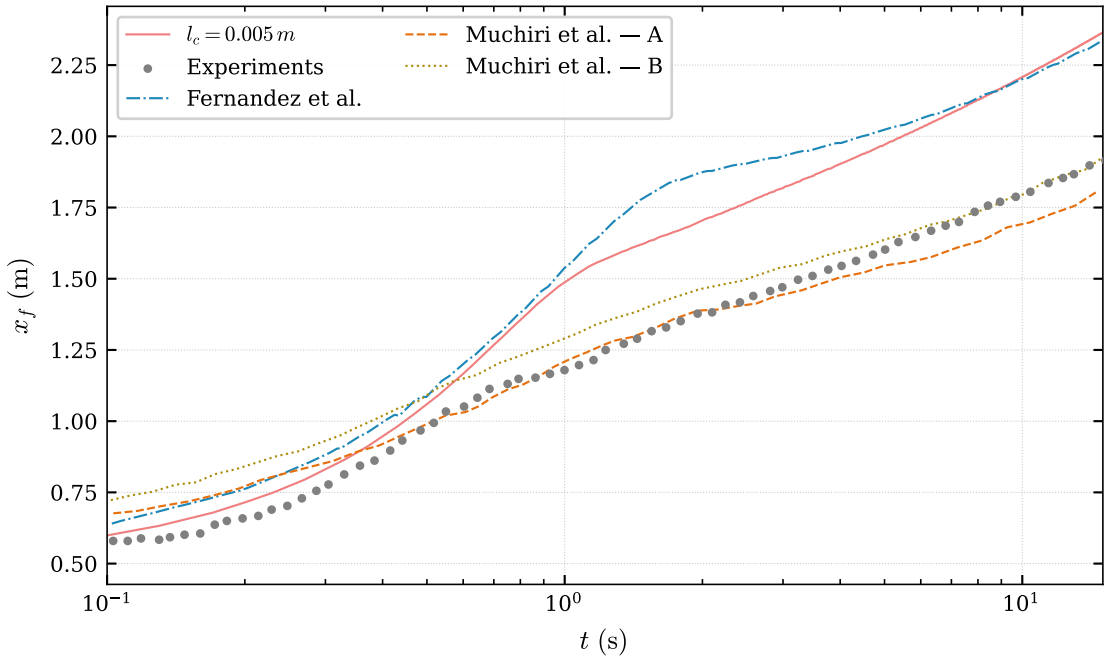


Fig 6.6. *Comparison of the front position $x_f(t)$ obtained in this study with the regime A rheology and the results from Fernández-Nieto* et al. *(2023) and Muchiri* et al. *(2025), alongside the experimental data.*

6.4.2 Regime B

Front position and front velocity

The mesh convergence of regime B in Figure 6.7 mirrors that of regime A, with the same plateau on the coarsest mesh and the two finer meshes converging close to one another. The position curves of regime B sit slightly above those of regime A during the inertial phase. The initial front position is overestimated more strongly than with regime A, but the two regimes converge to nearly the same long-time front position by the end of the simulation.

The most distinctive feature of regime B is the deceleration–re-acceleration visible around $t \approx 1$ s on the front velocity of Figure 6.8. This feature is absent from regime A and from the regularised closure, but it is also visible, on the experimental velocity. Regime B is therefore the only implementation of the three to capture this transient feature. The initial velocity is higher than in regime A, but it reproduces the experimental data much better after $t \approx 0.2$ s.

The mechanism behind this distinct behaviour is the corrective term $-\cos\theta_{\mathrm{loc}}\,\nabla h$ that distinguishes regime B from regime A. Near the front, where $\partial_x h < 0$ is steep, the corrective term aligns with the gravitational driving force and increases $\|\vec{S_\theta}\|$. Through the prefactor $\|\vec{S_\theta}\|^{1-m}$ with $m \approx 3$, a larger driving slope produces a smaller basal friction in the head of the wave: regime B initially propagates faster, and only later decelerates more strongly once the head has spread and $\partial_x h$ has flattened. The slightly higher position curve in the early phase therefore comes paired with the deceleration that follows, and the two effects compensate by the spreading phase.

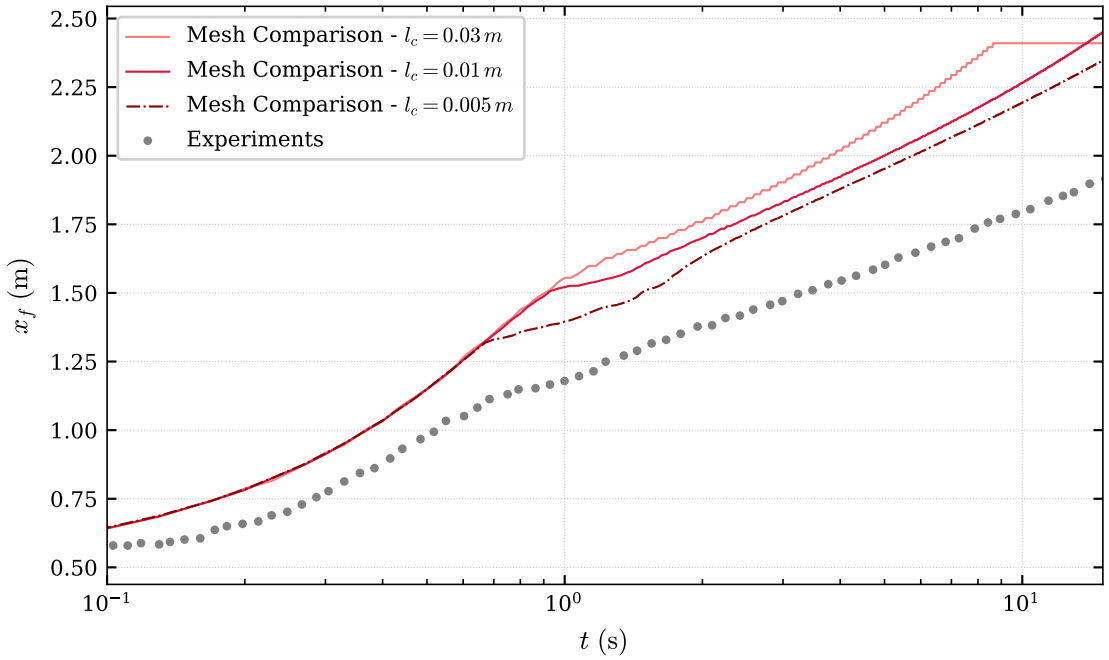


Fig 6.7. *Front position $x_f(t)$ as a function of time for three mesh sizes ($M = 50$, $\mathrm{CFL} = 0.4$) with regime B rheology, compared with the experimental data of Ancey* et al. *(2012).*

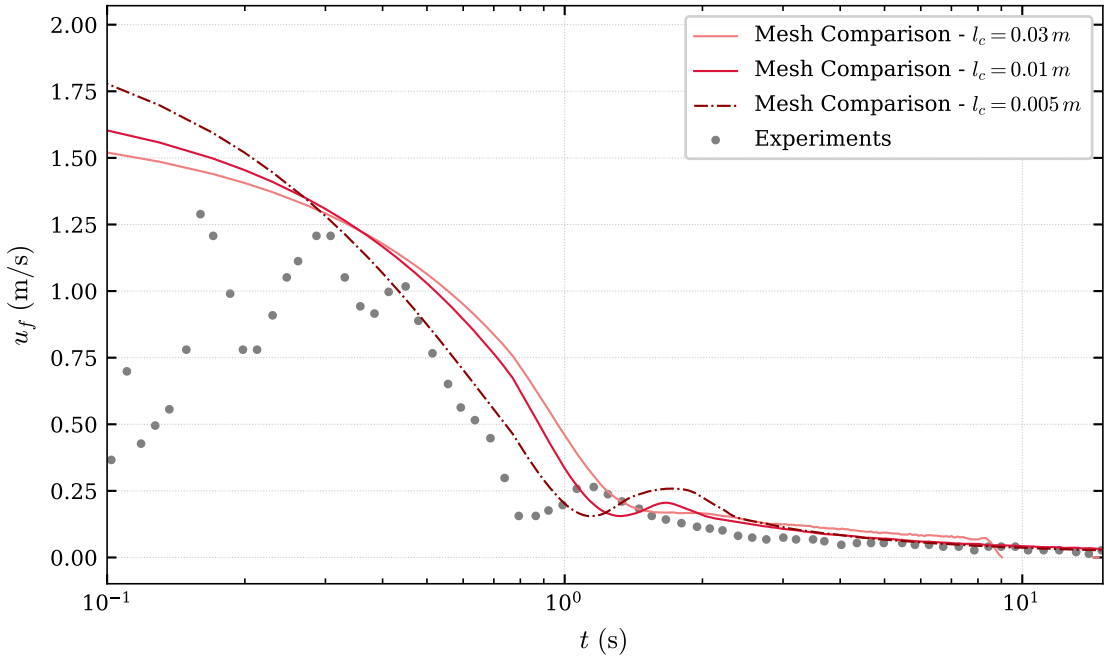


Fig 6.8. *Front velocity $u_f(t)$ as a function of time for three mesh sizes ($M = 50$, $\mathrm{CFL} = 0.4$) with regime B rheology, compared with experiments.*

Depth at the gate

The depth at the gate $h(x{=}0,\,t)$ is shown in Figure 6.9. The behaviour is qualitatively similar to that of regularised closure, with a rapid decrease following the gate release and a slow asymptotic approach to a finite resting height. The final resting height is closer to the theoretical plug-flow arrest height $h_p = 0.0102$ m than in regime A, which suggests that the stopping criterion of Section 3.4 is better calibrated for this regime.

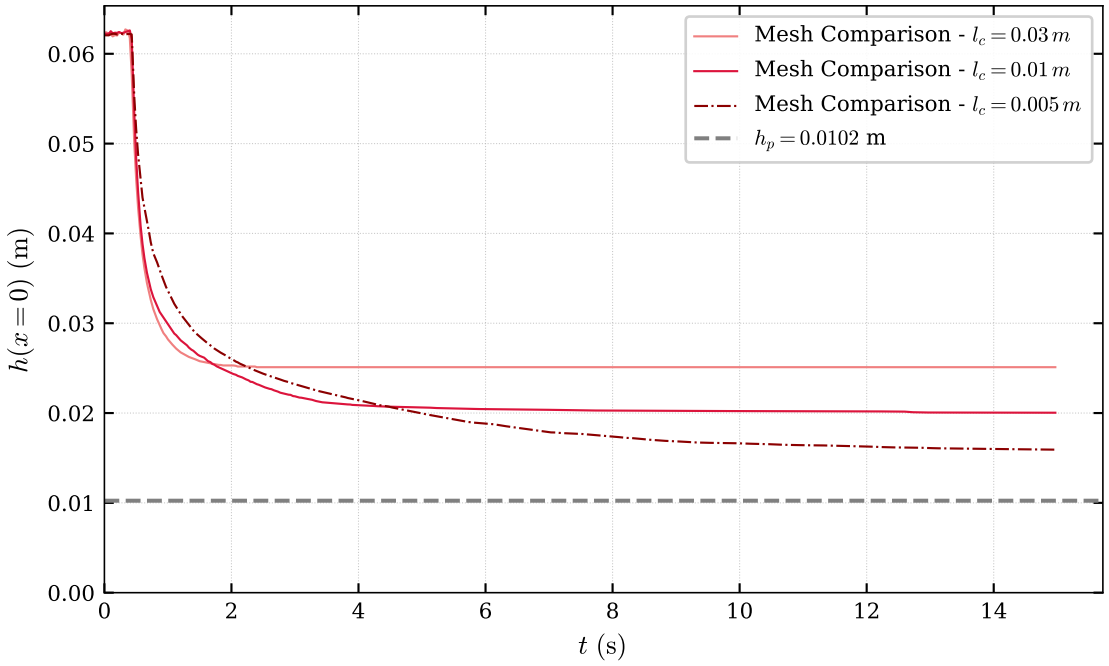


Fig 6.9. *Flow depth $h(x{=}0,\,t)$ at the gate location for three mesh sizes ($M = 50$, $\mathrm{CFL} = 0.4$) with regime B rheology. The dashed line indicates the theoretical plug-flow arrest height $h_p = 0.0102$ m.*

Depth profile

The free-surface profiles along the flume axis at different times are shown in Figure 6.10. The three resolutions share the same overall profile shape, with a reservoir region near the gate and a converging thickness. However, the profiles of regime B are smoother at the transition between the constant thickness reservoir and the front, while those of regime A feature a sharper step-like structure. This is consistent with the $-\cos\theta_{\mathrm{loc}}\,\nabla h$ corrective term of regime B, which adapts the friction to the local free-surface gradient and therefore produces a smoother profile. A local and limited noise is visible on the profiles of regime B, which is likely due to the numerical evaluation of ∇h and its coupling with the friction term. However, this noise does not seem to affect the overall convergence of the results.

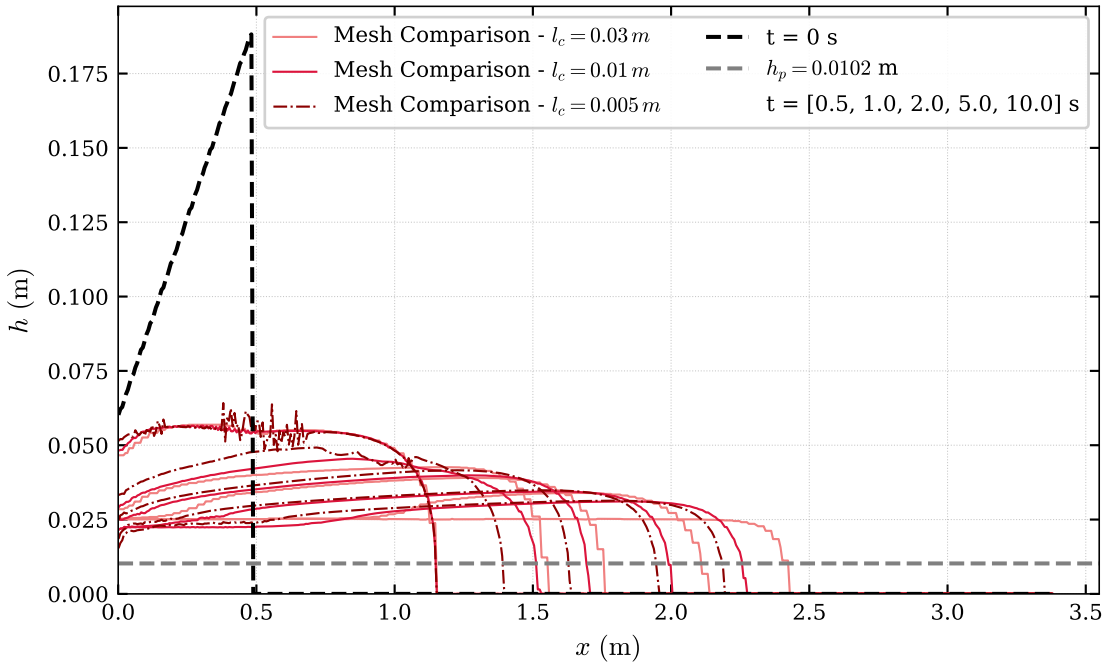


Fig 6.10. *Free-surface profiles along the flume axis at $t \in \{0.5,\ 1.0,\ 2.0,\ 5.0,\ 10.0\}$ s for three mesh sizes ($M = 50$, $\mathrm{CFL} = 0.4$) with regime B rheology.*

Comparison with the literature

Figure 6.11 shows that the present regime B implementation tracks the regime B of Muchiri *et al.* (2025) closely during the inertial phase, where both curves trace nearly the same trajectory. The two then diverge: the original paper continues smoothly towards the experimental data, while the present implementation drifts upward and ends up close to the result of Fernández-Nieto *et al.* (2023). The same attribution discussed for regime A applies here, with the additive momentum correction of Section 5.4.2 being the most plausible explanation for the long-time drift.

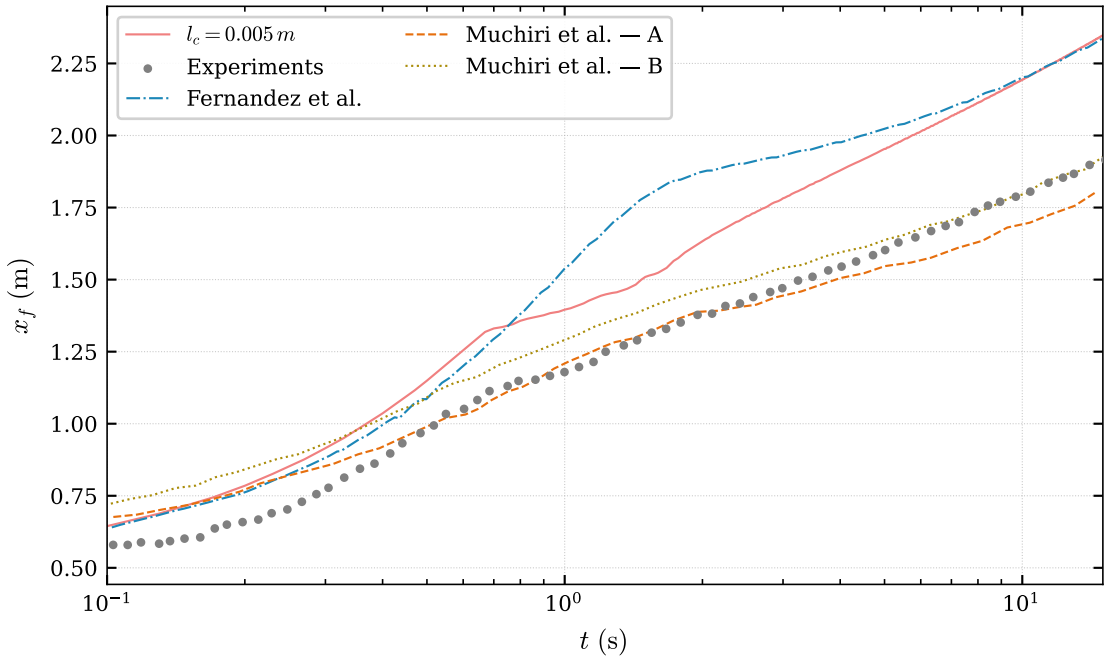


Fig 6.11. *Comparison of the front position $x_f(t)$ obtained in this study with the regime B rheology and the results from Fernández-Nieto* et al. *(2023) and Muchiri* et al. *(2025), alongside the experimental data.*

6.4.3 Comparison between three implementations

This subsection brings the three rheological implementations developed in this work; the regularised closure of Chapter 5, the regime A, and the regime B together on the same axes, in order to assess the global improvement and to discuss the practical trade-offs between accuracy, computational cost, and conservatism with respect to safety.

The contrast in front position between the three implementations is the clearest illustration of the improvement brought by the new closure. The regularised closure produces a substantial overshoot of the experimental front position throughout the simulation, while the two regimes reduce this overshoot. During the first $t \approx 0.8$ s, the three implementations provide substantially the same front position. Then, the main improvement of both regimes comes from the reduction of the front position overshoot between $t \approx 0.8$ s and $t \approx 1.2$ s, which is the phase where the flow transitions from the inertial phase to the spreading phase. The Figure 6.12 clearly shows that the regime A and regime B of this work track the experimental front position much better than the regularised closure during this critical phase, with a much smaller overshoot. The regime B is the most accurate during this transition. Finally, during the spreading phase, the three implementations converge to a similar behaviour in front velocity, the front position being different only because of the initial overshoot.

The final overshoot and global behaviour are present in all three implementations and in the results of Fernández-Nieto *et al.* (2023), which suggests that this error is not a closure artefact but originates from another modelling element common to all three approaches, most plausibly

the absence of the additive momentum correction discussed in Section 5.4.2.

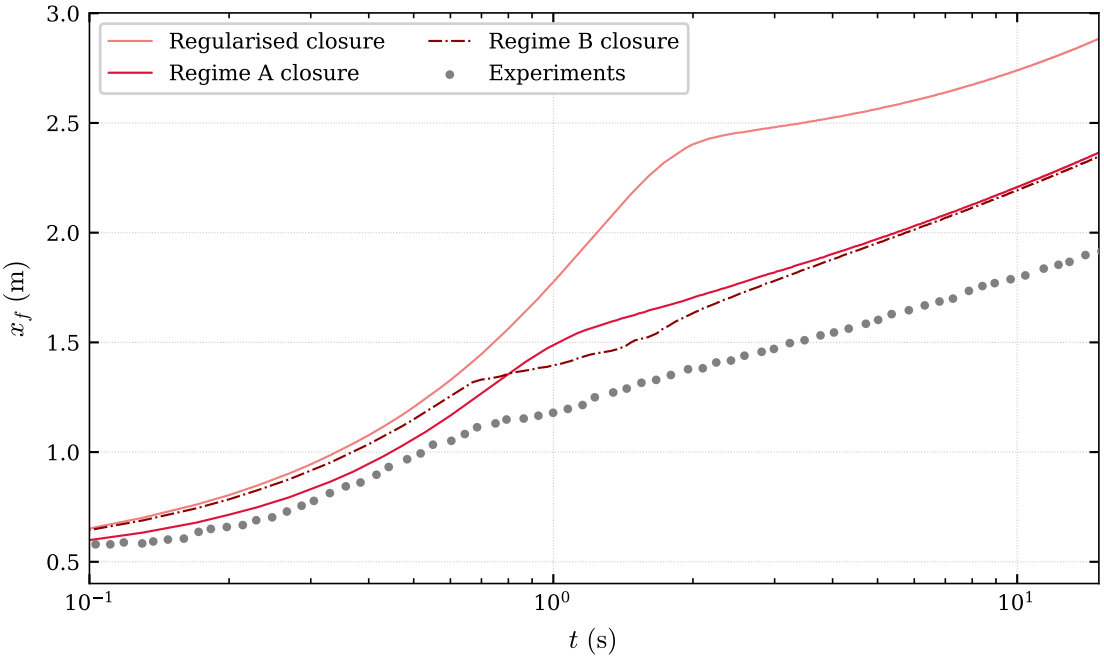


Fig 6.12. *Comparison of the front position $x_f(t)$ obtained with the three implementations of the rheology (regularised, Regime A and Regime B) with the experimental data from Ancey* et al. *(2012).*

The front velocity (see Figure 6.13) tells a more nuanced story than the front position. The regularised closure produces a smooth and broad peak during the inertial phase. Regime A produces a lower and shorter peak, closer in amplitude to the experimental signal. Regime B produces the highest peak of the three, but decays substantially faster, and is the only implementation that reproduces the deceleration–re-acceleration feature of the experimental signal around $t \approx 1$ s. None of the three implementations captures the oscillations of the experimental signal during the inertial phase.

After the inertial phase, the three curves converge to the same slow spreading velocity, in close agreement with the experiment. This convergence is not a coincidence: during the spreading phase, the flow is locally close to a steady, uniform state, so the observed couple $(\bar{u},\ \|\vec{S_\theta}\|)$ approaches the steady relation $\bar{u} = f_{\mathsf{HB}}(\rho g h \|\vec{S_\theta}\|,\ h)$ around which both closures are derived. In this regime, the equivalent driving slope $\|\vec{S_\theta}^{\,\mathsf{eq}}\|$ inferred by the regularised closure from the velocity coincides with the geometric driving slope $\|\vec{S_\theta}^{\,\mathsf{obs}}\|$ used directly by the two regimes, so the three implementations produce the same basal stress and therefore the same dynamics.

The choice of closure therefore matters chiefly for the early inertial phase, where the steady relation does not hold locally, and the two parametrisations diverge, exactly the situation anticipated in Section 6.1. It is also worth noting that, despite radically different velocity profiles during the inertial phase, the two Muchiri regimes integrate to nearly the same long-time front position.

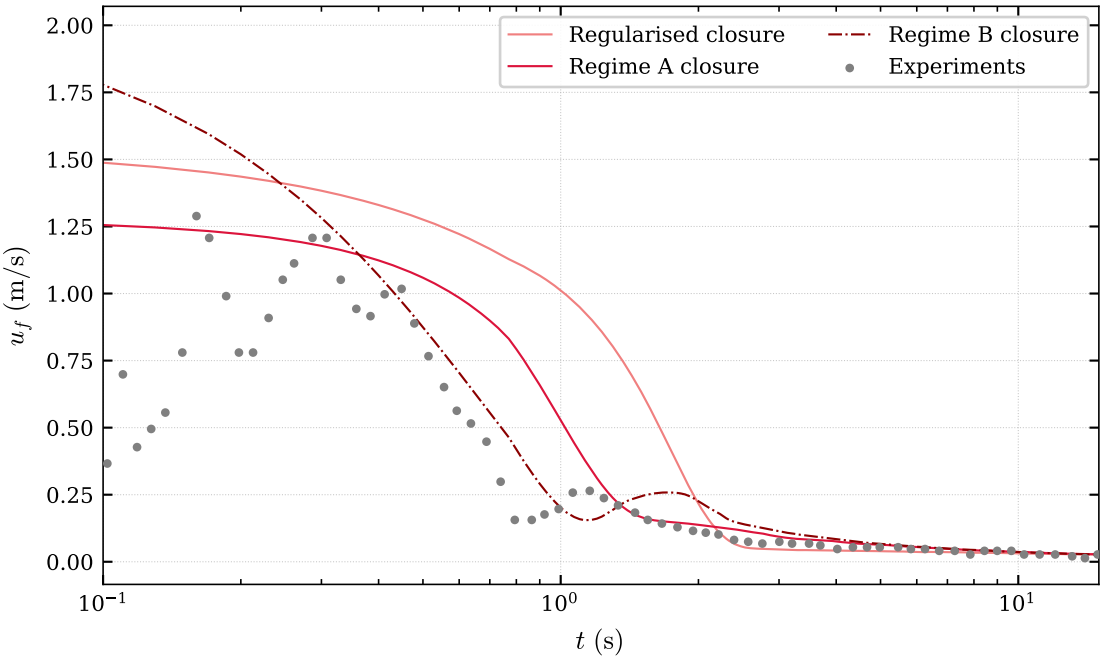


Fig 6.13. *Comparison of the front velocity $u_f(t)$ obtained with the three implementations of the rheology (regularised, Regime A and Regime B) with the experimental data from Ancey* et al. *(2012).*

The depth at the gate (see Figure 6.14) closes the comparison: the three implementations produce essentially identical curves, all converging to a value close to h_p. The two Muchiri regimes converge slightly above h_p while the regularised closure converges slightly below. This suggests that the offset is set by the stopping criterion of the numerical scheme rather than by the closure itself, and that small changes in the timing of the arrest can flip the convergence to the other side of h_p. However, it is worth noting that the regime B converges slightly closer to h_p than regime A.

For a hazard-assessment application, the Muchiri convergence above h_p is in fact preferable to the regularised convergence below. Predicting a deposit slightly thicker than the theoretical equilibrium is conservative. It overestimates the volume retained at any given section of the channel, and therefore the local impact on infrastructure or terrain. Predicting a deposit thinner than h_p, conversely, would underestimate the residual mass and could lead to a non-conservative hazard map. The two Muchiri regimes therefore combine a more accurate inertial-phase dynamic with a more conservative deposit prediction, which is the most useful pairing for prevention purposes. A similar conclusion can be drawn from the front position: the smaller overshoot of the two regimes is more accurate, but also more conservative than the larger overshoot of the regularised closure, which overestimates the run-out distance and therefore the hazard area.

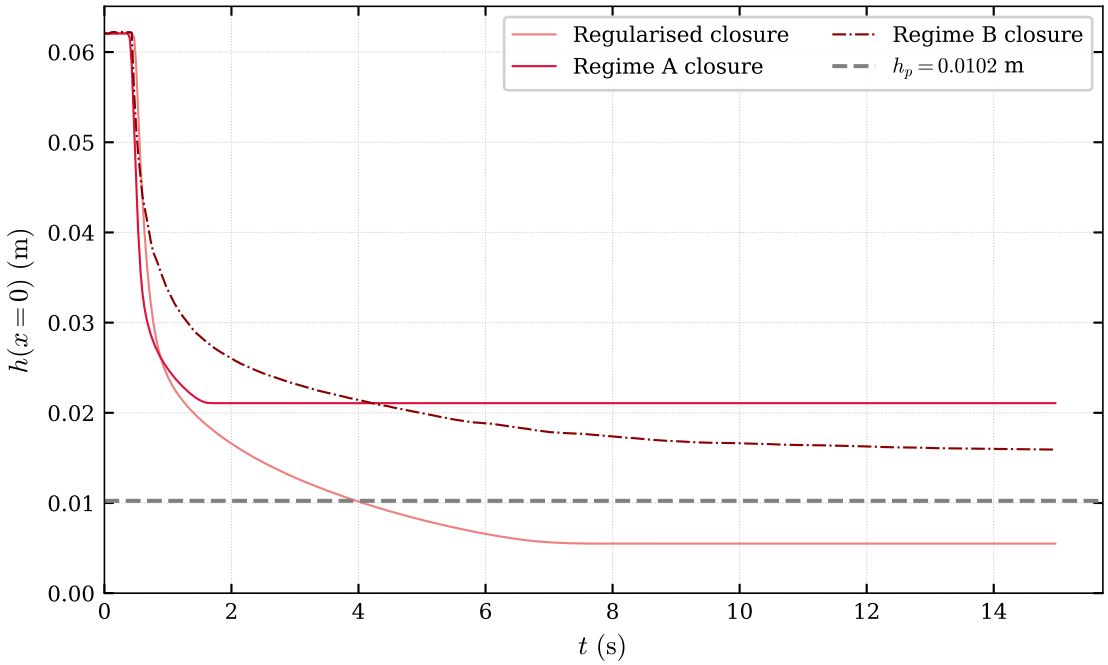


Fig 6.14. *Comparison of the flow depth at the gate $h(x{=}0,\,t)$ obtained with the three implementations of the rheology (regularised, Regime A and Regime B) with the experimental data from Ancey* et al. *(2012).*

6.4.4 Time computation

Effect of the closure choice

The wall-clock computation times reported in Table 6.1 reveal a substantial speed-up of both Muchiri implementations over the regularised closure on every mesh size tested, with the speed-up of regime A reaching about a factor of six on the finest mesh. This gain comes directly from the elimination of the per-cell Newton-Raphson inversion: the slope-based closure evaluates τ_b in a fixed, small number of operations, whereas the regularised closure performs several iterations per cell to converge $\bar{u}(\tau_b) \to \bar{u}_{\text{cell}}$, with the iteration count growing as the local stiffness of the relation increases.

Table 6.1. *Computation time for the benchmark simulations for different mesh sizes and closure formulations (CFL = 0.4, 15 seconds of simulated time, AMD Ryzen 7 7735HS, 16 threads).*

Mesh size l_c (m)	Computation time (s)		
	Regularised closure	Regime A	Regime B
0.03	16	8	10
0.01	233	48	62
0.005	2051	333	523

The speed-up grows with mesh refinement: on the coarsest mesh, the simulation runtime is dominated by overheads such as mesh management and output, and the closure cost is comparatively minor. On the finest mesh, the closure cost dominates the runtime, and the saving from the explicit formula compounds across all cells and all time steps.

Effect of the regime choice

Regime B is consistently more expensive than regime A, with the gap widening on the finer meshes. This overhead is entirely attributable to the LSQ reconstruction of ∇h at every time step, which regime A does not perform: the bed gradient ∇z_b is reconstructed once at initialisation, whereas ∇h must be reconstructed at every step on a field that may be discontinuous near the front.

6.5 Global limitations of the benchmark

The results obtained on the Carbopol dam-break benchmark, however convincing, only validate the implementation in a controlled laboratory setting. Two classes of limitations restrict the conclusions that can be drawn for the targeted mudflow application.

6.5.1 Limitations related to mudflow application

The first and most important limitation is that Carbopol ultrez 10 is not a natural mud. It is a transparent, water-swollen polymeric gel, deliberately chosen because it behaves as an idealised Herschel-Bulkley fluid. Its rheological parameters are stable, reproducible and very well characterised in the literature. The Carbopol benchmark thus tests whether the model correctly reproduces the dynamics of an idealised Herschel-Bulkley fluid. It does not test the predictive capability of the model for a real mudflow.

The mapping from this idealised material to natural mud or debris-flow material introduces several additional sources of uncertainty. First, the rheological parameters themselves are difficult to measure for natural mud: the yield stress τ_y, the consistency K and the flow index n depend on the solid volume fraction, the grain-size distribution, the mineralogical composition and numerous other physical properties. Reported values for similar-looking materials can differ by orders of magnitude, and even if the constitutive model is exact, the predictive accuracy of any simulation is bounded by the accuracy of these input parameters.

Second, real mudflows exhibit a number of physical phenomena that the present depth-averaged Herschel-Bulkley framework does not represent: bed entrainment and erosion that change the flow volume during run-out, pore-pressure dynamics in the granular phase, segregation of coarse particles towards the front, *etc*. The Carbopol benchmark, by construction, cannot test the model on any of these.

6.5.2 Deposit geometry and material

A second limitation concerns what the benchmark does not test, even within its idealised setting. The quantities of interest reported in this work and in Chapter 5 characterise the flow dynamics during run-out, but they do not directly characterise the geometry of the final deposit.

For engineering and hazard-assessment purposes, the final deposit shape including its lateral extent, its thickness distribution, and the position of its edges is often the primary output of interest. The benchmark of Ancey *et al.* 2012 provides a clean validation of the run-out dynamics, but it is essentially 1D and does not constrain the lateral spreading or the detailed shape of the final stop.

CHAPTER 7

Validation on a real-material mudflow

The benchmark from Ancey *et al.* (2012) used in Chapter 5 and Chapter 6 demonstrated that the model can reproduce the dynamics of an idealised Herschel-Bulkley fluid. As discussed in Section 6.5, this validation leaves two important questions unanswered:

- Does the model behave correctly when applied to a natural mud rather than a polymeric gel?
- Does the model capture the geometry of the final deposit, which is the main concern in engineering and hazard-assessment purposes?

The benchmark presented in this chapter, first presented and part of the Master's thesis of Liesse (2026), addresses both questions. It is based on an experimental campaign carried out at Politecnico di Milano, involving the release of a natural clayey-to-silty sand mixed with water into an inclined channel and the spreading and deposition on a horizontal plane downstream of the channel.

7.1 Experimental setup

A detailed description of the experimental setup can be found in Liesse (2026). Only the elements relevant to the validation are summarised here.

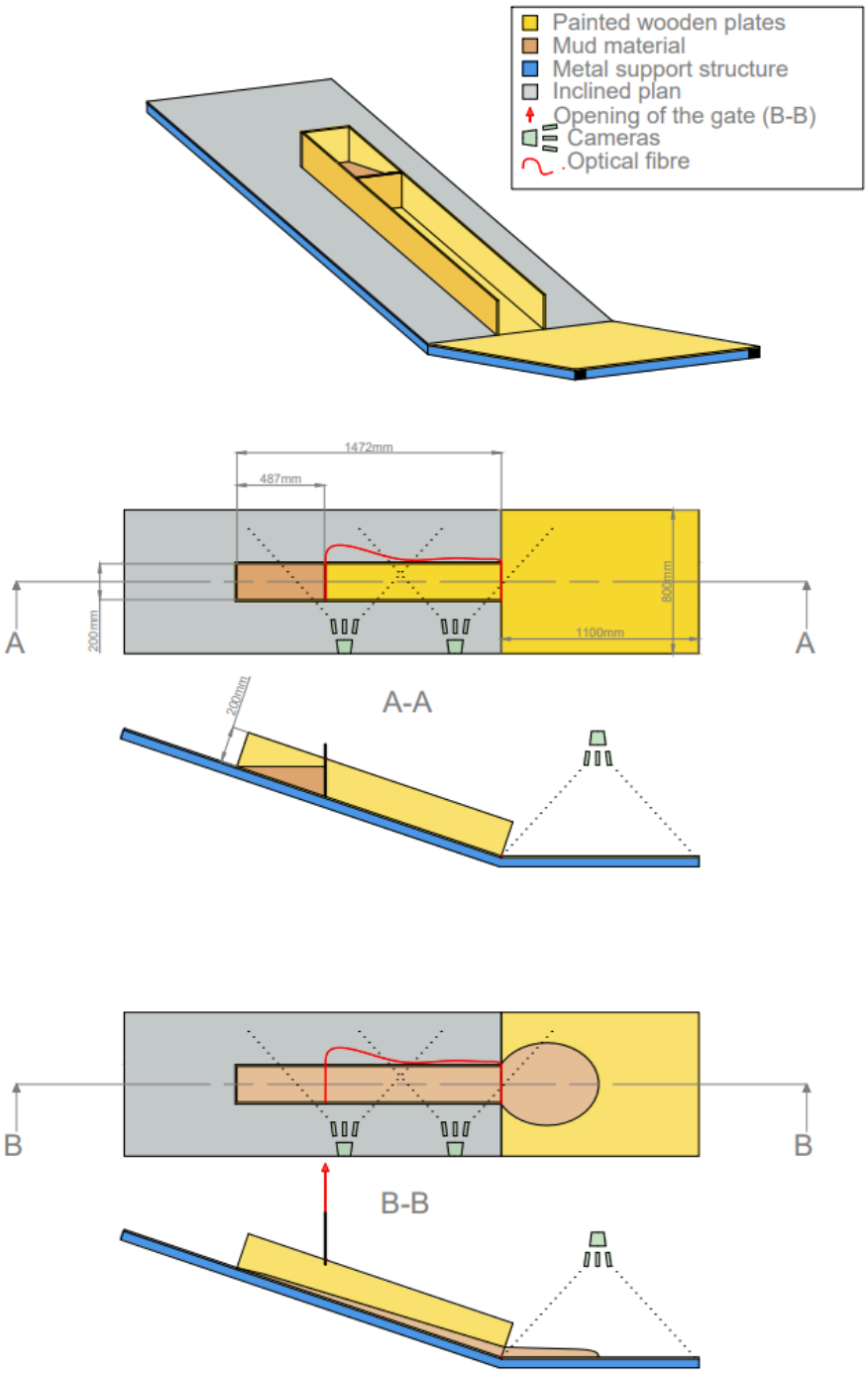


Fig 7.1. *Experimental setup of the Polimi benchmark, from Liesse (2026).*

The setup, shown in Figure 7.1, consists of a wooden channel of dimensions 1472×200 mm mounted on a scaled-down landslide simulator with adjustable slope. The material is stored upstream of a vertical wooden gate in a reservoir of length 487 mm and is released onto a horizontal deposition plane of 1100×800 mm at the downstream end of the channel.

A run proceeds as follows. The mixture is prepared in an external box, weighed and placed behind the gate with the channel still horizontal. The depth of material in the reservoir is recorded so that the initial volume and bulk density can be calculated. The channel is then tilted to the targeted slope and the gate is rotated to remain vertical, a requirement for a consistent representation of the initial condition in a depth-averaged framework. The gate is finally opened by a quick upward motion at about 19 m/s, more than an order of magnitude faster than the front velocity, so that the release can be treated as instantaneous.

Three independent measurement systems are used. A set of GoPro-type cameras records the flow at $\Delta t = 0.1$ s or 0.2 s, both inside the channel and on the deposition plane. The colour contrast between the brown mud and the yellow-painted plates allows the front position and the flow heights to be reconstructed by image processing. An optical fibre placed at the gate and at the channel outlet records the gate opening time and the passage of the front, providing a precise estimate of the mean front velocity V_m in the channel. Once the material has stopped, a laser scan of the deposit yields the final geometry on the horizontal plane.

7.1.1 Reference experiment

Multiple tests were carried out with different slopes, initial volumes and bulk densities. The present work focuses on experiment T08, which is the steepest slope and most energetic flow, and therefore the most challenging for the model. Its initial conditions and the measurements are summarised in Table 7.1.

Table 7.1. *Initial conditions and measurements for experiment T08, from Liesse (2026).*

Quantity	Symbol	Value
Channel slope	θ	33°
Initial volume	V_0	8.0×10^{-3} m^3
Bulk density	ρ_{tot}	2203.64 kg/m^3
Flow duration	t_D	8 s
Runout distance	L_{run}	1.666 m
Deposit area	A_{dep}	0.337 m^2
Mean front velocity (channel)	V_m	1.467 m/s
Peak velocity (deposition)	V_f	0.38 m/s
Maximum height, middle point (40 cm)	h_{mid}	1.19 cm
Maximum height, upper point (80 cm)	h_{up}	3.35 cm

7.2 Rheological characterisation

As discussed in Section 6.5, the rheological characterisation of a natural mud is a complex task, as it depends on various material factors and flow conditions. In the case of this experimental campaign, no rheometric measurements were carried out on the material, and the only available information is the granulometric distribution and the bulk density of each test.

This is not a defect of the present benchmark but rather a reflection of the usual situation of any geotechnical application. Indeed, the rheological parameters of natural muds are rarely determined from rheometric measurements and are more often estimated from empirical relationships or back-calculated from flow observations. Moreover, because of the simplifications inherent to any modelling approach, the rheological parameters giving the best fit to the observations are not expected to be the same as those measured in a rheometer, even if the latter were available.

The strategy adopted here is based on the article by Bonomelli *et al.* (2025). It does not predict the parameters from *a priori* information, but rather fits them from the experimental data.

7.2.1 Fitting procedure

Analytical reference

The calibration procedure relies on two independent relations.

The first one is the depth-averaged Herschel-Bulkley law (see Equation 4.8):

$$\bar{u}_\infty \;=\; \frac{h}{n+1}\left(\frac{\tau_y}{K}\right)^{\frac{1}{n}} \frac{(1-\xi)^{\frac{(n+1)}{n}}}{\xi^{\frac{1}{n}}} \left(1 \;-\; \frac{n}{2n+1} \;+\; \frac{n\,\xi}{2n+1}\right), \qquad \xi \;=\; \frac{\tau_y}{\tau_b} \tag{7.1}$$

where $\tau_b = \rho g h \sin\theta$ (6.2) is the basal shear stress for a uniform flow of thickness h on a slope of angle θ, and $\xi \in [0,1]$ measures the ratio between yield stress and driving stress. Equation 7.1 reduces to the Bingham form (4.7) for $n = 1$. It is the expression for the asymptotic velocity $\bar{u}_\infty$ of a uniform, fully established flow with no basal slip.

The second relation is directly derived from Equation 6.1:

$$h_{\mathrm{dep}} \;=\; \frac{\tau_y}{\rho\, g\, \sin\theta} \tag{7.2}$$

where h_{dep} is the thickness of the residual deposit left on the inclined channel after the flow has stopped. Equation 7.2 therefore provides a direct estimate of τ_y from a purely geometric measurement.

A third quantity completes the analytical framework, the characteristic time T required for the flow to reach the asymptotic regime described by (7.1). An estimate of the characteristic time

can be obtained from the Bingham limit of the depth-averaged momentum balance (Bonomelli *et al.* 2025):

$$T \;=\; \frac{\rho\, h^2 \cos\theta}{3\,\mu}. \tag{7.3}$$

The characteristic time does not enter the calibration itself but provides an *a posteriori* check on its validity. A calibration based on (7.1) can only be trusted if the residence time of the flow in the channel is significantly larger than T, so that the asymptotic regime is actually reached. This check is made explicitly in Section 7.2.1.

Procedure

The fitting procedure consists in using the static criterion (7.2) to determine τ_y from the deposit thickness, and then in inverting the depth-averaged velocity relation (7.1) to obtain K for a given value of n.

- **Yield stress**

  The yield stress is directly obtained from a representative deposit thickness h_{dep} using Equation (7.2):

  $$\tau_y \;=\; \rho\, g\, h_{\mathrm{dep}}\, \sin\theta.$$

  This estimate is independent of K and n and only requires the slope angle and the bulk density of the deposit.

- **Flow index**

  The flow index n is not directly constrained by any of the measurements, and is therefore treated as a free parameter. It is fixed *a priori* to a set of values spanning the range from strongly shear-thinning to mildly shear-thickening behaviour, and a sensitivity analysis is carried out to assess the influence of n on the results.

- **Consistency**

  With τ_y and n fixed, K is recovered analytically from the velocity inversion of Equation 7.1. Inverting Equation 7.1 for K yields

  $$K \;=\; \tau_y \left[\frac{h}{(n+1)\,\bar{u}_\infty}\, \frac{(1-\xi)^{(n+1)/n}}{\xi^{1/n}} \left(1 - \frac{n}{2n+1} + \frac{n\,\xi}{2n+1} \right) \right]^n, \qquad \xi \;=\; \frac{\tau_y}{\rho\, g\, h\, \sin\theta}$$

  where ξ uses the yield stress obtained from the yield stress step above.

Application to experiment T08

The procedure described above requires three input quantities: an estimate of the asymptotic uniform-flow velocity $\bar{u}_\infty$, the corresponding flow thickness h, and the residual deposit thickness h_{dep} on the inclined channel. These three quantities are not directly measured in the experiment. Therefore, they are estimated from the available measurements as follows:

- **Flow velocity**

  At the beginning of the channel, the flow is still accelerating from the gate release, and the mean front velocity V_m recorded by the optical fibre averages over this inertial phase. The best available estimate for the asymptotic velocity is the peak velocity V_f reached just downstream of the channel outlet, before lateral spreading starts to dissipate the flow on the horizontal plane. We therefore retain

  $$\bar{u}_\infty \;\approx\; V_f \;=\; 0.38\,\mathrm{m/s}.$$

- **Flow thickness**

  The thickness associated with $\bar{u}_\infty$ is taken at the middle control point of the channel (40 cm from the outlet), where the flow has had enough time to develop a quasi-steady profile while still being confined to the inclined-channel geometry underlying Equation 7.1. The Carbopol benchmark of Chapter 5 showed that the free-surface profile reaches a clear plateau in the established region, which supports the use of the maximum height recorded at this location:

  $$h \;\approx\; h_{\mathrm{mid}} \;=\; 1.2\,\mathrm{cm}.$$

- **Deposit thickness**

  A frame-by-frame analysis of the in-channel camera footage gives the residual deposit thickness once motion has ceased:

  $$h_{\mathrm{dep}} \;\approx\; 0.78\,\mathrm{cm}.$$

The three values are of the same order of magnitude as those reported by Ancey *et al.* (2012) for a comparable inclined dam-break configuration. Inserting h_{dep} in the static criterion gives $\tau_y = 92.1$ Pa. The consistency K is then obtained from the velocity inversion for several values of the flow index n, sweeping the range from strongly shear-thinning to mildly shear-thickening behaviour.

A final adjustment is applied to the calibrated consistency, which is multiplied by a factor between 2 and 5 before being used in the model. The channel is in fact too short for the flow to reach its asymptotic regime. The velocity V_f measured at the outlet substantially exceeds the true $\bar{u}_\infty$, and the inversion therefore underestimates K. The multiplicative correction is the simplest way to compensate for this systematic bias without altering the analytical inversion, and its magnitude is tuned to match the flow duration and runout distance reported in Table 7.1.

The complete set of parameters retained for the numerical experiments is summarised in Table 7.2.

Table 7.2. *Rheological parameters fitted for experiment T08.*

Parameter	Symbol	Values across n				
Flow behaviour index (–)	n	0.3	0.7	1.0	1.2	1.4
Consistency index (Pa·s^n)	K	16.078	2.92	0.72	0.365	0.165
Yield stress (Pa)	τ_y	92.1	92.1	92.1	92.1	92.1
Characteristic time (s)	T	–	–	0.37	–	–

The characteristic time of Table 7.2 for the Bingham parameter set can now be compared to the residence time of the flow in the channel, $t_D \approx 0.7$ s. Both timescales are of the same order of magnitude. The flow therefore does not have time to reach an established uniform regime within the channel. This violation of the calibration hypothesis provides the justification for the multiplicative correction subsequently applied to K.

Despite this limitation, the calibrated parameter sets remain physically consistent and within the expected range for dense clayey-to-silty mudflow, and they are of the same order as the fitted parameters obtained by Liesse (2026) for the same experiment.

7.3 Results

The five rheological parameter sets of Table 7.2 are compared with the T08 measurements on the front velocity and the flow heights inside the channel, as well as the two-dimensional geometry of the final deposit on the horizontal plane. The simulations are carried out with the regime B slope-based closure described in Chapter 6.

7.3.1 Channel dynamics

The table of channel metrics (Table 7.3) summarises the comparison between the experiment and the simulations for the mean front velocity V_m, the outlet velocity V_{outlet} and the residence time t_{outlet} of the flow in the channel.

Table 7.3. *Channel metrics for experiment T08: experiment vs. simulations.*

Quantity	Exp.	HB (n=1.4)	HB (n=1.2)	Bingham	HB (n=0.7)	HB (n=0.3)
V_{m} (m/s)	1.467	2.169	2.203	2.298	2.387	2.455
V_{outlet} (m/s)	0.380	1.723	1.855	1.907	1.909	2.085
t_{outlet} (s)	≈ 0.7	0.4	0.37	0.37	0.37	0.33

Figure 7.2 shows the simulated front velocity in the channel and on the deposit zone for the five rheological parameter sets. They all share the same qualitative behaviour, a peak velocity on gate release followed by a continuous deceleration, with no intermediate plateau. No asymptotic regime like in the results of Chapter 5 is visible at any point. This is a direct consequence of the channel being too short for the friction to balance gravity, as already anticipated by the comparison between the residence time $t_D \approx 0.7$ s and the characteristic time of Table 7.2.

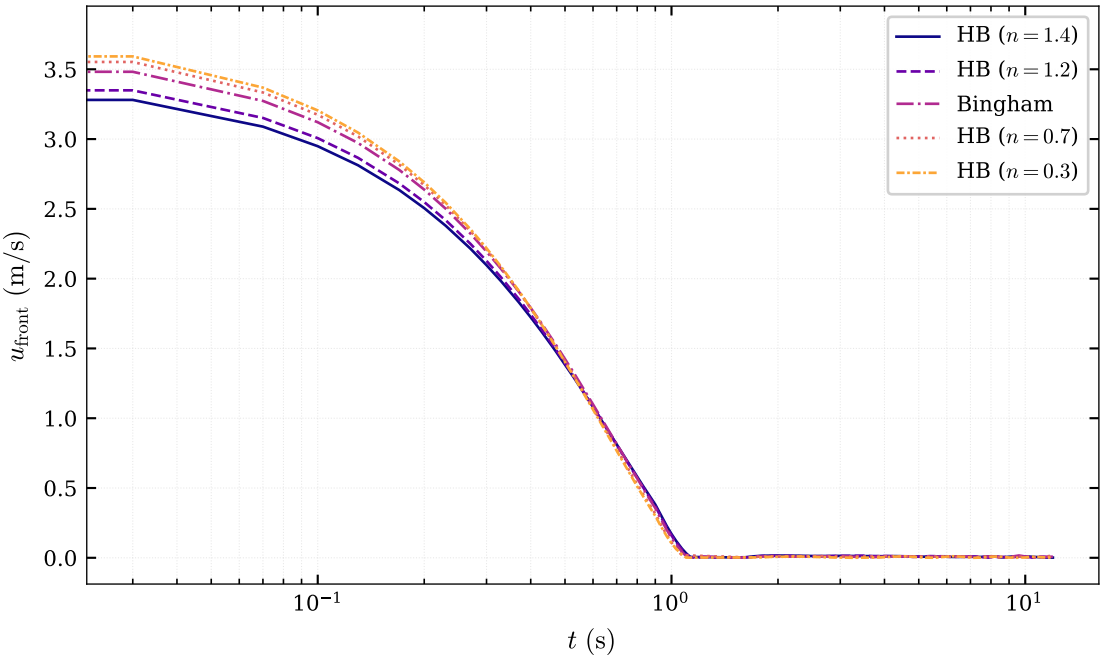


Fig 7.2. *Time evolution of the simulated front velocity in the channel and deposit zone for the five rheological parameter sets.*

The same conclusion is reached from the velocity recorded at the channel outlet (Figure 7.3). The simulated outlet velocities lie in the range 1.7–2.1 m/s, against an experimental peak of $V_f = 0.38$ m/s at the entrance of the deposition plane. Two contributions combine to produce this overshoot. The first is the calibration bias identified in Section 7.2.1: V_f is higher than the true asymptotic velocity, so the inverted consistency K is too low even after the multiplicative correction. The second is intrinsic to the model. The Carbopol benchmark of Chapter 5 already showed that the model tends to overestimate the front velocity during the inertial phase that follows the gate release, and this phase covers the entire residence time of the flow in the channel for this configuration. The two effects act in the same direction and explain why even the best calibration leaves a large gap between the simulated and the measured outlet velocity.

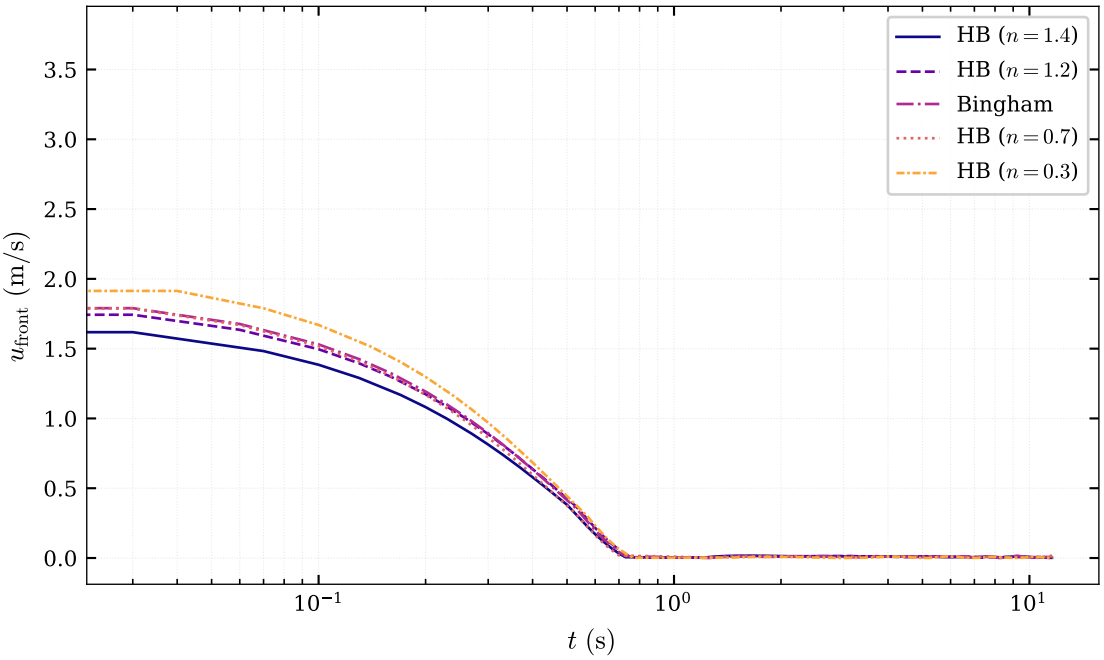


Fig 7.3. *Time evolution of the simulated front velocity, time-shifted so that $t = 0$ corresponds to the passage of the front at the channel outlet.*

Figure 7.4 shows the simulated free-surface profiles in the channel at six successive times. After the initial passage of the wave, the profiles first stabilise around an intermediate plateau of approximately 1.2 cm, clearly visible at $t = 1$ s and $t = 2$ s. This value coincides with the maximum height $h_{\mathrm{mid}} = 1.19$ cm recorded at the middle control point, and validates *a posteriori* the choice made in Section 7.2.1 to use h_{mid} as the estimate for the established flow height in the calibration. As the flow decelerates and stops, the profiles relax towards a second, lower plateau of about 0.8 cm, in close agreement with the experimental residual deposit $h_{\mathrm{dep}} \approx 0.78$ cm. The slight overshoot is consistent with the behaviour already observed on the Carbopol benchmark.

The maximum heights observed at the two control points are largely overestimated by the simulations. These maxima are reached during the transient passage of the front, when the flow is still in its inertial phase, and they are therefore directly affected by the same overestimation of the velocity discussed above.

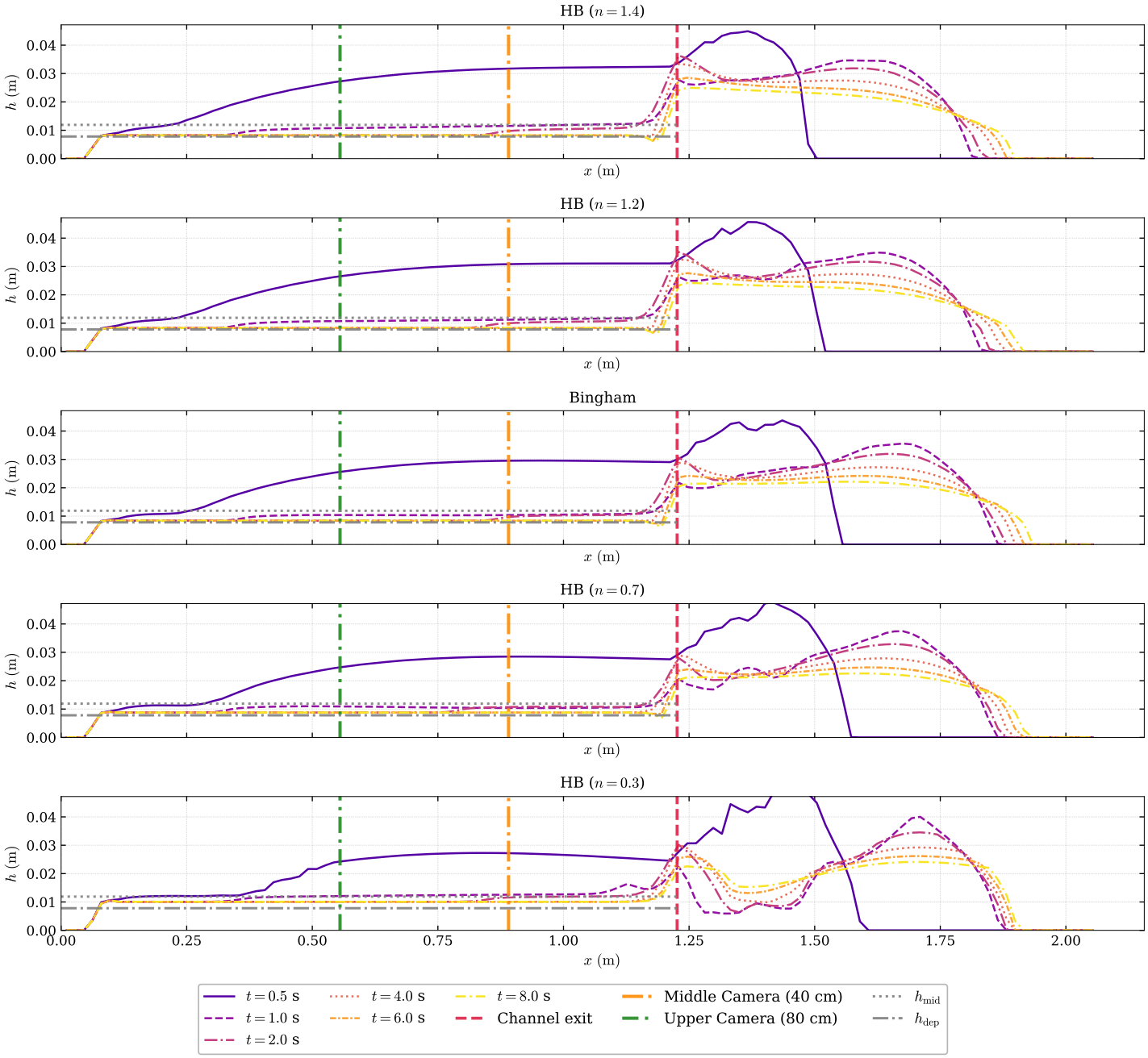


Fig 7.4. *Longitudinal free-surface profiles along the channel axis at six successive times for the five rheological parameter sets of Table 7.2. Dashed lines mark the channel outlet and the two control points at* 40 *cm (middle) and* 80 *cm (upper) from the outlet.*

7.3.2 Deposit geometry

Figure 7.5 compares the laser-scanned deposit with the five simulated final states. The overall shape is reproduced by all parameter sets: the deposit widens transversely and stops at a comparable downstream distance.

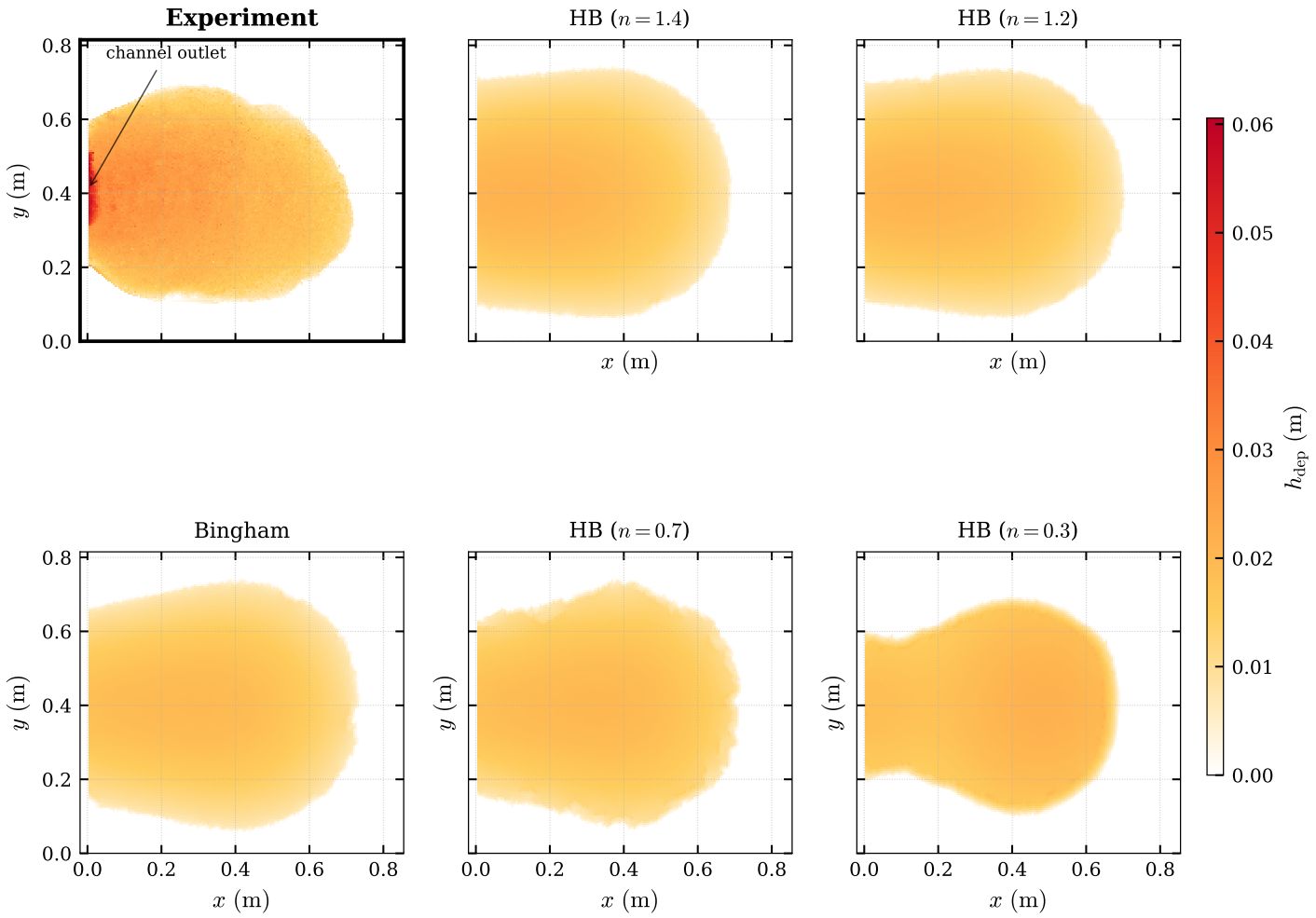


Fig 7.5. *Top view of the final deposit on the horizontal plane. Top left: laser scan of the experimental deposit. Other panels: simulated deposit at $t = 12$ s for each rheological parameter set of Table 7.2.*

The principal qualitative difference lies in the redistribution of material along the streamwise direction. The experimental deposit shows a marked peak of thickness at the channel outlet, where the material accumulates against the horizontal plane. This peak reaches $h_{\mathrm{max}}^{\mathrm{exp}} = 6.06$ cm, whereas the simulated deposits remain essentially flat at $h \approx 2$ cm.

The longitudinal and transverse cuts of Figure 7.6 confirm that the simulations spread the same volume of material more uniformly over the deposition plane, missing the near-channel accumulation. However, the global shape of the depth profiles is correctly reproduced by all parameter sets, with a steep front and a long tail, and the maximum thickness is reached at the same location as in the experiment.

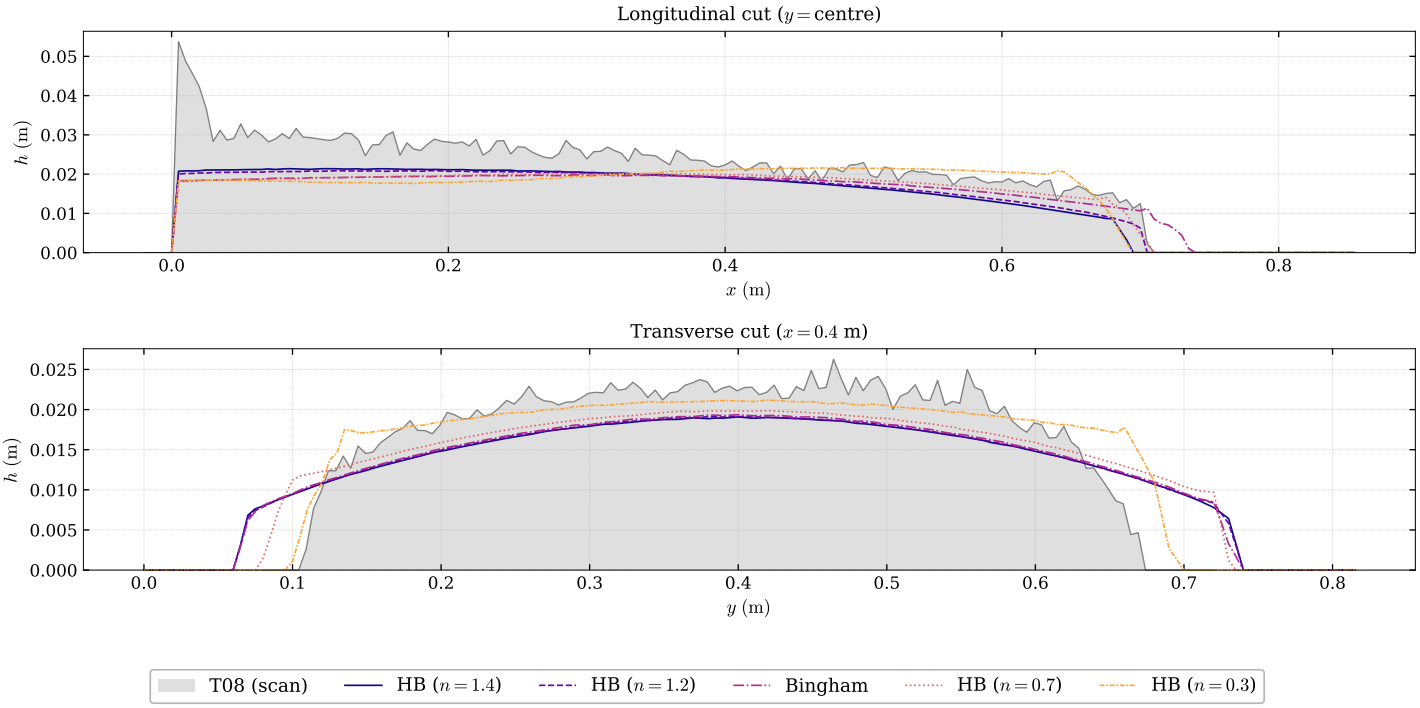


Fig 7.6. *Top: longitudinal cut of the final deposit along $y = 0.4$ m. Bottom: transverse cut at $x = 0.4$ m. The simulations spread the material more uniformly than the experiment, which exhibits a pronounced peak near the channel outlet.*

Figure 7.7 shows the spatial distribution of the local difference $h_{\mathrm{sim}} - h_{\mathrm{exp}}$ between the simulated and experimental deposit thicknesses, along with two scalar metrics: the bias[1], which measures the mean signed deviation between simulation and experiment, and the root-mean-square error (RMSE)[2], which measures the typical amplitude of the local deviations.

All five parameter sets share a negative bias between -2.4 and -4.0 mm. The simulated deposit is, on average, thinner than the experimental one. The RMSE stays between 6.6 and 7.0 mm for the four less shear-thinning parameter sets and rises to 8.4 mm for $n = 0.3$. The fact that the RMSE is roughly three times larger than the absolute value of the bias indicates that the discrepancy is not a uniform underestimation of the thickness, but a spatial redistribution of the material. The central region is too thin (negative contributions to the difference) while the lateral edges are too thick (positive contributions). The two effects partially cancel in the bias but add up in the RMSE.

[1] The bias is the arithmetic mean of the local differences $h_{\mathrm{sim}} - h_{\mathrm{exp}}$ over the N points of the deposit area, $\mathrm{bias} = \frac{1}{N}\sum_{i=1}^{N}\left(h_{\mathrm{sim},i} - h_{\mathrm{exp},i}\right)$. A negative bias indicates that the simulation is on average thinner than the experiment.

[2] RMSE is the root-mean-square of the same local differences, $\mathrm{RMSE} = \left(\frac{1}{N}\sum_{i=1}^{N}\left(h_{\mathrm{sim},i} - h_{\mathrm{exp},i}\right)^2\right)^{1/2}$, and quantifies their typical magnitude regardless of sign. It is always larger than or equal to the absolute value of the bias.

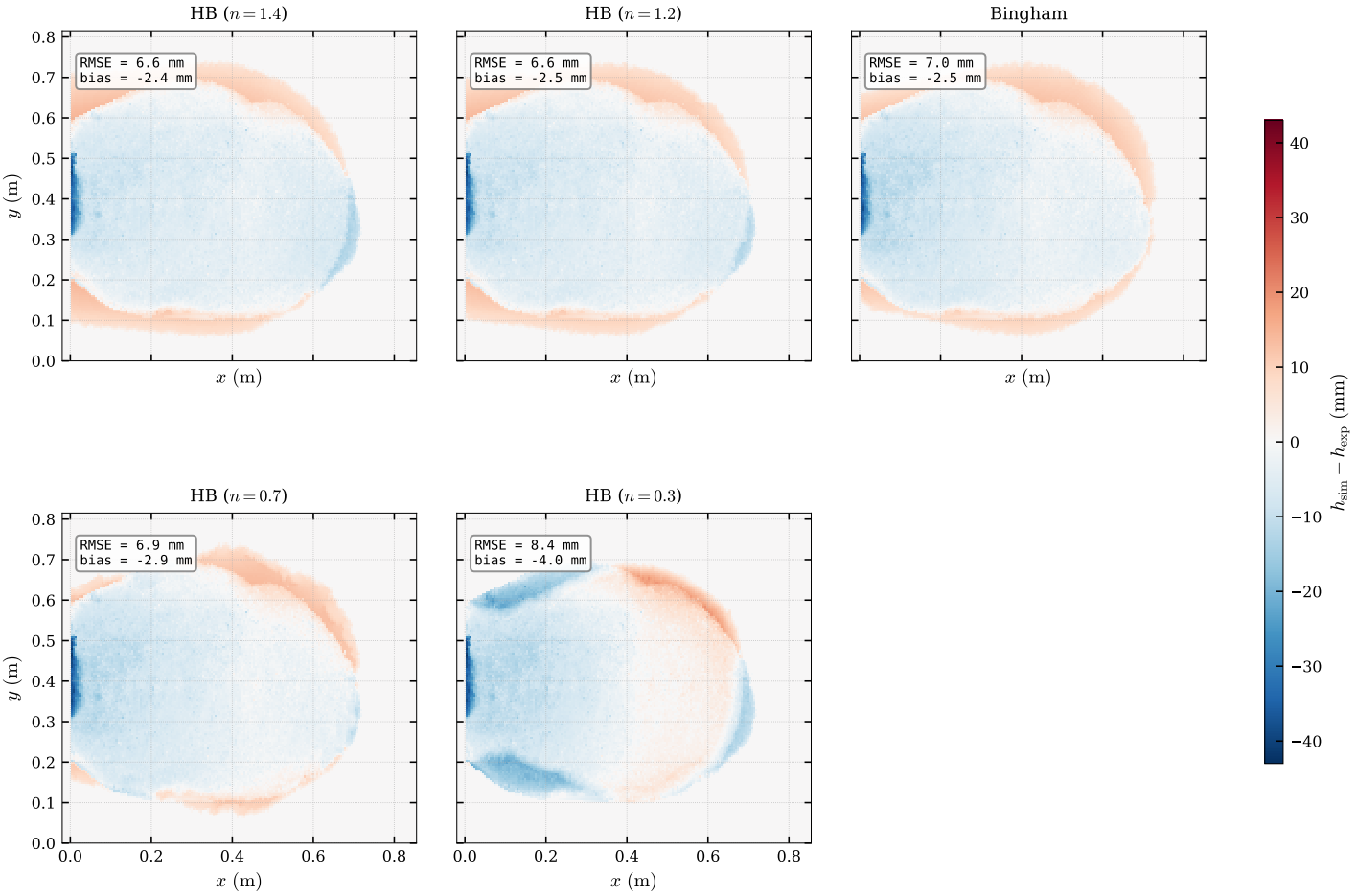


Fig 7.7. *Maps of the difference $h_{\mathrm{sim}} - h_{\mathrm{exp}}$ at $t = 12$ s for the five rheological parameter sets. RMSE and bias are reported in each panel.*

Table 7.4 summarises the comparison between the experiment and the simulations for a set of scalar metrics extracted from the deposit geometry.

Table 7.4. *Scalar metrics for experiment T08: experiment vs. simulations.*

Quantity	Exp.	HB (n=1.4)	HB (n=1.2)	Bingham	HB (n=0.7)	HB (n=0.3)
$h_{\max}$ (cm)	6.06	2.15	2.09	1.99	2.02	2.18
Δx (cm)	71.5	69.0	70.0	73.0	71.0	68.5
Centroid x (cm)	30.1	29.8	30.8	33.5	33.7	35.7
Deposit RMSE (mm)	–	6.6	6.6	7.0	6.9	8.4
Deposit bias (mm)	–	–2.4	–2.5	–2.5	–2.9	–4.0

7.4 Discussion and conclusions

Table 7.4 illustrates that none of the five rheological parameter sets is able to reproduce all the experimental metrics simultaneously. The downstream extent Δx and streamwise centroid position are correctly captured by all five parameter sets and the best of them is the one using the Herschel-Bulkley law with $n = 1.4$ or $n = 1.2$. The maximum height $h_{\max}$, on the other hand, is underestimated by a factor of three by all parameter sets. The accumulation of material at the channel outlet is missed by every parameter set.

The fact that the best results are obtained for $n > 1$ is surprising, as natural muds are generally expected to be shear-thinning. This may be a consequence of the calibration strategy, which relies on the inversion of an analytical solution that is only partially valid for this configuration, as discussed in Section 7.2.1. This highlights the limitations of the present approach, which is based on a single experiment and a single calibration strategy. The procedure inspired by Bonomelli *et al.* (2025) is a first step towards a more systematic calibration of the model, but it needs to be improved and adapted to the current solver on a larger set of experiments to be able to give more robust conclusions on the rheological parameters of the material and the best closure to use for natural muds.

Despite these limitations, the present benchmark provides a valuable test of the model's ability to reproduce the deposit geometry of a natural mudflow. The fact that all parameter sets capture the overall shape of the deposit and its downstream extent is encouraging, and suggests that the model is a relevant first step towards a tool for hazard assessment purposes, even if it may not capture all the details of the flow dynamics.

CHAPTER 8

Conclusion and perspectives

8.1 Conclusion

The principal objective of this master's thesis was to improve, within the existing Watlab framework, a numerical tool dedicated to mudflow simulation, building on the work of Liesse (2026). As explained in previous chapters, this objective was met for idealised viscoplastic flows and partially met for natural mudflows. Remaining gaps are documented in Section 8.2 hereunder providing guidance for future work.

8.1.1 Summary of contributions

The main outcome of this work is a version of Watlab enabling the simulation of viscoplastic free-surface flows. The outcome can be subdivided into three main contributions.

The first concerns the solver itself. The order-of-magnitude analysis of Appendix A established that the friction source term and the inertial flux divergence are of comparable magnitude in mudflows, and that the friction may even dominate during the run-out phase. However, the operator-splitting strategy on which Watlab is built, originally designed for inertia-dominated water flows, is not well suited for the regime of interest in the case of mudflows. The sequencing "flux update first, source as correction" was found to produce a non-physical *artificial mass diffusion*. The temporary state variable, the vector-valued stopping criterion and the semi-implicit treatment of the friction proposed in Chapter 3 resolve this issue within the current framework.

The second contribution is the implementation, comparison, and benchmarking of several rheological closures. The Bingham, Herschel-Bulkley, Casson and quadratic models reviewed in Chapter 4 were implemented through a regularisation strategy inspired by the work of Papanastasiou (1987). The basal shear stress, initially recovered by numerical inversion of the depth-averaged relation $\bar{u}\left(\tau_b\right)$, was subsequently re-implemented in Chapter 6 through the explicit slope-based formulation of Muchiri *et al.* (2025) in both its Regime A (gravity-only driving slope) and Regime B (with the leading-order free-surface gradient correction) forms. The carbopol dam-break experiment of Ancey *et al.* (2012) was used as the reference for benchmarking the different rheological closures and different models from the literature. The slope-based formulation was found to reproduce the most accurately the experimental data, and to be

substantially less computationally expensive than the velocity-based closure.

The third contribution is the validation of the developed model using mudflow experiments. The real-material experiments T08 of the Polimi campaign, addressed in Chapter 7, showed that the model captures the overall shape and downstream extent of the natural mud. However, the model was found to overlook some observed behaviours, such as the accumulation of material at the channel outlet.

Despite these discrepancies, the different results obtained throughout the master's thesis allow concluding that the current model captures the main quantities of interest for geohazard assessment, such as the front position, velocity, and run-out distance with a good degree of accuracy. These results are convincing enough to be considered a significant step forward in the development of a predictive tool for mudflow simulation. Moreover, it suggests that the approach considered is promising and worth pursuing.

8.1.2 Limitations

Even though the use of the model led to convincing results, some limitations should be acknowledged. Three main limitations are identified.

The first is the inertial-phase overshoot of the front position and velocity, partially explained by the absence of the additive momentum correction of Muchiri *et al.* (2025) and traced back in Chapter 5 to the steady fully-developed assumption underlying the velocity-based closure.

The second limitation appeared during the calibration of the model with the Polimi experiment, whereby the best fit was obtained for unexpected shear-thickening exponents $n > 1$. This result is not consistent with the shear-thinning behaviour generally expected for natural muds and is most likely due to the calibration procedure, and the absence of an established flow during the experiment constraining the rheological parameters.

The third limitation is the discrepancy between the simulated and experimental deposit thickness, which is most likely due to the vector-value stopping criterion, a simplified representation of the complex process of flow cessation.

8.2 Perspectives

The work presented in this thesis opens many perspectives for future model improvements. They are presented here in increasing order of complexity considering the current state of the model. The following list aims not to be exhaustive but to provide a roadmap for future work.

8.2.1 Completing the slope-based formulation of Muchiri *et al.* (2025)

The simplest extension recommended is the implementation of the additive momentum correction of Muchiri *et al.* (2025), which the implementation in Chapter 6 does not include. The correction expresses the depth-integrated convective term as:

$$\int_b^H u^2 \, \mathrm{d}z \;\simeq\; \frac{q_x^2}{h} \;+\; C_m \Lambda_x^{2m} \, h^{2m+3}$$

with a similar contribution along y and a cross-term in the two-dimensional case, where $\Lambda = (\rho g / K)\, \vec{S_\theta}$ and $m = 1/n$.

Physically, it encodes the fact that the depth-averaged momentum flux $\bar{u}^2 h$ underestimates the true kinetic-energy flux whenever the vertical velocity profile is non-uniform. The inertial overshoot observed in the early phase of the flow is consistent with the absence of this term and would most likely be reduced by its inclusion. The implementation is conceptually straightforward but requires the additive term to enter the conservative momentum flux at every cell interface, with the corresponding revision of the LHLLC flux reconstruction and of the CFL condition. As both the slope-based closure already in place and the additive correction derive from the same Herschel–Bulkley vertical profile and use the same driving slope, $\vec{S_\theta}$, this extension is the most natural continuation of the developments presented in Chapter 6.

8.2.2 A systematic, model-specific calibration of the rheological parameters

The benchmark of Chapter 7 identified the rheological calibration as a key challenge for the application of the model to natural mudflows. The procedure inspired by Bonomelli *et al.* (2025) adopted in this work is promising but the inconsistent shear-thickening exponent obtained for T08 shows that it cannot yet be relied upon as a predictive calibration.

A more robust strategy would be either to adapt the procedure of Bonomelli *et al.* (2025) to the specificities of the model on several experiments with a clear established flow phase, or to develop a new procedure. The latter could be based on the same principle of minimising the distance between the simulated and experimental flow fields, but with a more systematic exploration of the parameter space and a more robust optimisation algorithm.

8.2.3 From a single-phase to a multilayer vertical structure

A more substantial extension, addressing the physics rather than the numerics, would be to move from the single-phase depth-averaged description to a multilayer structure. The single-phase model adopted in this work, while computationally efficient, collapses the entire flow depth onto a single averaged velocity and a single set of rheological properties. It therefore cannot represent the vertical heterogeneity that characterises natural mudflows i.e. the coexistence of a sheared basal region and an upper plug zone, the vertical segregation of the material, *etc*.

These mechanisms are widely held responsible for several of the behaviours the present model fails to reproduce, in particular the accumulation of material observed at the channel outlet in Chapter 7.

A multilayer shallow-water formulation, such as the one proposed by Fernández-Nieto *et al.* (2023), discretises the flow depth into a few superposed layers, each carrying its own thickness and velocity and coupled to its neighbours through interfacial exchanges of mass and momentum. It thus restores part of the vertical structure lost in the depth-averaging, while remaining far less expensive than a fully three-dimensional simulation. It is worth noting that the developments introduced in this work i.e. the semi-implicit treatment of the friction and the slope-based closure, are formulated cell by cell and could be applied layer by layer. Therefore, they are structurally compatible with such an extension, which could be built incrementally on top of the existing solver.

8.2.4 A solver with an intrinsic treatment of the friction source term

The largest limitation of the present implementation is structural and lies in the operator-splitting strategy on which Watlab is built. As explained in Chapter 3, this strategy treats the gravity–friction balance as a correction applied after a flux update that is itself blind to the source term, a sequencing that is well adapted to inertia-dominated water flows but loses its physical justification for viscoplastic flows in which the friction and the flux divergence are of comparable magnitude. The temporary state variable, the stopping criterion and the semi-implicit linearisation introduced in this work mitigate the visible symptoms, but they remain workarounds within a framework that was not designed for friction-dominated regimes.

The natural long-term improvement would be the development of a solver in which the friction source term is incorporated directly in the construction of the numerical flux. Consequently, the gravity–friction balance is enforced at the cell interfaces rather than corrected subsequently.

APPENDIX A

Order-of-magnitude estimate of the inertial flux term

A.1 Water flow case

A.1.1 Characteristic scales

Let us introduce the following characteristic scales:

- characteristic depth: $h \sim H$,
- characteristic horizontal velocity: $u, v \sim U$,
- characteristic horizontal length scale: $x, y \sim L$.

From the definitions of the specific discharges, we have $q_x = hu \sim HU$ and $q_y = hv \sim HU$. The spatial derivatives also scale as $\partial/\partial x,\ \partial/\partial y \sim 1/L$.

A.1.2 Order of magnitude of the different components

Firstly we have (the development is done here for the x-momentum equation, but the same reasoning applies to the y-momentum equation):

$$\frac{\partial F}{\partial x} = \frac{\partial}{\partial x}\left(\frac{q_x^2}{h} + \frac{1}{2}gh^2\right) \sim \frac{1}{L}\left(HU^2 + gH^2\right) = \frac{gH^2}{L}\left(Fr^2 + 1\right)$$

and

$$\frac{\partial G}{\partial y} = \frac{\partial}{\partial y}\left(\frac{q_x q_y}{h}\right) \sim \frac{HU^2}{L} = \frac{gH^2}{L}\,Fr^2$$

where $Fr = U/\sqrt{gH}$ is the Froude number. Therefore, the flux divergence scales as:

$$\left|\frac{\partial F}{\partial x} + \frac{\partial G}{\partial y}\right| \sim \frac{gH^2}{L}\left(1 + 2\,Fr^2\right).$$

On the other hand, the friction source term scales as

$$ghS_f \sim gH\frac{n^2\,U^2}{H^{4/3}} = gn^2\,U^2\,H^{-1/3}$$

where we have used the expression of the friction slope $S_f = n^2\,U^2/H^{4/3}$ for Manning's friction.

A.1.3 Comparison of the flux divergence and the friction source term

The ratio between the flux divergence and the friction source term therefore scales as

$$\frac{\left|\partial_x F + \partial_y G\right|}{|ghS_f|} \sim \frac{gH^2(1+2\,Fr^2)/L}{gn^2\,U^2\,H^{-1/3}} = \frac{H^{7/3}(1+2Fr^2)}{Ln^2\,U^2} = \frac{H^{4/3}}{Lgn^2}\cdot\frac{1+2\,Fr^2}{Fr^2}.$$

A.1.4 Numerical estimation for typical water flows

To assess the dominance of inertial terms over friction in the context of water flow simulations, we consider characteristic values for typical hydrological applications:

- characteristic depth: $H \sim 1$ m (representative of rivers and floodplains),
- characteristic horizontal length scale: $L \sim 100$ m,
- Manning coefficient: $n \sim 0.03$ (typical for natural channels),
- gravitational acceleration: $g = 9.81$ m/s²,
- Froude number range: $Fr \sim 0.1$ (subcritical flows dominating most hydrological contexts).

For a typical lowland river or floodplain configuration ($Fr = 0.1$, $L = 100$ m):

$$\text{Ratio} \sim \frac{1^{4/3}}{100\times 9.81\times(0.03)^2}\times\frac{1+2(0.1)^2}{(0.1)^2} \approx \frac{1}{0.8829}\times\frac{1.02}{0.01} \approx 115.$$

This indicates that the inertial flux divergence is approximately two orders of magnitude larger than the friction source term, confirming that inertial effects are dominant in such flow conditions.

A.2 Mudflow case

A.2.1 Characteristic scales and friction term

For mudflows, the main difference is that the friction term scales as follows:

$$ghS_f \sim gH\frac{\tau_b}{\rho gH} = \frac{\tau_y}{\rho}$$

where τ_b is the basal shear stress, τ_y is the yield stress of the mud which is the minimum shear stress required to initiate flow, and ρ is the density of the mud.

A.2.2 Order of magnitude of the flux divergence

The flux divergence for mudflows remains similar to the water flow case:

$$\left|\frac{\partial F}{\partial x}+\frac{\partial G}{\partial y}\right| \sim \frac{gH^2}{L}\left(1+2\,Fr^2\right).$$

A.2.3 Comparison of the flux divergence and the friction source term

The ratio between the flux divergence and the friction source term for mudflows therefore scales as:

$$\frac{\left|\partial_x F+\partial_y G\right|}{|ghS_f|} \sim \frac{gH^2(1+2\,Fr^2)/L}{\tau_y/\rho} = \frac{\rho g H^2(1+2\,Fr^2)}{L\tau_y}.$$

A.2.4 Numerical estimation for typical mudflows

To assess the relative importance of inertial and friction terms in mudflows, we consider the following characteristic values:

- characteristic depth: $H \sim 0.5$ m,
- characteristic horizontal length scale: $L \sim 50$ m,
- mud density: $\rho \sim 1500$ kg/m^3,
- yield stress: $\tau_y \sim 100$ Pa,
- Froude number range: $Fr \sim 0.3$ (subcritical to transcritical flows).

For a typical mudflow configuration:

$$\text{Ratio} = \frac{1500 \times 9.81 \times (0.5)^2(1+2(0.3)^2)}{50 \times 100} = \frac{1500 \times 9.81 \times 0.25 \times 1.18}{5000} \approx 0.87.$$

This indicates that, for mudflows, the friction source term is of the same order of magnitude as the inertial flux divergence, confirming that friction effects are significant in such flow conditions. Moreover, the estimate is conservative, as the basal shear stress was approximated by the yield stress ($\tau_b \approx \tau_y$), which represents a lower bound of the actual friction. In real flowing conditions, $\tau_b > \tau_y$, implying that frictional effects are likely to dominate over inertial fluxes.

APPENDIX B

Casson model derivation

The Casson's model is defined as:

$$\dot{\gamma} = \frac{(\sqrt{\tau} - \sqrt{\tau_y})^2}{\mu}$$

The velocity profile $u(z)$ is obtained by integrating the shear-rate over depth, using the linear shear-stress profile given by equation 4.6:

$$\begin{aligned} u(z) &= \int_0^z \dot{\gamma}(z')\, dz' \\ &= \int_0^z \frac{\left(\sqrt{\tau_b\left(1-\frac{z'}{h}\right)} - \sqrt{\tau_y}\right)^2}{\mu}\, dz' \\ &= \frac{1}{\mu}\int_0^z \left[\tau_b\left(1-\frac{z'}{h}\right) + \tau_y - 2\sqrt{\tau_b\tau_y\left(1-\frac{z'}{h}\right)}\right] dz' \end{aligned}$$

Integrating for the two separate intervals $[0, h_s]$ and $[h_s, h]$, we have :

- for $z \leq h_s$, separating the integral in three parts :

$$\begin{aligned} I_1 &= \int_0^z \tau_b\left(1-\frac{z'}{h}\right) dz' = \tau_b\left[z' - \frac{(z')^2}{2h}\right]_0^z = \tau_b\left(z - \frac{z^2}{2h}\right) \\ I_2 &= \int_0^z \tau_y\, dz' = \tau_y z \\ I_3 &= \int_0^z \sqrt{\tau_b\tau_y\left(1-\frac{z'}{h}\right)}\, dz' = \frac{2h\sqrt{\tau_b\tau_y}}{3}\left[1-\left(1-\frac{z}{h}\right)^{3/2}\right] \end{aligned}$$

  which gives the velocity profile for $z \leq h_s$:

$$u(z) = \frac{1}{\mu}\left[\tau_b\left(z - \frac{z^2}{2h}\right) + \tau_y z - \frac{4h\sqrt{\tau_b\tau_y}}{3}\left(1-\left(1-\frac{z}{h}\right)^{3/2}\right)\right] \quad \forall z \in [0, h_s]$$

- for $h_s < z < h$, in this part, the speed is constant along depth and equal to $u(h_s)$. With $\xi = \frac{\tau_y}{\tau_b}$ and using :

$$\tau_b\left(1-\frac{h_s}{h}\right) = \tau_y \quad \Rightarrow \quad 1 - \frac{h_s}{h} = \frac{\tau_y}{\tau_b} \quad \Rightarrow \quad h_s = h\,(1-\xi)$$

The expression of $u(h_s)$ is directly obtained from the previous result with $z = h_s$ and using the relation above:

$$\begin{aligned} u(h_s) &= \frac{1}{\mu}\left[\tau_b\left(h_s - \frac{h_s^2}{2h}\right) + \tau_y h_s - \frac{4h\sqrt{\tau_b\tau_y}}{3}\left(1 - \left(1 - \frac{h_s}{h}\right)^{3/2}\right)\right] \\ &= \frac{1}{\mu}\left[\tau_b\left(h(1-\xi) - \frac{h^2(1-\xi)^2}{2h}\right) + \tau_b\xi\cdot h(1-\xi) - \frac{4h\tau_b\sqrt{\xi}}{3}\left(1-\xi^{3/2}\right)\right] \\ &= \frac{h\tau_b}{\mu}\left[(1-\xi) - \frac{(1-\xi)^2}{2} + \xi(1-\xi) - \frac{4\sqrt{\xi}}{3}(1-\xi^{3/2})\right] \end{aligned}$$

and by simplifying the expression, we obtain the velocity profile:

$$u(h_s) = \frac{1}{\mu}\left[\frac{\tau_b h}{2} + \tau_y h - \frac{4h\sqrt{\tau_b\tau_y}}{3} - \frac{h\tau_y^2}{6\tau_b}\right] \quad \forall z \in [h_s, h]$$

Then, the depth-averaged velocity $\bar{u}$ is obtained by integrating the velocity profile over depth:

$$\begin{aligned} \bar{u} &= \frac{1}{h}\left(\int_0^{h_s} u(z)\,dz + \int_{h_s}^{h} u(h_s)\,dz\right) = I_1 + I_2 \\ I_1 &= \frac{1}{h}\int_0^{h_s}\frac{1}{\mu}\left[\tau_b\left(z - \frac{z^2}{2h}\right) + \tau_y z - \frac{4h\sqrt{\tau_b\tau_y}}{3}\left(1 - \left(1 - \frac{z}{h}\right)^{3/2}\right)\right]dz \\ &= \frac{1}{\mu h}\left[\tau_b\int_0^{h_s}\left(z - \frac{z^2}{2h}\right)dz + \tau_y\int_0^{h_s} z\,dz - \frac{4h\sqrt{\tau_b\tau_y}}{3}\int_0^{h_s}\left(1 - \left(1 - \frac{z}{h}\right)^{3/2}\right)dz\right] \\ &= \frac{1}{\mu h}\left[\frac{\tau_b h_s^2}{2} - \frac{\tau_b h_s^3}{6h} + \frac{\tau_y h_s^2}{2} - \frac{4h\sqrt{\tau_b\tau_y}}{3}\left(h_s - \frac{2h}{5}\left(1 - \left(1 - \frac{h_s}{h}\right)^{5/2}\right)\right)\right] \\ I_2 &= \frac{1}{h}\int_{h_s}^{h} u(h_s)\,dz = \frac{h - h_s}{h}\cdot u(h_s) \\ &= \frac{\tau_y}{\tau_b}\cdot u(h_s) \quad \text{(because } h - h_s = h\xi\text{)} \\ &= \frac{\xi}{\mu}\left[\frac{\tau_b h}{2} + \tau_y h - \frac{4h\sqrt{\tau_b\tau_y}}{3} - \frac{h\tau_y^2}{6\tau_b}\right] \end{aligned}$$

Finally, the depth-averaged velocity is given by:

$$\begin{aligned} \bar{u} = \frac{1}{\mu h}\Bigg[&\frac{\tau_b h^2(1-\xi)^2}{2} - \frac{\tau_b h^3(1-\xi)^3}{6h} + \frac{\tau_b\xi h^2(1-\xi)^2}{2} \\ &- \frac{4h\sqrt{\tau_b\tau_b\xi}}{3}\left(h(1-\xi) - \frac{2h}{5}\left(1-\xi^{5/2}\right)\right)\Bigg] \\ &+ \frac{\xi}{\mu}\left[\frac{\tau_b h}{2} + \tau_b\xi h - \frac{4h\sqrt{\tau_b^2\xi}}{3} - \frac{h\tau_b\xi^2}{6}\right] \end{aligned}$$

which simplifies to:

$$\bar{u} = \frac{\tau_b h}{\mu}\left[\frac{1}{3} + \frac{\xi}{2} - \frac{4\sqrt{\xi}}{5} - \frac{\xi^3}{30}\right]$$

A trivial verification shows that when $\tau_y = 0$ (i.e. $\xi = 0$), we recover the Newtonian case and when $\tau_y \to \tau_b$ (i.e. $\xi \to 1$), we have $\bar{u} \to 0$ as expected.

APPENDIX C

Use of Generative AI Tools

In the interest of transparency, this appendix describes how generative artificial intelligence (AI) tools were used during the preparation of this work. These tools served strictly as a support, and never as a source of scientific content. In accordance with the institutional guidelines, every element produced with the help of such tools was reviewed, verified, and validated before being incorporated.

Coding assistance

Generative AI was used as an aid for writing and debugging code in Python and C++. Suggesting syntax, explaining error messages, proposing refactorings, and reviewing portions of code. All algorithmic choices, the implementation of the physical models, and the numerical validation are original work. Any suggested code was read, tested, and validated before being incorporated.

Writing assistance

AI tools were used as a linguistic aid only, namely for spelling and grammar correction and for rephrasing sentences to improve clarity and readability. The starting text was written without AI assistance. The tools did not add any content beyond linguistic refinement. The substance, argumentation, and scientific structure of the text remain original work.

Preliminary understanding of unfamiliar topics

Finally, AI tools were used as a first step to obtain an accessible overview of certain adjacent topics, in order to grasp the basic notions before studying them in depth through the primary scientific literature. The explanations obtained were never used as a reference: they served only as an entry point, and every claim was subsequently verified and supported by primary sources cited in the text. The bibliographic research itself was carried out through the relevant scientific databases and library catalogues.

Bibliography

Ancey, Andreini, and Epely-Chauvin (Nov. 2012). “Viscoplastic dambreak waves: Review of simple computational approaches and comparison with experiments”. In: *Advances in Water Resources* 48, pp. 79–91. ISSN: 03091708.

Bagnold (Aug. 6, 1954). “Experiments on a gravity-free dispersion of large solid spheres in a Newtonian fluid under shear”. In: *Proceedings of the Royal Society of London. Series A. Mathematical and Physical Sciences* 225.1160, pp. 49–63. ISSN: 0080-4630, 2053-9169.

Barnes and Walters (July 1985). “The yield stress myth?” In: *Rheol Acta* 24.4, pp. 323–326. ISSN: 0035-4511, 1435-1528.

Barré de Saint-Venant (1871). “Théorie du mouvement non-permanent des eaux, avec application aux crues des rivières et à l’introduction des marées dans leur lit”. In: *Comptes Rendus des Séances de l’Académie des Sciences de Paris* 73, pp. 147–154, 237–240.

Bonomelli, Pilotti, and Farina (2025). “Use of simple analytical solutions in the calibration of shallow water equation debris flow models”. In: *Earth Surface Dynamics* 13.4, pp. 665–681.

Boutounet, Monnier, and Vila (Jan. 2016). “Multi-regime shallow free surface laminar flow models for quasi-Newtonian fluids”. In: *European Journal of Mechanics - B/Fluids* 55, pp. 182–206. ISSN: 09977546.

Büntgen, Oppenheimer, Farinotti, Nahtz, and Esper (Dec. 8, 2025). “The 2025 Blatten disaster in the Swiss Alps followed exceptional warming and highlights the vulnerability of people and heritage in glaciated landscapes”. In: *Commun Earth Environ* 6.1, p. 994. ISSN: 2662-4435.

Coussot (1997). *Mudflow Rheology and Dynamics*. 1st ed. IAHR Monographs. Rotterdam: CRC Press. 1 p. ISBN: 978-90-5410-693-7 978-1-351-42988-7.

Coussot and Meunier (June 1996). “Recognition, classification and mechanical description of debris flows”. In: *Earth-Science Reviews* 40.3, pp. 209–227. ISSN: 00128252.

Dimas, Pouliasis, Dimitriadis, Papanicolaou, Lazaridou, and Michas (Dec. 2023). “Comparison of mudflow simulation models in an ephemeral mountainous stream in Western Greece using HEC-RAS and FLO-2D”. In: *Euro-Mediterr J Environ Integr* 8.4, pp. 919–933. ISSN: 2365-6433, 2365-7448.

Engineers, US Army Corps of (2023). *HEC-RAS Mud and Debris Flow : Non-Newtonian Technical Reference Manual – Rheological Models*. URL: `https://www.hec.usace.army.mil/confluence/rasdocs/rasmuddebris/non-newtonian-technical-reference-manual/rheological-models` (visited on 06/12/2024).

Fernández-Nieto, Garres-Díaz, and Vigneaux (June 2023). “Multilayer models for hydrostatic Herschel-Bulkley viscoplastic flows”. In: *Computers & Mathematics with Applications* 139, pp. 99–117. ISSN: 08981221.

Gibson, Floyd, Sánchez, and Heath (Mar. 15, 2021). “Comparing single-phase, non-Newtonian approaches with experimental results: Validating flume-scale mud and debris flow in HEC-RAS”. In: *Earth Surf Processes Landf* 46.3, pp. 540–553. ISSN: 0197-9337, 1096-9837.

Hirschberg, Fatichi, Bennett, McArdell, Peleg, Lane, Schlunegger, and Molnar (Jan. 2021). “Climate Change Impacts on Sediment Yield and Debris-Flow Activity in an Alpine Catchment”. In: *JGR Earth Surface* 126.1, e2020JF005739. ISSN: 2169-9003, 2169-9011.

Houwen and Geehan (Oct. 1986). *Rheology of Oil-Base Muds*. Vol. SPE Annual Technical Conference and Exhibition. SPE Annual Technical Conference and Exhibition. SPE-15416-MS.

Huang and García (Nov. 10, 1998). “A Herschel–Bulkley model for mud flow down a slope”. In: *J. Fluid Mech.* 374, pp. 305–333. ISSN: 0022-1120, 1469-7645.

Hunt, Zenit, Campbell, and Brennen (Feb. 10, 2002). “Revisiting the 1954 suspension experiments of R. A. Bagnold”. In: *J. Fluid Mech.* 452, pp. 1–24. ISSN: 0022-1120, 1469-7645.

Imaizumi, Ikeda, Yamamoto, and Ohsaka (Nov. 2, 2021). “Temporal changes in the debris flow threshold under the effects of ground freezing and sediment storage on Mt. Fuji”. In: *Earth Surf. Dynam.* 9.6, pp. 1381–1398. ISSN: 2196-632X.

Iverson (Aug. 1997). “The physics of debris flows”. In: *Reviews of Geophysics* 35.3, pp. 245–296. ISSN: 8755-1209, 1944-9208.

Iverson, Reid, and LaHusen (May 1997). “DEBRIS-FLOW MOBILIZATION FROM LANDSLIDES”. In: *Annu. Rev. Earth Planet. Sci.* 25.1, pp. 85–138. ISSN: 0084-6597, 1545-4495.

Liesse (2026). “Modélisation numérique et expérimentale de coulées de boues”. MA thesis. Université Catholique de Louvain.

Lumbroso, Davison, Body, and Petkovšek (Jan. 7, 2021). “Modelling the Brumadinho tailings dam failure, the subsequent loss of life and how it could have been reduced”. In: *Nat. Hazards Earth Syst. Sci.* 21.1, pp. 21–37. ISSN: 1684-9981.

Major (May 1997). “Depositional Processes in Large-Scale Debris-Flow Experiments”. In: *The Journal of Geology* 105.3, pp. 345–366. ISSN: 0022-1376, 1537-5269.

Muchiri, Monnier, and Sellier (Jan. 2025). “Derivation and numerical resolution of 2D shallow water equations for multi-regime flows of Herschel–Bulkley fluids”. In: *European Journal of Mechanics - B/Fluids* 109, pp. 22–36. ISSN: 09977546.

O’Brien and Julien (Aug. 1988). “Laboratory Analysis of Mudflow Properties”. In: *J. Hydraul. Eng.* 114.8, pp. 877–887. ISSN: 0733-9429, 1943-7900.

O’Brien, Julien, and Fullerton (Feb. 1993). “Two-Dimensional Water Flood and Mudflow Simulation”. In: *J. Hydraul. Eng.* 119.2, pp. 244–261. ISSN: 0733-9429, 1943-7900.

Papanastasiou (1987). “Flows of Materials with Yield”. In: *Journal of Rheology* 385.31.

Pastor, Quecedo, González, Herreros, Merodo, and Mira (Feb. 2004). “Simple Approximation to Bottom Friction for Bingham Fluid Depth Integrated Models”. In: *J. Hydraul. Eng.* 130.2, pp. 149–155. ISSN: 0733-9429, 1943-7900.

Pierson and Costa (1987). “A Rheologic Classification of Subaerial Sediment-Water Flows”. In: *Debris Flows/Avalanches: Process, Recognition, and Mitigation*. Ed. by John E. Costa and Gerald F. Wieczorek. Vol. 7. Reviews in Engineering Geology. Boulder, Colorado: Geological Society of America, pp. 1–12.

Schaer (2018). “Modélisation des écoulements à surface libre de fluides non-newtoniens”. Thèse de doctorat. Strasbourg, France: Université de Strasbourg.

Syrakos, Oxtoby, De Villiers, Varchanis, Dimakopoulos, and Tsamopoulos (Mar. 2023). “A unification of least-squares and Green–Gauss gradients under a common projection-based gradient reconstruction framework”. In: *Mathematics and Computers in Simulation* 205, pp. 108–141. ISSN: 03784754.

Trujillo-Vela, Ramos-Cañón, Escobar-Vargas, and Galindo-Torres (Sept. 2022). “An overview of debris-flow mathematical modelling”. In: *Earth-Science Reviews* 232, p. 104135. ISSN: 00128252.

Whorton, Jones, and Wilson (Nov. 2025). “Mudflow rheology: A review and analysis for Earth and planetary science disciplines”. In: *Earth-Science Reviews* 270, p. 105226. ISSN: 00128252.

Zhang, Chen, Tan, Bao, Han, Yan, and Mehmood (July 2021). “A novel approach to simulating debris flow runout via a three-dimensional CFD code: a case study of Xiaojia Gully”. In: *Bull Eng Geol Environ* 80.7, pp. 5293–5313. ISSN: 1435-9529, 1435-9537.

Zhang, Li, Guo, Yang, Liu, and Yu (May 17, 2021). “Temporal Characteristics of Debris Flow Surges”. In: *Front. Earth Sci.* 9, p. 660655. ISSN: 2296-6463.

UNIVERSITÉ CATHOLIQUE DE LOUVAIN
École polytechnique de Louvain
Rue Archimède, 1 bte L6.11.01, 1348 Louvain-la-Neuve, Belgique | **www.uclouvain.be/epl**